UNIVERSITY OF CALIFORNIA, SAN DIEGO

On the role of atmospheric forcing on upper ocean physics in the Southern Ocean and biological impacts

A Dissertation submitted in partial satisfaction of the
requirements for the degree
Doctor of Philosophy

in

Oceanography

by

Magdalena M. Carranza

Committee in charge:

Professor Sarah T. Gille, Chair
Professor Peter J. S. Franks
Professor Jan P. Kleissl
Professor Robert Pinkel
Professor Alberto R. Piola
Professor Lynne D. Talley

2016

The Dissertation of Magdalena M. Carranza is approved, and it is acceptable in quality and form for publication on microfilm and electronically:

_____

_____

_____

_____

_____

_____

Chair

University of California, San Diego

2016

TABLE OF CONTENTS

Signature Page iii

Table of Contents iv

List of Figures vi

List of Tables ix

Acknowledgements x

Vita xi

Abstract of the Dissertation xii

Chapter 1 Introduction 1

Chapter 2 Wind-driven entrainment enhances summer chlorophyll-a in the Southern Ocean 6
- 2.1 Introduction 7
- 2.2 Data and methods 13
  - 2.2.1 Satellite data 14
  - 2.2.2 Reanalysis data 18
  - 2.2.3 Argo mixed-layer depth 18
  - 2.2.4 Statistical analysis 19
- 2.3 Results 23
  - 2.3.1 Southern Ocean phytoplankton blooms 23
  - 2.3.2 Summer atmospheric forcing and MLD variability . 25
  - 2.3.3 Effect of MLD deepening on Chl-a 29
  - 2.3.4 Effect of Ekman pumping on Chl-a 33
  - 2.3.5 SST and Chl-a 35
  - 2.3.6 Discussion 37
- 2.4 Summary and Conclusions 43
- 2.5 Acknowledgments 46

Chapter 3 Frequent chlorophyll-a fluorescence maxima and unevenness within Southern Ocean hydrographic mixed layers 48
- 3.1 Introduction 49
- 3.2 Data 53
  - 3.2.1 Southern-elephant Seal Tags 53
  - 3.2.2 Biogeochemical Floats 56
- 3.3 Methods 57
  - 3.3.1 Profile Fits and Deep Chl-a Maxima 60

3.3.2 Unevenness Indeces 63
3.3.3 Mixed-layer Depth 65
3.4 Results 66
3.4.1 Deep Chl-a Fluorescence Maxima 66
3.4.2 Deep Chl-a Maximum Depth and Mixed-layer Depth 68
3.4.3 Chl-a Variability in the Mixed Layer 70
3.5 Discussion and Conclusions 73
3.6 Appendix 76
3.7 Acknowledgments 78

Chapter 4 Wind modulation of upwelling at the shelf-break front off Patagonia: Observational evidence 79
4.1 Introduction 80
4.2 Background: General characteristics of the Patagonian shelf and physical mechanisms for shelf-break upwelling 85
4.3 Data and Methods 89
4.3.1 Satellite data 89
4.3.2 *In situ* observations 91
4.4 Results and Discussion 95
4.4.1 Composites of satellite Chl-a by wind direction . . . 95
4.4.2 Isopycnal tilting, changes in stratification and *in situ* Chl-a: synoptic evidence 97
4.4.3 Isopycnal tilting and changes in stratification: statistical significance 103
4.4.4 Water-column response to along-front winds 106
4.5 Further Discussion 109
4.6 Conclusions 115
4.7 Acknowledgments 117

Chapter 5 Conclusions and future perspectives 119

Bibliography 123

LIST OF FIGURES

Figure 2.1: (a) Mean summer (DJF) Chl-a in mg m^{-3} based on 12 years of satellite Chl-a data (2000-2011). (b) Percentage of weeks with missing values in summer Chl-a data due to cloud and ice coverage, sun glint and low sun angles. 8
Figure 2.2: Schematic of physical processes considered in this study that can lead to entrainment of nutrient-rich, and typically cold sub-surface waters into the euphotic zone. 13
Figure 2.3: Month of maximum Chl-a, based on 12 years of monthly data (2000-2011). 24
Figure 2.4: (a) Mean summer (DJF) MLD and (b) standard deviation of the summer MLD averaged in $2^\circ \times 4^\circ$ bins for the period 2001-2011. 27
Figure 2.5: (a) Mean summer (DJF) winds in m s^{-1} based on 12 years of CCMP wind data (2000-2011). (b) Partial correlation coefficients between daily anomalies of wind speed and SST after removing the effect of Q_{net} for summer data of 2002-2011. 29
Figure 2.6: Local summer (DJF) correlation coefficients between daily anomalies of (a) wind speed and MLD, (b) Q_{net} and MLD, and (c) SST and MLD. 31
Figure 2.7: Local summer (DJF) correlation coefficients between high-pass filtered daily anomalies of (a) Chl-a and wind speed and (b) Chl-a and Q_{net}, considering spatial scales larger than 350 km and timescales of less than 10 days 33
Figure 2.8: (a) Mean summer (DJF) Ekman pumping velocities (w_{Ek}) in m $week^{-1}$, based on weekly data for the period 2000-2011. (b) Standard deviation of summer w_{Ek}. 34
Figure 2.9: Summer (DJF) partial correlation coefficients, controlling for Q_{net}, between weekly anomalies of (a) w_{Ek} and SST, and (b) w_{Ek} and Chl-a, considering spatial scales larger than 350 km $\times$ 350 km and timescales of less than 10 days 35
Figure 2.10: Partial correlation coefficients between (a) weekly anomalies of Chl-a and SST, and (b) high-pass filtered daily anomalies of Chl-a and SST, controlling for the effect of Q_{net}, and considering spatial scales larger than 350 km $\times$ 350 km. 38
Figure 2.11: Summary figure showing pixels were positive anomalies of Chl-a are associated with positive anomalies in wind speed (light blue), negative anomalies in SST (dark green), both positive anomalies in wind speed and negative anomalies in SST (blue), ... 45

Figure 3.1: (a) Locations of Chl-a profiles from elephant seal tags deployed off Kerguelen Is., EM-APEX (white dots) and Argo floats (black dots) with bio-optical sensors, color coded by month of the year when data were collected. 54
Figure 3.2: Examples of Chl-a fluorescence vertical profiles (relative units) fitted to a (a) sigmoid, (b) exponential, (c) Gaussian, (d) Gaussian + sigmoid and (e) Gaussian + exponential. 63
Figure 3.3: (a) Percentage of Chl-a fluorescence profiles with DFM for elephant seals (black), EM-APEX floats (dark grey) and Argo floats (light grey), considering a DFM when a profile was fitted to a Gaussian and showed a prominent peak below the surface 68
Figure 3.4: Two-dimensional probability density of occurrence functions between deep Chl-a-maximum depth (DFMD) and the MLD using a fine-density threshold of (a) 0.005 kg m^{-3}, (b) the density algorithm from *Holte and Talley* (2009), and density thresholds . . . 69
Figure 3.5: (a) Percentage of profiles with DFM above the MLD for different definitions of mixed layer in each month of the year. 70
Figure 3.6: STD index within the MLD (i.e. the standard deviation within the mixed layer normalized by the regional standard deviation) for Chl-a fluorescence (green) and potential density (blue). 72

Figure 4.1: (a) Bathymetry of the Patagonian shelf from GEBCO with schematic of mean circulation, adapted from *Piola and Falabella* (2009). (b) Chl-a amplitude (annual maximum - annual minimum) based on monthly means for the period 2000-2011, ... 82
Figure 4.2: Schematic diagram showing the effect of along-front winds on the upwelling at a shelf-break front, adapted for the Southern Hemisphere and modified from *Siedlecki et al.* (2011). 85
Figure 4.3: Composites of summer Chl-a for (a) southerly winds and (b) northerly winds, based on 4-day averages of CCMP winds for the period 2000-2011. (c) Difference between (a) and (b): 98
Figure 4.4: Mean summer satellite Chl-a for southerly winds (red), northerly winds (blue) and all summer cases (yellow) for the two transects across the shelf-break front shown in Figure 4.3c, in the (a) northern sector and (b) southern sector. 99
Figure 4.5: Satellite Chl-a and surface winds (left), vertical structure of adjusted Chl-a fluorescence (right, color bar) with density contours overlaid in white, for two transects across the shelf break. 101
Figure 4.6: Temperature-Salinity (TS) diagram for stations at the shelf break indicated with white dots in vertical sections of Figure 4.5. . . . 102
Figure 4.7: Mean hydrographic density sections based on vertical profiles sampled with (a) northerly winds (N=78) and (b) southerly winds (N=94) in winter and spring (JJASON), for stations between 38°S and 50°S. 104

Figure 4.8: Scatter plot for the density gradient between 100m and the surface vs the along-front wind component, for stations between 38°S and 44°S. The correlation for the 97 stations at the SBF with CCMP wind data is -0.48, significant at the 99% level. 106
Figure 4.9: (a) Mean sea surface temperature (color bar) with wind vectors overlaid for the period October 16 to December 5 2005, when the mooring site at $\sim$ 44°S indicated by the white dot acquired hourly winds and water column temperature at six depth levels 109
Figure 4.10: Mean (a) temperature, (b) salinity and (c) density profiles at the mooring location(bottom depth at 185 m), averaged over a 24-h period at the end of southerly wind events (in blue), and northerly wind events (in red). 110
Figure 4.11: Lagged cross correlations between meridional winds and temperature (a) at the surface, (b) at 50 m, and (c) 100 m. Positive lags indicate wind is leading with respect to changes in water temperature. 111

LIST OF TABLES

Table 4.1: Summary of *in-situ* observations presented in this study (weblinks for data sources can be found in the Data section and Acknowledgements.) 95

ACKNOWLEDGEMENTS

Chapter 2, in full, is a reprint of the material as it appears in *Journal of Geophysical Research Oceans*: **Carranza M. M.** and Gille S. T. (2015). Southern Ocean wind-driven entrainment enhances satellite chlorophyll-a through the summer, *J. Geophys. Res. Oceans*, 120, doi:10.1002/ 2014JC010203. The dissertation author was the primary investigator and author on this paper.

Chapter 4, in full, has been submitted for publication of the material as it may appear in *Journal of Geophysical Research Oceans*: **Carranza M. M.**, Gille S. T., Piola A. R., Charo M. and Romero S. I. (2016). Wind modulation of the upwelling at the shelf-break front off Patagonia: Observational evidence, *J. Geophys. Res. Oceans*. The dissertation author was the primary investigator and author on this paper.

VITA

2009	B. S. in Physical Oceanography, Faculty of Hard and Natural Sciences - University of Buenos Aires, Argentina
2016	Ph. D. in Oceanography, Scripps Institution of Oceanography - University of California San Diego

PUBLICATIONS

Carranza, M. M., S. T. Gille, A. R. Piola, M. Charo and S. I. Romero (2016). "Wind Modulation of upwelling at the shelf-break front off Patagonia: observational evidence". In revision for Journal of Geophysical Research: Oceans.

Carranza, M. M., and S. T. Gille (2015), "Southern Ocean winddriven entrainment enhances satellite chlorophylla through the summer", J. Geophys. Res. Oceans, 120, doi:10.1002/ 2014JC010203.

Gille, S. T., **M. M. Carranza**, R. Cambra, and R. Morrow (2014), "Wind-induced upwelling in the Kerguelen Plateau region", Biogeosciences, 11(22), 63896400, doi:10.5194/bg-11-6389-2014.

Abbriano, R. M., **M. M. Carranza**, S. L. Hogle, R. A. Levin, A. N. Netburn, K. L. Seto, S. M. Snyder, SIO280, and P. J. S. Franks (2011). "Deepwater Horizon oil spill: A review of the planktonic response". Oceanography, 24(3):294301, http://dx.doi.org/10.5670/oceanog.2011.80.

ABSTRACT OF THE DISSERTATION

On the role of atmospheric forcing on upper ocean physics in the Southern Ocean and biological impacts

by

Magdalena M. Carranza

Doctor of Philosophy in Oceanography

University of California, San Diego, 2016

Professor Sarah T. Gille, Chair

The Southern Ocean (SO) plays a key role in regulating climate by absorbing nearly half of anthropogenic carbon dioxide (CO_2). Both physical and biogeochemical processes contribute to the net CO_2 sink. As a result of global warming and ozone depletion, westerly winds have increased, with consequences for upper ocean physics but little is known on how primary producers are expected to respond to changes in atmospheric forcing. This thesis addresses the impact of atmospheric forcing on upper ocean dynamics and phytoplankton bloom development in the SO on synoptic storm scales, combining a broad range of observations derived from satellites, reanalysis,

profiling floats and Southern elephant seals.

On atmospheric synoptic timescales (2-10 days), relevant for phytoplankton growth and accumulation, wind speed has a larger impact on satellite Chl-a variability than surface heat fluxes or wind stress curl. In summer, strong winds are linked to deep mixed layers, cold sea surface temperatures and enhanced satellite chlorophyll-a (Chl-a), which suggest wind-driven entrainment plays a role in sustaining phytoplankton blooms at the surface. Subsurface bio-optical data from floats and seals reveal deep Chl-a fluorescence maxima (DFM) are ubiquitous in summer and tend to sit at the base of the mixed layer, but can occur in all seasons. The fact that wind speed and Chl-a correlations are maximal at zero lag time (from daily data) and incubation experiments indicate phytoplankton growth occurs 3-4 days after iron addition, suggests high winds in summer entrain Chl-a from a subsurface maximum. Vertical profiles also reveal Chl-a fluorescence unevenness within hydrographically defined mixed layers, suggesting the biological timescales of adaptation through the light gradient (i.e. growth and/or photoacclimation) are often faster than mixing timescales, and periods of quiescence between storms are long enough for biological gradients to form within the homogeneous layer in density.

Directional winds can also modify upwelling/subduction patterns near oceanic fronts. At the shelf-break front off Patagonia, the combined analyses of satellite and in situ observations suggest along-front winds modulate the upwelling on synoptic timescales, potentially through a nutrient pumping mechanism associated with the interaction between along-front wind oscillations and the frontal structure through Ekman transport.

Chapter 1

Introduction

Southern Ocean biogeochemistry plays a key role regulating the climate system, through the uptake of atmospheric carbon (e.g. *Chisholm*, 2000). Both physical and biogeochemical processes contribute to the Southern Ocean carbon sink (e.g. *Morrison et al.*, 2015). However, little is known on how primary producers, that absorb CO_2 by photosynthesis, and the biological component of the carbon cycle are expected to respond to future climate forcing in the Southern Ocean, and biogeochemical models show disagreement in their response (e.g. *Hauck et al.*, 2015). Given that westerly winds in the Southern Hemisphere are projected to increase as a result of global warming (e.g. *Ulbrich et al.*, 2009; *Wang et al.*, 2012), a better understanding of how atmospheric forcing, and winds in particular, impact phytoplankton bloom development will help in projecting how climate change could influence the biological component of the global carbon cycle. This thesis explores the influence of atmospheric forcing on chlorophyll-a (Chl-a) variability in the Southern Ocean, used as a proxy for phytoplankton biomass, from an observational perspective, employing a broad range of observations that come from satellites, reanalyses, cruises, profiling

floats and Southern elephant-seals.

The Southern Ocean is a High Nitrate Low Chl-a (HPLC) region. However, phytoplankton blooms occur seasonally over continental shelves, near islands and oceanic fronts. Phytoplankton accumulation results from the balance between growth and processes that lead to losses (i.e. grazing, mortality, sinking), and upper ocean physics is expected to influence both. Phytoplankton growth in the Southern Ocean is known to be co-limited by iron and light (e.g. *Martin et al.*, 1990a; *Mitchell and Holm-Hansen*, 1991; *de Baar et al.*, 2005). Sources of bioavailable Fe mostly come from the deep ocean, and physical processes that supply iron to the euphotic zone, where phytoplankton can thrive, may influence phytoplankton growth. Stratification and upper ocean mixing will also determine the light levels that phytoplankton are exposed to, as they are mixed through the light gradient. Due to the limited influence of terrestrial input, Southern Ocean waters generally conform to the classical bio-optical classification of Case 1 waters, where phytoplankton are the dominant drivers of optical variability (*Morel and Prieur*, 1977). Thus, phytoplankton often represent the dominant contribution to absorption of light in the Southern Ocean (*IOCCG*, 2015), which makes satellite Chl-a a relatively good proxy for phytoplankton abundance (e.g. *Siegel et al.*, 2013). Within the Southern Ocean temperature decreases with increasing latitude, there is weak density stratification, little summertime surface solar irradiance, and strong wind stress. The combination of these environmental factors result in deep mixing, and generally favors large and pigment-packed phytoplankton species that are well adapted to low light levels (*IOCCG*, 2015).

Atmospheric cyclonic activity shows little seasonality (compared to the Northern Hemisphere, e.g. *Ulbrich et al.*, 2009), and strong winds may impact phytoplank-

ton growth and/or accumulation at the surface by several means. High winds, by deepening the mixed layer through mechanical mixing, can lead to entrainment of nutrients and/or phytoplankton from below the mixed layer. The wind stress curl itself can induce Ekman pumping/suction that can lead to upwelling in the open ocean, particularly south of the maximum westerlies. Wind directionality may also influence upwelling/subduction rates, not only near a coast, but also at oceanic fronts, through the interaction of the associated Ekman transport with the frontal structure. The impacts of all these wind-induced processes on Chl-a variability in the Southern Ocean are evaluated on the scales of atmospheric storm systems (2-10 days, $>$ 300 km) over the open Southern Ocean, as well as over the Patagonian shelf, which is presented as a case study of regional responses.

Chapter 2 looks into the impact of wind speed intensity and surface heat fluxes on Chl-a variability through mixed-layer dynamics in the summer, when presumably nutrients in the euphotic zone become depleted and light is abundant. Mixed layer deepening through enhanced mechanical mixing and wind-stress curl induced upwelling, both of which may lead to nutrient enhancement in the euphotic zone, are evaluated combining satellite Chl-a and winds, and heat fluxes from reanalyses with mixed-layer depth estimates from profiling Argo floats. We find that high winds enhance satellite Chl-a in the summer over most of the open Southern Ocean, potentially through mixed layer deepening.

Ocean color sensors mounted on satellites, however, only give information over the first optical depth, which is roughly the upper 30 m of the water column, and they cannot sense through clouds, imposing severe limitations to studies of biophysical interactions and Chl-a variability in the Southern Ocean. The advent of novel

in situ bio-optical sensors that can be mounted on profiling floats and elephant seals are providing unprecedented measurements that allow us to estimate vertical profiles of Chl-a fluorescence through the upper ocean, throughout the year and under sea ice. Chapter 3 exploits these new measurements from Argo biogeochemical floats and southern elephant seal tags to assess the vertical structure of Chl-a fluorescence in the Southern Ocean. We specifically assess the occurrence of deep Chl-a fluorescence maxima and the vertical structure of Chl-a fluorescence within the mixed layer, where properties are expected to be relatively homogenous. We find, even in the Southern Ocean, where harsh weather conditions presumably lead to deep mixing and homogeneous properties, deep Chl-a fluorescence maxima are not uncommon, and may occur in all seasons. Moreover, Chl-a fluorescence shows variability and gradients within hydrographically defined mixed layers more often than commonly assumed. This implies that the biological timescale of growth/photoacclimation is faster than the mixing timescales. Assuming upper ocean mixing on these scales is largely driven by the winds, this suggests periods of quiescence between storms are long enough to allow biological processes to take place, leading to uneven distributions in hydrographic mixed layers.

Wind directionality can also influence upper ocean processes and upwelling/subduction rates near oceanic fronts, and, in Chapter 4, we investigate the role of wind directionality over the Patagonian shelf-break front as a regional case study. The Patagonian shelf off the eastern coast of South America is particularly relevant because it is the hottest spot in satellite Chl-a images of the Southern Ocean. Phytoplankton in the Patagonian shelf sustain the largest marine ecosystem in the Southern Hemisphere, and the high rates of primary production make the region a strong sink

of atmospheric CO_2. A 1500-km long persistent band of high Chl-a along the shelf break is indicative of upwelling, but the mechanisms that drive such upwelling are not entirely known. Leveraging from satellite data and the existing observations in the region, we look into the impact of directional wind forcing on Chl-a variability at the shelf-break front (SBF) off Patagonia. Results show that along-front winds modulate the Chl-a signal at the SBF on synoptic timescales, consistent with a pumping mechanism associated with the interaction of oscillating along-front winds with the frontal isopycnals. This study reveals along-front wind variability on synoptic scales as a possible forcing mechanism that can drive variability in phytoplankton activity and should be considered in future studies of upwelling at the SBF off Patagonia, while contributing to the understanding of shelf-slope exchange processes.

Chapter 2

Wind-driven entrainment enhances summer chlorophyll-a in the Southern Ocean

Despite being the largest High Nitrate Low Chlorophyll (HNLC) region, the Southern Ocean sustains phytoplankton blooms through the summer, when presumably there is sufficient light, but nutrients in the euphotic zone have been depleted. Physical processes that can potentially supply nutrients from subsurface waters to the euphotic zone, and promote phytoplankton growth in the summer, have not been fully explored at the large scale. By means of a correlation analysis, this study combines high-resolution satellite observations of ocean color, winds and sea surface temperature (SST), surface heat fluxes from reanalysis and Argo mixed-layer depth (MLD) estimates to explore the role of the atmospheric forcing (i.e. winds and surface heat fluxes) on upper-ocean processes that may help sustain high satellite chlorophyll-a (Chl-a) through the summer. Two physical processes that can supply nutrients to

the euphotic zone are: MLD deepening, caused by wind-mixing and/or surface cooling, and Ekman pumping driven by the wind stress curl. We find that high winds correlate with high Chl-a over broad open ocean areas, suggesting that transient MLD deepening through wind-mixing (i.e. wind-driven entrainment) helps sustain high Chl-a. Wind-driven entrainment plays a dominant role on timescales associated with atmospheric synoptic storms (i.e. < 10 days) and has a larger influence on surface Chl-a than storm-scale local Ekman pumping. Based on our analysis of statistically significant correlation patterns, we identify regions in the Southern Ocean where wind-induced entrainment may play a role in sustaining summer phytoplankton blooms.

2.1 Introduction

The Southern Ocean plays a key role in regulating climate by sequestering atmospheric CO_2 through both the solubility and biological pumps (e.g. *Martin et al.*, 1990b; *Chisholm*, 2000; *Tréguer and Pondaven*, 2001; *Marinov et al.*, 2008). It is a High Nitrate Low Chlorophyll (HNLC) region where phytoplankton abundance is primarily iron (Fe) limited (*Martin et al.*, 1990a; *Boyd*, 2002; *de Baar et al.*, 2005). Although HNLC conditions abound in the Southern Ocean, phytoplankton blooms occur annually close to continental shelves and major islands, as well as in open ocean regions. Satellite observations and many studies based on *in situ* measurements have shown blooms that persist through the summer (e.g. *Blain et al.*, 2007; *Korb et al.*, 2008; *Frants et al.*, 2013, see also Figure 2.1a). In this work we investigate physical mechanisms that may be responsible for sustaining phytoplankton blooms through the summer, when in most Southern Ocean locations Fe in the euphotic zone has been

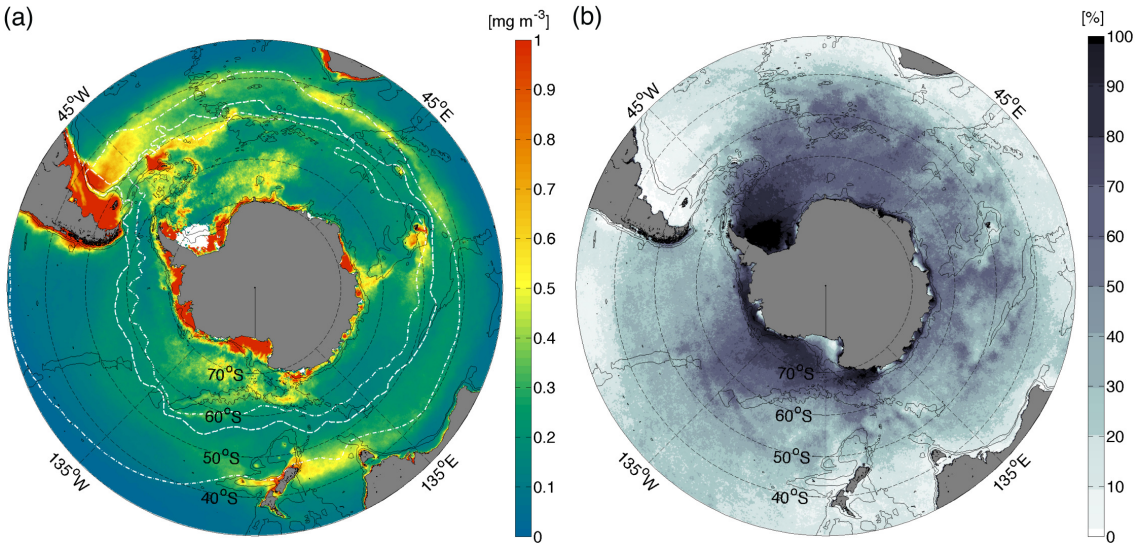

Figure 2.1: (a) Mean summer (DJF) Chl-a in mg m^{-3} based on 12 years of satellite Chl-a data (2000-2011). (b) Percentage of weeks with missing values in summer Chl-a data due to cloud and ice coverage, sun glint and low sun angles. Thin black lines show the bathymetric contours of 1000 and 3000 m. The mean positions of the Subtropical (STF), Sub-Antarctic (SAF) and Polar Fronts (PF, from north to south) are shown with white contours (from *Orsi et al.*, 1995).

depleted (e.g. *Sedwick et al.*, 2011; *Tagliabue et al.*, 2014). Considering that for at least three months of the year the HNLC Southern Ocean is not light limited (*Venables and Moore*, 2010), prolonged phytoplankton blooms likely require a continuous supply of Fe to surface waters.

Several sources of Fe to the euphotic zone have been identified in the Southern Ocean (*Boyd and Ellwood*, 2010). These include Fe from dust deposition events, Fe that is recycled within the euphotic zone due to remineralization of organic matter, and Fe brought up to the surface from subsurface waters by means of physical processes. In seasonally ice-covered Antarctic waters, icebergs and sea-ice melting constitute an additional source of Fe (*Sedwick and Ditullio*, 1997; *Fennel et al.*, 2003; *Lancelot et al.*, 2009). Phytoplankton use primarily dissolved inorganic Fe (*Sunda*

and Huntsman, 1995), while dust particles are dominated by minerals of Fe (*Boyd and Ellwood*, 2010) and are not thought to be a major Fe source for most of the Southern Ocean (e.g. *Meskhidze et al.*, 2007; *Wagener et al.*, 2008). Because the solubility of Fe from dust is low (*Luo et al.*, 2005; *Boyd et al.*, 2010; *Baker and Croot*, 2010), *Jickells* (2005) suggested there must be a large flux of particulate Fe through the deep ocean, particularly beneath the major dust plumes, that can potentially increase dissolved Fe concentrations at depth and, over the long term can increase productivity in upwelling regions such as the Southern Ocean.

Despite abundant macronutrients such as nitrate, silicate-(Si)-depleted waters north of the Sub-Antarctic Front (SAF) can prevent growth of large phytoplankton (i.e. diatoms) and Fe-Si co-limitation may occur (e.g. *Hoffmann et al.*, 2008; *Martin et al.*, 2013). In the summertime, even nitrate may become depleted, especially to the north of the Sub-Tropical Front (STF, *Pollard et al.* (2002)). Hereafter, we will use the word nutrients when referring to the limiting nutrient, which based on observations could potentially be Fe, Si or nitrate depending on the region.

Nutrient supply in the Southern Ocean is thought to be controlled by ocean dynamics (e.g. *de Baar et al.*, 1995; *Hense et al.*, 2003; *Fennel et al.*, 2003; *Moore*, 2004; *Meskhidze et al.*, 2007). Physical processes such as mixing, upwelling, horizontal advection, secondary circulation associated with mesoscale features (i.e. eddies and fronts), and entrainment due to changes in the mixed-layer depth (MLD), all can contribute to the supply of nutrients to the euphotic zone. In this study, we focus on physical processes controlling the vertical exchange of nutrients from subsurface reservoirs to the euphotic zone through MLD dynamics.

The MLD controls nutrient availability as well as phytoplankton exposure to

light and thus is of great relevance for phytoplankton growth (e.g. *Sverdrup*, 1953; *Mitchell and Holm-Hansen*, 1991). The level of mixing and turbulence in the upper ocean can also influence grazing rates (*Behrenfeld*, 2010) and has consequences for the redistribution and accumulation of phytoplankton itself within the mixed layer, which may lead to surface blooms regardless of the depth of the mixed layer (*Taylor and Ferrari*, 2011a). Despite the recent debate on the extent to which the MLD is relevant for phytoplankton bloom development (*Behrenfeld*, 2010; *Taylor and Ferrari*, 2011a; *Chiswell*, 2011), the atmospheric forcing that sets up stratification and mixing in the upper ocean on timescales relevant to phytoplankton growth and accumulation (days to weeks) likely impacts surface phytoplankton blooms.

On time scales of days to weeks, the MLD is largely determined by the turbulent mixing caused by the winds, and buoyancy forcing. Entrainment of nutrient-rich and sub-mixed-layer waters, which are typically cold, occurs when the mixed layer deepens. Numerical models and observational evidence show that wind-induced mixing events accompanied by deepening, and/or erosion of the seasonal thermocline can significantly increase nutrient concentrations in the euphotic zone (*Klein and Coste*, 1984; *Eppley and Renger*, 1988; *Marra et al.*, 1990; *Lévy et al.*, 2009). Nutrient entrainment to the mixed layer follows the wind action with a time lag of hours, which decreases with stronger winds (*Klein and Coste*, 1984), and because phytoplankton populations can double more than once per day, and phytoplankton grazers are capable of population increases at much higher rates (i.e. up to five doublings per day, e.g. *Miller et al.* (1991); *de Baar et al.* (2005)), the response of phytoplankton is expected to be concomitant with wind-driven entrainment at daily scales. In extratropical latitudes, modeling studies show that changes in the MLD and the heat flux

through the base of the mixed layer play an important role in the development of sea surface temperature (SST) anomalies in the summer, when the entrainment rate is generally dominated by wind-induced mixing (*Alexander et al.*, 2000). In addition, the wind-stress curl drives vertical velocities via Ekman pumping and can modulate the entrainment process (e.g. *McPhaden et al.*, 2008).

Global studies have shown that winds have a measurable influence on satellite chlorophyll-a (Chl-a) variability (*Kahru et al.*, 2010). In most parts of the global ocean high wind speeds correlate with high Chl-a, implying either that winds deepen the mixed layer resulting in more nutrients being entrained into the upper ocean promoting phytoplankton growth, or alternatively that winds mix the deep Chl-a maximum up to the surface. This is not the case in the Southern Ocean where wind speed and Chl-a tend to be negatively correlated on monthly to seasonal timescales (*Fitch and Moore*, 2007; *Kahru et al.*, 2010). The most plausible explanation for the inverse relationship is that in regions with very deep mixed layers in late winter, strong winds tend to deepen the mixed layer enough to remove phytoplankton from the euphotic zone and thus reduce their mean light levels, impacting their growth rates. Although the MLD is shallowest in the summer, the water just below the seasonal mixed layer has potentially low stratification, and small anomalous increases in summer winds can therefore easily remix the upper layer, reestablishing deep mixed layers, which would tend to decrease Chl-a (*Kahru et al.*, 2010). The suggested inverse relationship between Chl-a and MLD is in agreement with the relationship observed between Fe-addition experiments (*de Baar et al.*, 2005), where those in the Southern Ocean associated with deeper mixed layers showed lower surface Chl-a values.

The Southern Ocean is exposed to strong surface winds associated with the

high atmospheric synoptic activity that characterizes the Southern Hemisphere all year round (*Hoskins and Hodges*, 2005). The Southern Annular Mode (SAM) has intensified in response to Antarctic ozone depletion, leading to stronger surface westerlies, particularly during austral summer (*Thompson et al.*, 2011), when coincidentally phytoplankton blooms tend to peak. Because the deepening of the MLD has the potential to entrain nutrients and promote phytoplankton growth when light is not limiting, the MLD may play a critical role in the summer if mixing events are strong enough to deepen the mixed layer. We will show that, despite strong summer winds, summer MLDs do not vary substantially from the seasonal mean. They are shallower and closer to the euphotic depth, potentially allowing for anomalous deepening of the seasonal MLD to entrain nutrients efficiently.

The purpose of this study is to explore the influence of atmospheric synoptic storms on summer phytoplankton abundance in the Southern Ocean.s We focus on the roles of winds and buoyancy forcing, which can deepen the mixed layer resulting in entrainment from below the base of the mixed layer. We also explore the contribution of Ekman-induced upwelling to the entrainment process. A schematic of the physical processes considered is shown in Figure 2.2. Our approach is a correlation analysis that combines data drawn from a broad range of sources including satellite data, reanalysis and Argo floats. We correlate high resolution physical variables that can elucidate the dynamics of the MLD with satellite Chl-a, which serves as a proxy for phytoplankton biomass. Because over coastal areas and close to islands/plateaus along the Antarctic Circumpolar Current (ACC) pathways the dynamics are expected to be influenced by other processes that are not necessarily wind-related, we focus our analysis on open ocean phytoplankton blooms. Based on our analysis of statistically

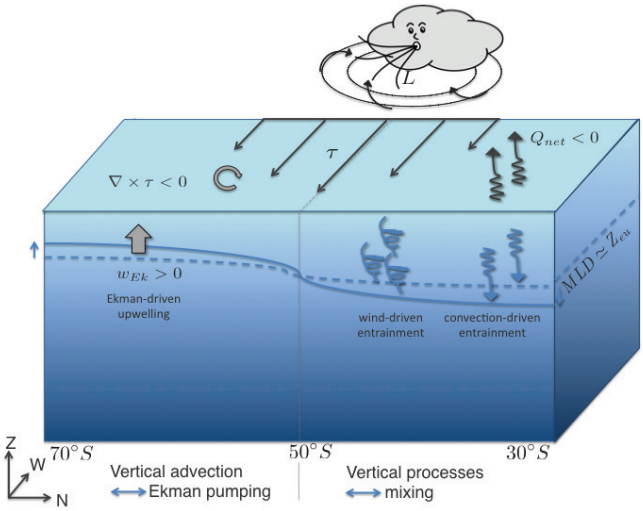

Figure 2.2: Schematic of physical processes considered in this study that can lead to entrainment of nutrient-rich, and typically cold sub-surface waters into the euphotic zone. MLD: mixed layer depth, Z_{eu}: euphotic depth, τ: wind stress, Q_{net}: net heat fluxes and w_{Ek}: Ekman pumping.

significant correlation patterns, we identify regions in the Southern Ocean where wind-induced entrainment may play a role in sustaining summer blooms.

2.2 Data and methods

The entrainment rate of any given property at the base of the mixed layer, h, can be written as (e.g *de Szoeke*, 1980; *Musgrave et al.*, 1988; *Close and Goosse*, 2013):

$$w_e = \frac{\partial h}{\partial t} + w_{Ek}(h), \tag{2.1}$$

where the first term in the right hand-side represents turbulent entrainment as the MLD deepens, and the second term is a modulation of entrainment caused by non-

turbulent vertical advection due to Ekman pumping (w_{Ek}). Deepening of the MLD can be caused by wind-induced mixing and/or surface cooling, two processes that can generate turbulence at the base of the mixed layer. On the other hand, w_{Ek} represents the vertical displacement of the material surface that defines the base of the mixed layer, solely as a result of mixed-layer divergences driven by wind-stress curl ($w_{Ek} = \nabla \times \tau/\rho f$). In the Southern Hemisphere where $f < 0$, Ekman-induced upwelling (i.e. Ekman suction, $w_{Ek} > 0$) occurs when the wind-stress curl is negative. Both contributions to the entrainment rate are tightly linked to the atmospheric forcing, for which satellite and reanalysis data are available, allowing us to address the potential impact of these processes in a large-scale context.

2.2.1 Satellite data

At least weekly temporal sampling is needed in order to capture variability driven by fast-moving atmospheric storm systems and phytoplankton turnover. Here we use 9 years of daily and weekly (i.e. 8 days) satellite estimates of Chl-a, SST and winds for the period June 2002 to May 2011 when all observations are available. The start and end of this period are dictated by the Advanced Microwave Scanning Radiometer (AMSR-E), which is used for SST. In our analysis, we only include data from the austral summer months (December, January and February, DJF) that comprise a total of 812 days.

Chl-a is used as a proxy for phytoplankton biomass. Although in some regions of the world's oceans Chl-a may respond more closely to physiological changes rather than phytoplankton biomass, in the Southern Ocean, Chl-a and phytoplankton carbon are well correlated (*Le Quéré et al.*, 2002; *Behrenfeld et al.*, 2005; *Arrigo et al.*,

2008). We use Chl-a data from multiple sensors merged by the European Space Agency's GlobColour project. The data are reported on a 25 km $\times$ 25 km grid, and are determined using the bio-optical model described by *Maritorena and Siegel* (2005). The main advantage of using the merged product is the increased number of observations in the Southern Ocean, where persistent cloud coverage represents an obstacle for ocean color sensors. Cloudiness shows a pronounced seasonal cycle over the Southern Ocean with higher cloud incidence during the winter season (*Verlinden et al.*, 2011), when Chl-a values are presumably low. In addition to clouds, ice cover and low sun angles south of 65°S often result in no valid data, and more than half of the year Chl-a cannot be retrieved. However, in the summer the percentage of missing data is significantly reduced, and only regions close to the Antarctic continent are severely impacted by missing data (Fig. 2.1b).

A phytoplankton bloom is generally defined as an increase in Chl-a concentration relative to a threshold value (e.g *Henson and Thomas*, 2007; *Fitch and Moore*, 2007; *Racault et al.*, 2012). *Behrenfeld* (2010) suggests looking at changes in net population growth rates (i.e. $r = \ln(\text{Chl-a}_{t1}/\text{Chl-a}_{t0})/\Delta t$) rather than biomass (i.e. Chl-a). In the Southern Ocean, the use of net phytoplankton growth rates significantly limits the number of observations, even when considering 4-day averages to compute initial and final Chl-a values for a given week. Here we are interested in intra-seasonal variability and use Chl-a anomalies relative to a climatological mean to preserve the highest possible temporal resolution. We find that the absolute value criterion (e.g. Chl-a > 0.8 mg m^{-3} in *Fitch and Moore* (2007)) misses small-amplitude phytoplankton blooms, and for this study we consider positive Chl-a anomalies to be indicative of a bloom. The criterion we use captures more open ocean blooms, where

winds and the dynamics of the mixed layer are likely to play a major role in sustaining high Chl-a.

Chl-a anomaly maps were computed for each day and week using the ratio of observed Chl-a to a multi-year time mean and expressed as a percentage, i.e.:

$$\text{Chl-a}' = \frac{\ln(\text{Chl-a}) - \overline{\ln(\text{Chl-a})}}{\overline{\ln(\text{Chl-a})}} \times 100. \tag{2.2}$$

Since Chl-a is approximately log-normally distributed, we use a geometric mean (i.e. $\overline{\text{Chl-a}} = \exp\left(\overline{\ln(\text{Chl-a})}\right)$ to compute mean values whenever necessary. The use of the log-normal distribution as a model for the variability of Chl-a has been supported both empirically and theoretically (*Campbell*, 1995). This assumption works well if the variance is relatively low (*IOCCG*, 2004). However, in many cases Chl-a binned data show a bimodal structure. We find that our results are not sensitive to the way in which Chl-a anomalies were calculated, and the quantity Chl-a $-\overline{\text{Chl-a}}$ yields similar correlation patterns.

In the range of Chl-a values typical for the Southern Ocean (0.2-2 mg m^{-3}), satellite Chl-a algorithms tend to underestimate Chl-a by a factor of 2-5 compared to *in situ* measurements (*Kahru and Mitchell*, 2010; *Guinet et al.*, 2013). Surface Chl-a may also underestimate vertically integrated values of Chl-a for the euphotic zone due to subsurface maxima (*Holm-Hansen et al.*, 2005; *Knox*, 2007; *Arrigo et al.*, 2008). Assuming an absolute bias offset that is uniform across the Southern Ocean, systematic underestimation of Chl-a will not impact our results, since the analysis of correlation patterns is based on anomalies.

We use the Cross-Calibrated Multi Platform (CCMP) ocean surface winds. These winds are produced using a variational analysis method that blends data from

multiple satellites (*Atlas et al.*, 2011a). CCMP winds are available on 25 km × 25 km grids and are distributed by the Physical Oceanography Distributed Active Archive Center (PO.DAAC). By taking advantage of the differences in the orbits between the platforms and sampling times, they provide reliable wind fields at 6-hour temporal resolution. In comparison with observations from the Stratus buoy (20° S, 85° W), CCMP winds provided higher coherence at high frequencies than single satellite observations for QuikSCAT, WindSat or ASCAT winds. CCMP winds yielded higher correlations with MLD than did other wind products, and in this paper, only results from CCMP winds are presented.

To compute w_{Ek}, wind stress was estimated following *Risien and Chelton* (2008) from the meridional and zonal components of the wind. Wind-stress curl fields were computed using spherical coordinates and smoothed using a moving block average with a flat kernel of 4 × 6 grid cells, resulting in an effective resolution of 100 km × 150 km (results were not sensitive to the choice of boxcar versus circular or Gaussian filter).

We use microwave SSTs from the AMSR-E instrument carried on board the Aqua satellite. These data are provided by Remote Sensing Systems (RSS) on a 25 km × 25 km grid (version 7). Microwave SSTs are not strongly affected by clouds, in contrast with infrared SSTs or ocean color, both of which provide gappy data in the Southern Ocean due to persistent cloud cover. Missing data in AMSR-E SST are due to high wind speed (> 20 m s^{-1}), sun glint, rain, sea ice or proximity to land. The AMSR-E measurements tend to overestimate SST due to undetected ice, and in summer they have been shown to be warmer than *in situ* observations (*Dong et al.*, 2006), whereas infrared SSTs tend to underestimate surface temperature due

to cloud contamination. For completeness, we also tested daytime infrared SSTs from the Moderate Resolution Imaging Spectroradiometer (MODIS-T on Terra). MODIS-T SSTs yield similar results in correlation coefficients between the variables, albeit with larger statistical uncertainties because of data drop-outs due to cloud cover.

2.2.2 Reanalysis data

For surface heat fluxes we use the coupled global NCEP Climate Forecast System Reanalysis (NCEP/CFSR, *Saha et al.* (2010a)). This reanalysis provides higher resolution (1 hour and $0.5^\circ \times 0.5^\circ$) compared with previous reanalysis. Since NCEP/CFSR reanalysis incorporates satellite measurements, especially in the Southern Hemisphere, the accuracy increases over time (*Saha et al.*, 2010b), and the net ocean surface heat flux (Q_{net}) has smaller biases than the NCEP/NCAR reanalysis (*Xue et al.*, 2011). Here positive Q_{net} is defined as flux into the ocean (i.e. the ocean heats). Although CFSR reanalyses show significant improvements over previous reanalyses (*Xue et al.*, 2011), remaining uncertainties in the surface heat fluxes could impact our results. To gain confidence in our results we repeated the analyses using the ERA-Interim heat fluxes from the European Centre for Medium-Range Weather Forecasts (ECMWF), and overall results did not change.

2.2.3 Argo mixed-layer depth

Most large-scale studies that address physical mechanisms responsible for the observed patterns in satellite Chl-a rely on numerical models or ocean reanalysis when considering the effect of stratification and MLD dynamics (e.g. *Llido et al.*, 2005; *Alexander et al.*, 2008; *Behrenfeld*, 2010; *Fauchereau et al.*, 2011). Here, we use *in-*

situ MLD estimates for 48,588 summer Argo profiles in the Southern Ocean during the period 2001-2011 (*Holte et al.*, 2010). The number of Argo profiles increased substantially over time (from 35 in 2001 to > 1,807 in 2004, and > 7,974 in 2011). *Holte and Talley* (2009) provided 5 MLD estimates. In summer, differences between these are typically less than 10 m (*Dong et al.*, 2008; *Stephenson et al.*, 2012), and all definitions of the MLD produced similar patterns when correlated with other variables. Here we show results based on the density threshold criterion of 0.03 kg m^{-3} (*de Boyer Montégut et al.*, 2004). In winter months *Stephenson et al.* (2012) showed ocean heat content to provide a better measure of upper ocean variability than MLD, but for this summer-oriented study we focus on MLD, since MLD can influence nutrient availability in the euphotic zone.

2.2.4 Statistical analysis

To explore the influence of atmospheric storms on upper ocean physics and summer Chl-a variability, we compute maps of local correlation coefficients between anomalies of Chl-a and physical variables: wind speed, Q_{net}, w_{Ek} and SST. At each grid cell a time series of anomalies of each of these variables was constructed (except for w_{Ek}), from which local correlation coefficients were computed.

To match the spatial resolution of all data sets, we have chosen to coarsen the resolution of Chl-a, SST and winds to match that of surface heat fluxes by bin averaging into a $0.5^\circ \times 0.5^\circ$ grid.

Because MLD deepening due to turbulent processes and Ekman-induced upwelling may be expected to operate on different timescales (*de Szoeke*, 1980), we tested both daily and weekly correlations. For most of the analysis shown, we use

daily anomalies calculated by subtracting monthly climatological means in order to eliminate the seasonal variability and long-term trends. When using weekly anomalies, we removed the muti-year weekly means.

Consecutive data dependence of daily data can reduce the number of degrees of freedom and impact the evaluation of statistical significance. To make significance more robust when testing for daily correlations, we high-pass filtered the data in time using a cut-off frequency of 10 days chosen to highlight the effects of synoptic storm systems (*Vera*, 2003). Missing data in daily fields were linearly interpolated in time prior to filtering and subsequently padded as missing values. For daily correlations, we show results obtained by subtracting from the original time series of anomalies the low-pass filtered time series using an 11-point moving average run forward and backward to preserve the phase (i.e a 21-point triangular filter). Other filters commonly used to extract the variability associated with the atmospheric synoptic scale were also tested (e.g a Butterworth 4-pole filter following *Nakamura et al.* (2002)) and gave qualitatively similar results.

The SAM and El Niño Southern Oscillation (ENSO) are the dominant modes of climate variability in the Southern Ocean, and both can influence upper ocean dynamics and Chl-a (e.g *Le Quéré et al.*, 2002; *Lovenduski and Gruber*, 2005; *Sallée et al.*, 2010). Here, we are interested in the response of Chl-a to local wind forcing, and we high-pass filter the data in the time domain to minimize the impact of low-frequency or remote coupled ocean-atmospheric forcings. High-frequency variability associated with the SAM (e.g *Baldwin*, 2001) may remain in high-pass filtered timeseries. Our results, however, are largely unchanged if we specifically remove the variability associated with SAM and ENSO from all anomaly time series by subtract-

ing the least squares regression onto SAM and ENSO indices.

Oceanic mesoscale features can significantly modify upper ocean physics and biology and are marginally resolved at 25-km resolution. Consistent with the first baroclinic Rossby deformation radius, satellite Chl-a shows mesoscale structures smaller than 175 km south of 30° S that are comparable to decorrelation scales of altimetry and SST data (*Krauss et al.*, 1990; *Stammer*, 1998; *Doney*, 2003). The anisotropy found in altimeter data is, however, less apparent in Chl-a mesoscale variability (*Doney*, 2003). To suppress oceanic mesoscale processes in our data, we spatially smooth anomaly fields of all variables using a rectangular window of 14 x 14 grid points (350 km x 350 km). For Chl-a, we smoothed ln(Chl-a) and the geometric means prior to computing anomalies to avoid unrealistic large values. Given that mean currents in the ACC are roughly 20 cm s^{-1} (or 17 km day^{-1}), at daily scales and 175 km effective resolution, advection can be neglected, and the correlation patterns reflect local processes.

When testing for a dependence relation between the variables, we use the non-parametric Spearman correlation coefficient (*Gibbons*, 1985) because it does not assume prior knowledge of the probability distribution function to determine statistical significance and it is less sensitive to outliers. Spearman's test has difficulties when the sample size is very small and therefore we compute correlations only when N>10.

SST is often used as a proxy for nutrients with the implicit assumption that SST variability is associated with upwelling or entrainment. However, there are multiple feedbacks between the oceanic and atmospheric boundary layers through changes in surface heat fluxes that can impact the SST and other physical variables. To avoid

spurious correlations, for parts of this study we compute partial correlations (see e.g. *Box et al.*, 1994). Partial correlations measure the degree of association between two variables with the effect of a controlling variable removed. The method essentially involves a correlation between the residuals that result from the linear regression of each variable against the controlling variable.

In this study we are mostly interested in the sign of correlations and the processes that may be driving the observed patterns. The magnitude of a change in SST that is expected given an increase in winds may be useful, for instance, for the design of observational experiments at sea. In the auxiliary material, we also supply slopes of the linear regression model for all significant correlations presented here.

To address how much of the summer MLD variability observed in Argo is accounted for by surface forcing, we correlate anomalies of the MLD with anomalies of wind speed, Q_{net} and SST. For each profile, MLD anomalies were computed relative to a summertime mean MLD field (Fig. 2.4a), constructed by averaging Argo MLD estimates onto a $2^\circ \times 4^\circ$ grid for the summer season. The number of Argo estimates averaged in each bin is shown in Figure 2.4c. Climatological monthly MLDs were also considered but these resulted in significant data loss due to the poorer coverage in monthly mean MLD maps. To correlate MLD anomalies with satellite variables, we found the closest observations of the physical variables in space and time that matched with the location and time of the Argo profiles in $2^\circ \times 4^\circ$ bins, and within a time window of 3 days. Because time series of data pairs in each bin are constrained by the availability of Argo profiles and, therefore, very gappy, we chose not to spatially smooth or high-pass filter the data in time when correlating against MLD. However, a correlation test using filtered satellite and reanalysis fields against unfiltered MLD

anomalies yields similar results.

2.3 Results

2.3.1 Southern Ocean phytoplankton blooms

Mean summer Chl-a based on 12 years of ocean color data is shown in Figure 2.1. Large values in Chl-a are found over most of the continental shelves (> 1 mg m^{-3}, e.g. around South America and the Antarctic continent), downstream of Drake Passage and near major islands (e.g. Kerguelen Plateau, South Georgia and South Sandwich Islands, Crozet Islands) but also relatively large values (> 0.4 mg m^{-3}) are observed in open ocean areas sometimes associated with the mean position of frontal features (e.g. in the STF, over the western part of ocean basins, along the northern most dashed white line in Figure 2.1a). These areas of high Chl-a coincide with areas of elevated surface particulate organic carbon and primary production in the Southern Ocean (*Moore and Abbott*, 2000; *Sokolov and Rintoul*, 2007; *Arrigo et al.*, 2008; *Allison et al.*, 2010). The asymmetry in Chl-a along the 40-50° S band between the Atlantic-Indian sector and the eastern Pacific was noted by *Thomalla et al.* (2011), who attributed the lower Chl-a values in the Pacific to limited Fe supply from the deep due to relatively shallower winter mixed layers.

Although bloom initiation in the Southern Ocean south of $\sim 40°$ S occurs in the spring (Sep-Nov, *Thomalla et al.*, 2011), elevated values of Chl-a can persist for more than 12 weeks (*Racault et al.*, 2012). In Figure 2.3 we show the month of occurrence of maximum Chl-a based on the climatological annual cycle (i.e. averaged monthly mean maps of Chl-a). We also calculated the most frequent month of occurrence of

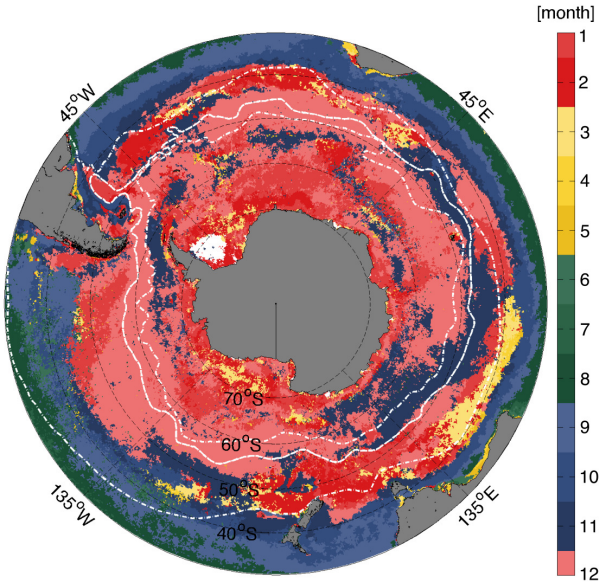

Figure 2.3: Month of maximum Chl-a, based on 12 years of monthly data (2000-2011). The mean positions of the STF, SAF, and PF (from north to south) are shown with white contours (from *Orsi et al.*, 1995).

the peak by keeping track of the month of maximum for each year in the record and computing the mode, and a similar structure was obtained. Chl-a tends to peak in the summer over large areas (red tones in Figure 2.3) within the ACC, whereas to the north of the ACC Chl-a tends to peak in the spring (blues in Figure 2.3). To the north of the STF, Chl-a reaches its maximum in winter (dark greens in Figure 2.3) when the MLD is deepest (70-100 m in the Atlantic and Pacific and somewhat shallower in the subtropical Indian sector), and its minimum in the summer when the MLD is shallowest ($\sim$ 40 m, see Figure 2.4a). This agrees with the findings of *Thomalla et al.* (2011), who carried out a detailed analysis of the seasonal cycle of Chl-a in the Southern Ocean, showing that the bloom initiation progresses meridionally with the latitudinal progression in light intensity (*Racault et al.*, 2012).

Regional differences in the phasing of the seasonal cycle suggest nutrient limitation may be more pronounced during different times of the year depending on the

location. Thus, the summer season based on the calendar year may not resemble a nutrient-limited regime everywhere in our domain. For example, north of the STF where Chl-a reaches its maximum in late winter, a nutrient-limited regime will likely be more pronounced in the spring. As an alternative to the DJF definition of summer, we also considered the two months that follow the month of the Chl-a peak in the annual cycle for our analysis, defining a summer-like season for each grid cell that best represents the time of the year when phytoplankton growth is presumably nutrient limited. Correlations based on the summer-like season give slightly larger values north of the STF, but overall patterns remain unchanged and, throughout this paper results we show are for the austral summer months (DJF).

2.3.2 Summer atmospheric forcing and MLD variability

In this section, we examine the impact of atmospheric forcing (i.e. winds and surface heat fluxes) on summertime MLD dynamics, since this is a key step to evaluate how anomalies in Chl-a are related to physical forcing.

Winds over the Southern Ocean are strong year round, with little seasonal variation (*Yuan*, 2004; *Gille*, 2005). Mean summer winds are $\sim$12 m s^{-1} in the circumpolar band (Fig. 2.5a), but extremes are much greater. Weekly and daily anomalies can reach up to 10 m s^{-1} and 20 m s^{-1} respectively. In regions where the winds are weaker (i.e. in the subtropical and polar bands) there is considerable gustiness (not shown), and ocean circulation models show the Southern Ocean MLD to be sensitive to gustiness in the winds (*Lee et al.*, 2008).

The MLD is shallowest in the summer (MLD $<$ 90 m, see Figure 2.4a) and closer to the euphotic depth ($\sim$100 m in oceanic waters surrounding Antarctica, *Knox*,

2007), which allows for optimal conditions of light for phytoplankton to grow. As the MLD shallows, strong wind events are more effective in deepening the mixed layer to entrain water from just below the base of the mixed layer. The summer MLD varies substantially in the Southern Ocean (Fig. 2.4b) with a standard deviation ranging from 15 m to 30 m. Variability is highest in regions with deep seasonal mixed layers (Fig. 2.4a). However, Argo data do not show extremely deep summer MLDs. This suggests that in the summer, strong wind events may reduce upper-ocean stratification without completely eroding the seasonal mixed layer.

By enhancing vertical mixing in the upper ocean, strong winds have the potential to entrain cold waters into the mixed layer thus influencing the mixed-layer heat budget (*Bonekamp et al.*, 1999) and producing cold SSTs. This would imply a negative correlation between wind speed and SST anomalies, as discussed by *Price* (1981) for hurricane conditions. However, SST can also induce changes in the winds by setting up instabilities in the marine atmospheric boundary layer (*Wallace et al.*, 1989) with implications for surface heat fluxes. In the extra tropics, *Xie* (2004) interpreted negative correlations between wind speed and SST as indicating that the ocean passively responds to wind-induced latent and sensible heat fluxes. In our analysis, wind speed and SST are also strongly correlated with Q_{net} (not shown). To suppress the effect of surface heat fluxes, in Figure 2.5b we show partial correlations between wind speed and SST controlling for Q_{net}. Statistically significant negative correlations arise over the entire domain, and suggest that SST changes in response to entrainment of subsurface waters. Our correlations indicate wind speed alone can explain as much as 80% of the variance observed in SST.

MLD data from Argo are less numerous than SST or wind data, but they

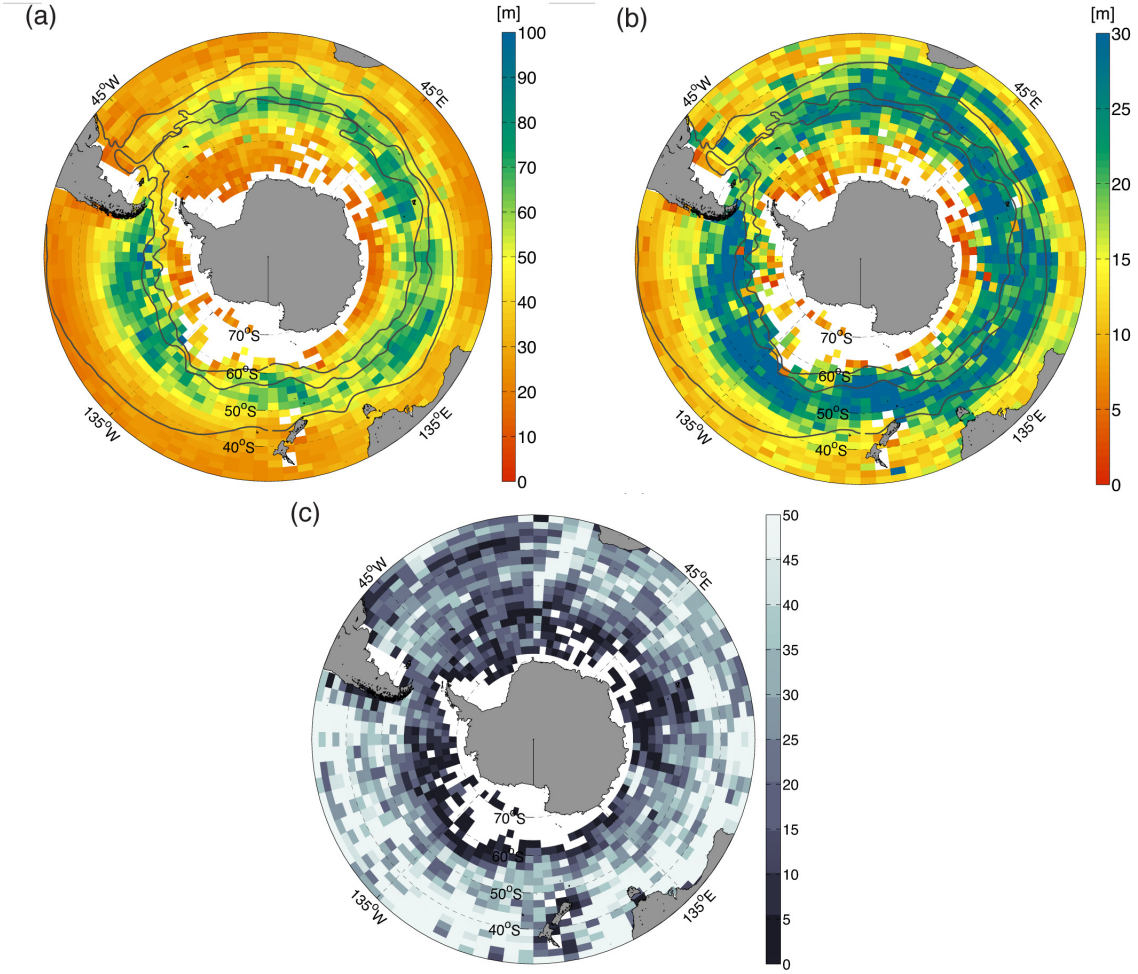

Figure 2.4: (a) Mean summer (DJF) MLD and (b) standard deviation of the summer MLD averaged in 2° × 4° bins for the period 2001-2011. The MLD is defined using a density threshold criteria (threshold of 0.03 kg m^{-3}, following *de Boyer Montégut et al.* (2004)). (c) Number of summer (DJF) Argo MLD estimates averaged in each bin. The mean positions of the STF, SAF, and PF (from north to south) are shown with black contours (from *Orsi et al.*, 1995).

support the hypothesis inferred from the SST versus wind correlation, that strong summer wind events lead to cooler SSTs, because they deepen the mixed layer. Figure 2.6a shows positive correlations between wind speed and MLD throughout the Southern Ocean, implying high winds deepen the mixed layer. To a lesser extent, surface cooling also contributes to deepening the MLD (i.e. negative correlations between Q_{net} and MLD in Figure 2.6b). On average, wind speed explains 21.8% of the MLD variance versus 16.7% explained by Q_{net}. The lower number of statistically significant correlations in Figure 2.6b compared to Figure 2.6a also suggests that in the summer winds have greater influence on MLD than Q_{net}. Correspondingly Figure 2.6c indicates that deep mixed layers are correlated with cold SSTs, supporting the hypothesis that anomalous deep mixed layers permit entrainment of cold water into the mixed layer. Changes in the MLD account for roughly 30% of the SST variance, and therefore SST alone may not be a good proxy for MLD. To suppress feedbacks with the marine atmospheric boundary layer, partial correlation coefficients were also computed. These patterns, based on fewer data points constrained by the availability of three variables, showed fewer bins with statistically significant correlations (not shown) but larger correlation coefficients of the same sign as shown in Figure 2.6. Non-significant correlations to the south of the ACC in Figure 2.6 may reflect both salinity effects that are important due to ice melting in the summer and the scarcity of Argo profiles. Correlations also tend to be non-significant over the Atlantic sector, where the number of available MLD estimates is smaller than in the Pacific (Fig. 2.4c).

To summarize, the results in Figure 2.6 imply that wind speed contributes more than Q_{net} to summer MLD variability, but both variables influence stratification and

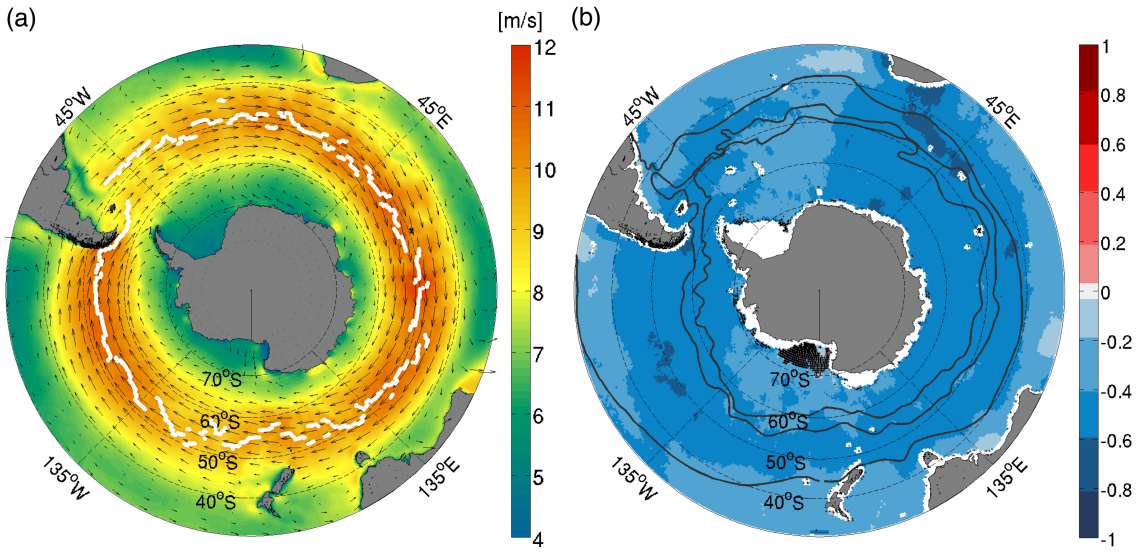

Figure 2.5: (a) Mean summer (DJF) winds in m s^{-1} based on 12 years of CCMP wind data (2000-2011). (b) Partial correlation coefficients between daily anomalies of wind speed and SST after removing the effect of Q_{net} for summer data of 2002-2011. Anomalies were spatially smoothed and high-pass filtered in the time domain to highlight the effect of atmospheric synoptic storms (i.e. spatial scales > 350 km and timescales < 10 days). Dotted areas indicate the correlation is not significant at the 90% level. The white dotted contour in (a) indicates the mean position of the maximum westerlies. The mean positions of the STF, SAF and PF are shown in black contours.

contribute to MLD variance and are thus hypothesized to influence Chl-a.

2.3.3 Effect of MLD deepening on Chl-a

In this section we evaluate how stratification and upper ocean mixing (caused by winds and surface heat fluxes) exert a control on Chl-a variability. If MLD deepening delivers nutrients into the seasonal mixed layer, we expect positive correlations between Chl-a and wind speed anomalies (i.e. wind-driven entrainment) and negative correlations between Chl-a and Q_{net} (i.e. convection-driven entrainment).

To investigate the influence of wind-driven entrainment on Chl-a, we mapped local correlation coefficients between anomalies of Chl-a and wind speed (Fig. 2.7a).

Because the atmospheric synoptic scale associated with storm systems exhibits fluctuations with periods of less than 10 days (*Vera*, 2003), here we use daily anomalies. Compared with weekly data, daily data, although sparser in space and time, yield larger areas with significant correlations between Chl-a and wind speed. Moreover, the direct relationship between wind speed and Chl-a prevails when high-pass filtering daily data in the time domain (see Section 2.4), and these are the results we show in Figure 2.7. Even though winds may be influenced by surface heat fluxes (e.g., through enhanced turbulence in the atmospheric boundary layer), we do not show partial correlations in Figure 2.7, because we are not interested in identifying, for example, whether the high wind correlation is related to surface heat fluxes. Nonetheless, we tested partial correlations in all cases, and the results did not change significantly.

In contrast with the findings of *Kahru et al.* (2010) who used year-round data, in the summer strong wind events show a positive influence on Chl-a over large areas (Fig. 2.7a). Even over regions where we find the deepest mixed layers (e.g the southeast Pacific, see Figure 2.4a), strong winds correlate with high Chl-a (Fig. 2.7a). This may imply summer storms are effective in breaking down stratification enough to entrain nutrients, without completely eroding the seasonal MLD, which would expose phytoplankton to light limitation stress. In particular, the regions to the north of the STF, the eastern Pacific including the region between the PF and SAF west of Drake Passage, and upstream of Kerguelen Plateau show significant positive correlations between wind speed and Chl-a (Fig. 2.7a) that persist on weekly timescales (not shown).

One might hypothesize that Fe-rich dust could be deposited by high wind events, and subsequently dissolve to initiate a bloom leading to positive correlations

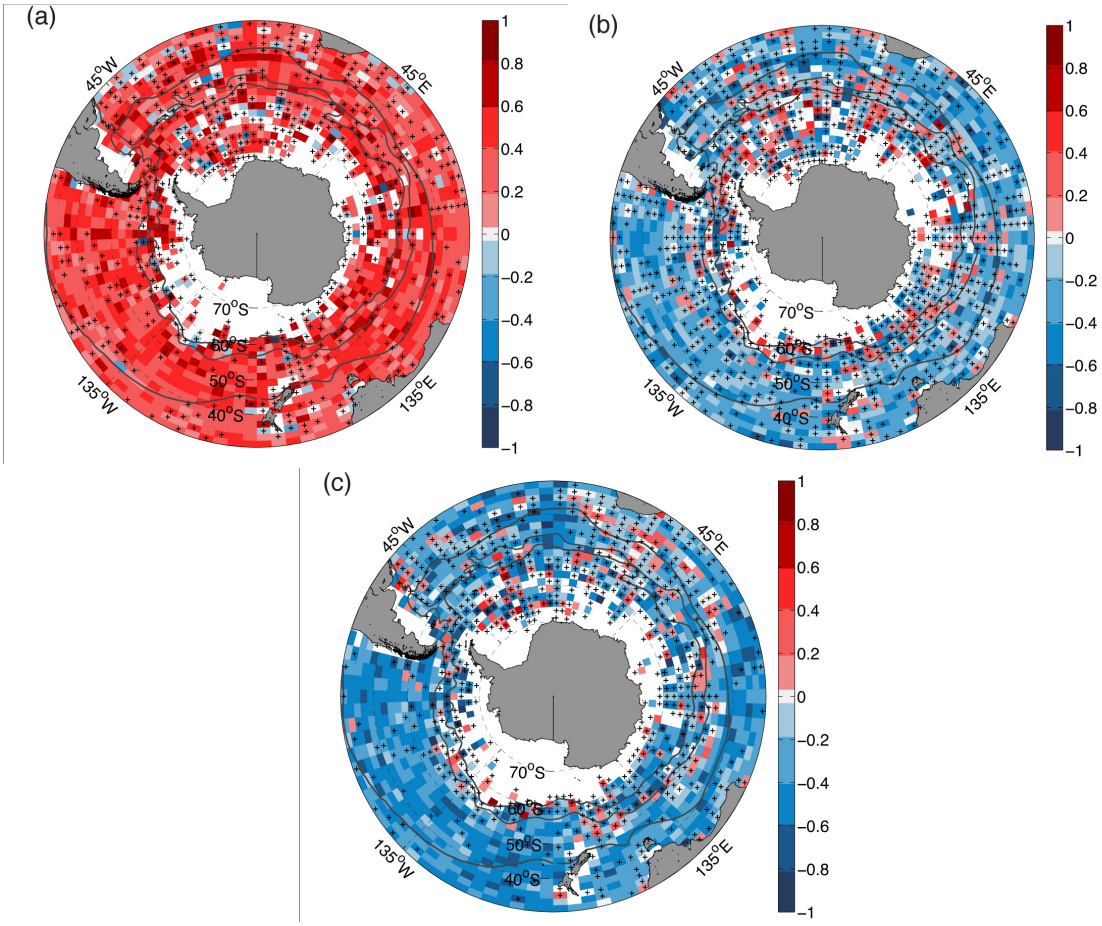

Figure 2.6: Local summer (DJF) correlation coefficients between daily anomalies of (a) wind speed and MLD, (b) Q_{net} and MLD, and (c) SST and MLD. Because MLD data is sparse, here we do not smooth out or filter the data in time. Cross-hatched areas indicate r is not significant at the 90% level. The mean positions of the STF, SAF and PF are shown in black contours.

between wind speed and Chl-a. However, our results indicate no correlation between wind speed and Chl-a at one-week time lags (not shown), even when we smooth spatially (with a spatial filter of 1×5 grid cells given the ACC moves at ~ 125 km week^{-1}) to account for advection, implying no clear connection with dust deposition. Further tests of lagged correlations between wind speed and Chl-a using daily data show that the correlation is significant at zero and one-day lags but mostly vanishes after two days. The time response of Chl-a to high winds is more consistent with nutrient supply due to wind-driven entrainment at the base of the mixed layer than with direct dust deposition. Although dust may not be immediately bioavailable, it is nevertheless presumably a source of Fe to the deep ocean (*Jickells*, 2005).

Although entrainment due to MLD deepening may play an important role in the open ocean, as suggested from correlations in Section 3.2., regions where the correlation between wind speed and Chl-a is not statistically significant (Figure 7a) may indicate that bioavailable Fe is supplied by means other than entrainment due to MLD deepening, or that the waters brought up lack bioavailable Fe (e.g. where waters have not recently interacted with the oceanic seafloor to pick up Fe and/or are distant from dust sources.)

Surface cooling might be predicted to deepen the MLD (Fig. 2.6b) and increase Chl-a. Significant negative correlations between anomalies of Q_{net} and Chl-a indicate surface cooling has an impact on Chl-a to the north of the STF (Fig. 2.7b), potentially through MLD deepening. However, low and mostly non-significant correlations in Figure 2.7b demonstrate this is not a dominant mechanism that drives Chl-a variability in the summer over most of the ACC. This result underscores the importance of wind-induced entrainment in sustaining summer phytoplankton blooms.

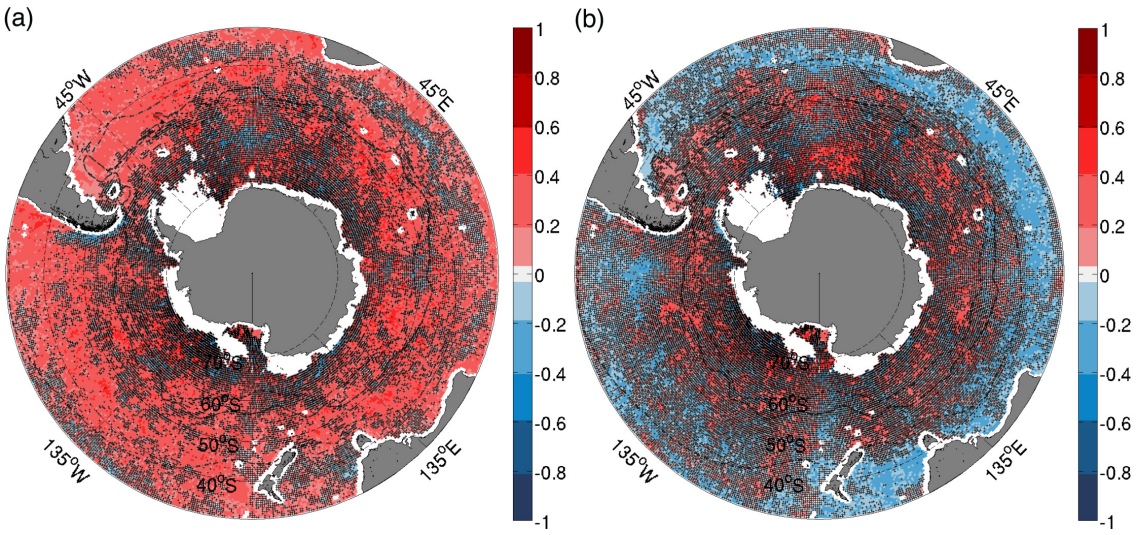

Figure 2.7: Local summer (DJF) correlation coefficients between high-pass filtered daily anomalies of (a) Chl-a and wind speed and (b) Chl-a and Q_{net}, considering spatial scales larger than 350 km and timescales of less than 10 days that highlight the effect of atmospheric storms. Dotted areas indicate the correlation is not significant to the 90% level. The mean positions of the STF, SAF and PF are shown in black contours.

2.3.4 Effect of Ekman pumping on Chl-a

In addition to deepening the MLD, the wind can also drive Ekman-induced upwelling associated with the wind-stress curl. The mean curl of the wind stress is expected to be positive in the subtropical band up to the latitude where the westerlies reach their maximum ($\sim 50^o$ S, white dotted line in Figure 2.8), and negative towards the south up to the maximum in the polar easterlies. In the Southern Hemisphere, the mean wind-stress curl translates into upwelling over most of the ACC (red in Figure 2.8a). Mean summer upwelling velocities w_{Ek} range from 0.2 to 1 m week^{-1} (Fig. 2.8a). Variability is largest over the ACC and over continental shelves (with the exception of the Patagonian shelf off South America, Fig. 2.8b), where maximum w_{Ek}'s are also largest (>1 m week^{-1}, not shown). Summer w_{Ek} can reach 0.8 m day^{-1} or roughly 6 m week^{-1}, which is in the range of values observed in the open ocean

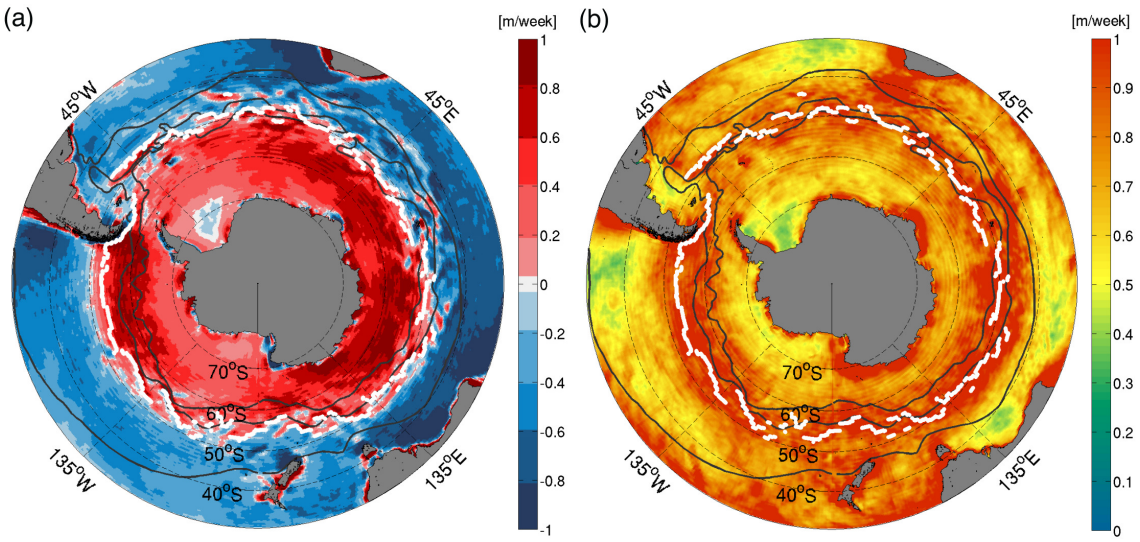

Figure 2.8: (a) Mean summer (DJF) Ekman pumping velocities (w_{Ek}) in m week^{-1}, based on weekly data for the period 2000-2011. (b) Standard deviation of summer w_{Ek}. The white dotted line indicates the mean position of maximum westerlies. The mean positions of the STF, SAF and PF are shown in black contours.

(e.g. *Fiechter and Moore*, 2009). The island effect due to the orographic obstruction of winds shows as a dipole in w_{Ek} over major islands, e.g. in Tasmania, New Zealand, South Georgia and Kerguelen, with upwelling to the north and downwelling to the south.

Surface wind direction and the wind-stress curl can be significantly modified over midlatitude SST fronts, and this in turn can influence ocean Ekman pumping at eddy scales (*O'Neill and Chelton*, 2003, 2010). Here we are interested in the large-scale Ekman pumping effect associated with atmospheric storms, and therefore we retain large spatial scales and short timescales ($>$ 350 km $\times$ 350 km and $<$ 10 days, see Section 2.4) when computing correlations with w_{Ek} (Fig. 2.9).

Ekman upwelling brings cold SSTs to the surface over a circumpolar band (blue areas in Figure 9a). The SST response to Ekman-induced upwelling is not restricted to the south of the mean maximum westerlies but is instead shifted northward

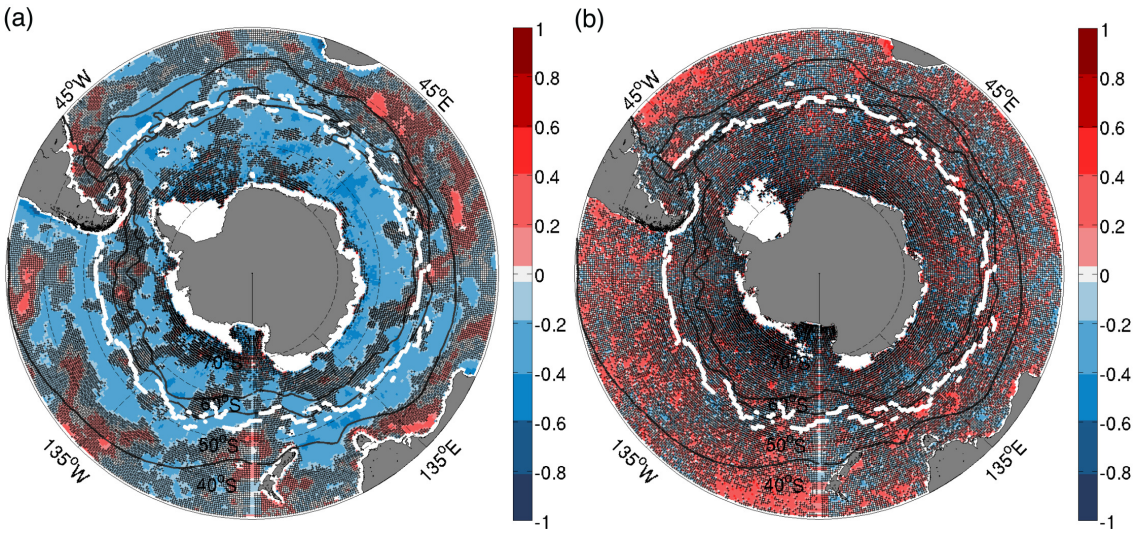

Figure 2.9: Summer (DJF) partial correlation coefficients, controlling for Q_{net}, between weekly anomalies of (a) w_{Ek} and SST, and (b) w_{Ek} and Chl-a, considering spatial scales larger than 350 km $\times$ 350 km and timescales of less than 10 days that highlight the effect of atmospheric storms. Dotted areas indicate that the correlation is not significant to the 90% level. The white dotted line indicates the mean position of maximum westerlies. The mean positions of the STF, SAF and PF are shown in black contours.

presumably due to oscillations in the position of the maximum westerlies. However, the correlation between w_{Ek} and Chl-a in Figure 9b is mostly non-significant and does not mirror the w_{Ek} versus SST correlations in Figure 9a. Ekman upwelling does appear to enhance summer Chl-a in coastal upwelling systems of the oceans' eastern boundaries and to the north of the STF in the western Pacific and Atlantic (Figure 9b). On the whole, Ekman upwelling has less impact on summer Chl-a than wind speed, and its impact is localized.

2.3.5 SST and Chl-a

Changes in SST provide another index of variability in the upper ocean that can impact phytoplankton (*Behrenfeld et al.*, 2006, 2008; *O'Malley et al.*, 2010). In this section, we look separately at the influence of SST on Chl-a, because it shows

complex patterns that cannot be solely attributed to shoaling or deepening of the MLD at synoptic scales and are likely influenced by mesoscale processes.

Because SST responds to atmospheric forcing as well as a whole range of upper ocean processes, SST anomalies can only partially indicate subsurface entrainment and changes in MLD (see Section 3.2). In Figure 2.10a, by computing partial correlations while controlling for Q_{net} we are able to interpret SST anomalies more clearly as a signature of an oceanic process. Horizontal processes, however, can obscure the correlation patterns resulting from vertical entrainment, and this is more pronounced at weekly timescales. Although the patterns in Figure 2.10a remain largely unchanged when using spatially smoothed fields that suppress the effect of advection by the mean currents or oceanic mesoscale features, horizontal (and nonlinear) processes may remain in the time domain at weekly timescales, because these act over longer timescales (i.e. weeks to months).

Summer Chl-a anomalies over the Southern Ocean are strongly correlated with SST anomalies, showing large and statistically significant positive or negative correlations over coherent areas at weekly timescales (Fig. 2.10a). Although the SST may have a direct impact on phytoplankton growth by enhancing metabolic rates (*Eppley*, 1972; *Neori and Holm-Hansen*, 1982; *Reay et al.*, 2001), in Figure 2.10a correlation patterns are tightly linked to frontal features, suggesting oceanic circulation and stratification as main drivers of these correlations, again revealing the close connection between phytoplankton and their physical environment (*O'Malley et al.*, 2010).

Regions where Chl-a and SST are inversely related are potential regions where entrainment or upwelling may be at work (e.g. to the north of the STF, to the

north of the PF in the eastern Pacific, and between the SAF and PF to the south of Africa). Negative correlations (-0.2 to -0.9) observed mostly to the north of the STF in Figure 2.10 are consistent with enhanced Chl-a driven by entrainment of cold and presumably nutrient-rich waters from below the euphotic zone due to enhanced wind mixing (Fig. 2.7a) and surface cooling (Fig. 2.7b), rather than Ekman upwelling (Fig. 2.9a).

When only variability of less than 10 days is considered, SST and Chl-a are uniformly negatively correlated (Fig. 2.10b) and consistent with the entrainment hypothesis. Figure 2.10b uses high-pass filtered daily anomalies to emphasize the fraction of variance that can be attributed to MLD deepening at the scales of atmospheric storms. Remarkably, positive correlations in Figure 2.10a vanish and become non-significant in Figure 2.10b. Positive correlations (0.2 to 0.9) in Figure 2.10a are observed over most of the Sub-Antarctic Zone (SAZ, the region between the STF and SAF), to the south of the PF in localized regions (e.g. downstream of South Georgia and South Sandwich Islands, and Kerguelen Plateau, or in the central Pacific), and west of the Antarctic Peninsula. Although positive correlations in Figure 2.10a may imply a shoaling of the MLD and light-limiting conditions, they vanish when considering synoptic timescales (Fig. 2.10b) and are, therefore, likely influenced by oceanic mesoscale processes that operate over longer timescales.

2.3.6 Discussion

We showed evidence of MLD deepening due to strong winds in the summer over subtropical regions, and most surprisingly, over the ACC where mixed layers are deepest. The mechanisms by which winds deepen the mixed layer are beyond

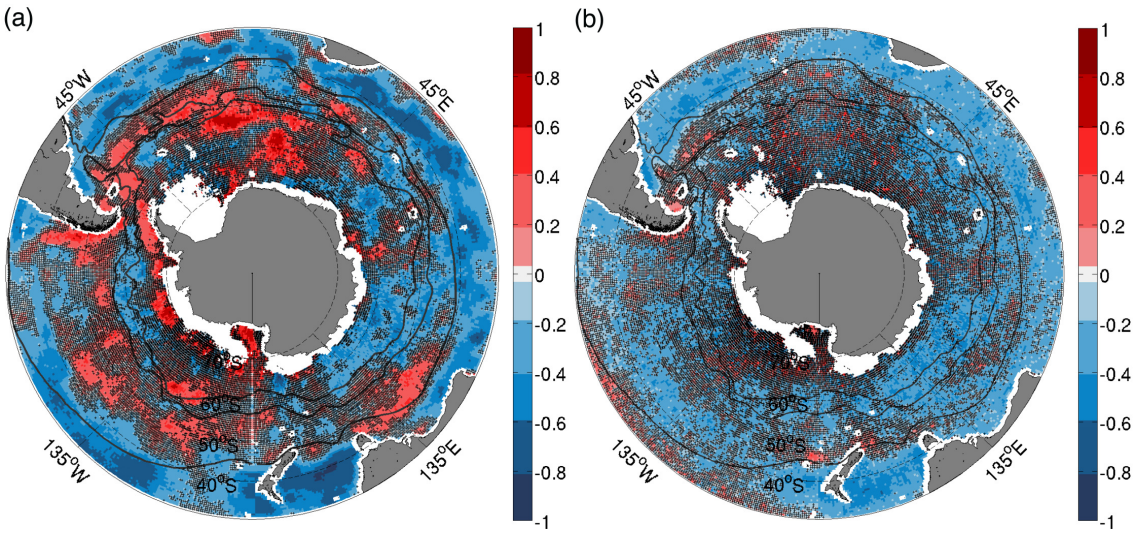

Figure 2.10: Partial correlation coefficients between (a) weekly anomalies of Chl-a and SST, and (b) high-pass filtered daily anomalies of Chl-a and SST, controlling for the effect of Q_{net}, and considering spatial scales larger than 350 km $\times$ 350 km. Dotted areas indicate the correlation is not significant to the 90% level. The mean positions of the STF, SAF and PF are shown in black contours.

the scope of this work, but could include effects of Langmuir circulation (*Kukulka et al.*, 2009; *Smith*, 1998; *Li and Garrett*, 1997; *Li et al.*, 1995) that is expected to have a significant effect in the Southern Ocean where winds are persistent and the Stokes drift is large (*Belcher et al.*, 2012), and/or shear-induced turbulence (*Klein and Coste*, 1984). Wind gustiness at synoptic time scales can also have an impact on the MLD through wave-induced mixing processes that can potentially facilitate mixing across the base of the seasonal mixed-layer (*Babanin et al.*, 2009); however, we find no correlation between wind gustiness and Chl-a (not shown). Wind-induced mixing can input nutrients into the euphotic zone and thus may drive the positive correlations we observe between winds and Chl-a over most of the Southern Ocean (Fig. 2.7a).

The influence of wind-driven entrainment on Chl-a is associated with atmo-

spheric synoptic storms. This is suggested by correlations based on filtered anomalies that highlight the variability on the scales of the storms (i.e. timescales of < 10 days and spatial scales > 350 km, in Figure 2.7). The combined analysis of correlation patterns based on significant partial correlations of filtered data, controlling for Q_{net}, is summarized in Figure 2.11. To construct Figure 2.11 we first plot in light blue regions where blooms are associated with high winds (i.e. red in Figure 2.7a). Overlaid in green we plot regions where blooms are associated with cold SSTs (i.e. blue in Figure 2.10b), and overlapped regions where both high winds and cold SSTs enhance blooms are indicated in blue. Finally, overlaid in yellow we plot regions where blooms are associated with warm SSTs (red in Figure 2.10b). Therefore, Figure 2.11 can be interpreted as follows: blue regions indicate blooms that are potentially associated with wind-driven entrainment, regions in light blue are those where blooms are associated with high winds that are not necessarily accompanied by changes in the SST, green regions are those where blooms are associated with cold SSTs presumably caused by processes unrelated to high winds, and in yellow regions blooms are associated with warm SSTs that may respond to a shoaling of the MLD, suggesting a light-limited environment.

On shelves, blooms may respond differently to winds than they do in the open ocean. In more quiescent shelf waters under the influence of fresh water input, thin mixed layers can develop (~ 5 m), and large phytoplankton biomass may result in self-shading leading to more complex interactions between light levels, mixing depth and nutrient supply (*Vernet et al.*, 2008). For instance, stratification of shelf waters off the southern tip of South America and in the Marginal Ice Zone (MIZ) that surrounds the Antarctic continent is strongly influenced by fresh water fluxes from

glacial origins and sea-ice melting, which stratify the upper ocean but also have the potential to release Fe to surface waters. Blooms in the MIZ have been associated with low winds (*Fitch and Moore*, 2007) and the retreat of the ice shelves and sea ice melting (e.g. *Arrigo et al.*, 1998; *Vernet et al.*, 2008).

High winds leading to high Chl-a through entrainment of nutrients presumes a biomass increase due to enhanced growth rates. However, phytoplankton biomass accumulation reflected in Chl-a also depends on loss rates that can be caused by grazing. *Behrenfeld*'s (2010) Dilution-Recoupling Hypothesis provides an alternate mechanism to explain the links between the deepening of the mixed-layer and increases in Chl-a. In this view, net phytoplankton growth results from a delicate balance between phytoplankton specific growth rates and grazing. Physical processes such as vertical mixing can also modulate grazing rates and alter the balance by dilution: as the MLD deepens, phytoplankton-free waters are entrained into the mixed layer, lowering both prey-predator encounter rates and grazing pressure on phytoplankton (*Marra and Barber*, 2005; *Behrenfeld*, 2010). The dilution process presumes no subsurface Chl-a maximum, and therefore requires that the MLD exceed the euphotic depth which is more likely to be the case in ACC waters than in subtropical waters.

To our knowledge, the direct relationship between SST and Chl-a in the SAZ in Figure 2.10a has not been previously documented from satellite measurements. The positive correlations between SST and Chl-a that we observe in the SAZ might suggest that a warm shallow mixed layer promotes high Chl-a, which would imply that relatively deep summer MLDs in the SAZ lead to light-limitation. However, such shoaling of the MLD cannot be attributed to reduced wind-mixing or surface warming at synoptic timescales. High-pass filtered data in the time domain (Fig. 2.10b) suggest

mesoscale processes cannot be ruled out in Figure 2.10a and may also be responsible for positive correlations between Chl-a and SST.

Mesoscale eddies and fronts that are ubiquitous in the Southern Ocean can modify upper ocean stratification and SST. Particularly during times of weak air-sea fluxes or in the presence of strong horizontal gradients, horizontal dynamics can play a leading order role in restratifying the mixed layer (*Lapeyre et al.*, 2006; *Fox-Kemper et al.*, 2008). Close to frontal regions the stratification of the surface mixed layer is set by the competing effects of ageostrophic circulation, baroclinic instabilities and eddies, which tend to restratify the upper ocean, and turbulent mixing (i.e. driven by winds and buoyancy forcing) which destroys stratification (*Lapeyre et al.*, 2006; *Taylor and Ferrari*, 2011b). Numerical simulations and observations show that restratification at fronts inhibits vertical mixing, and can trigger phytoplankton blooms in low-light conditions, even in the presence of strong surface cooling and destabilizing winds (*Taylor and Ferrari*, 2011b; *D'Asaro et al.*, 2011).

In the SAZ, the positive correlations between SST and Chl-a suggest that weak background stratification may precondition waters to permit formation of deep mixed layers, and intense mesoscale dynamics assist in the restratification of the surface layer triggering phytoplankton blooms. This scenario is in agreement with the findings of *Llido et al.* (2005) in the SAZ south of Africa, who found a strong influence of MLD shoaling on bloom occurrence, either caused by cyclonic eddies or local Ekman pumping, that may in fact extend to many regions throughout the SAZ. Ekman-induced upwelling results in cold SSTs over the SAZ (blue in Figure 2.9a) but appears to have little impact on Chl-a (red in Figure 2.9b) at storm's scales. Anticyclonic eddies, however, generally associated with warm SST anomalies, are in agreement with

the joint variability between SST and Chl-a that we observe in the SAZ. Enhanced Chl-a in warm core eddies has been observed (e.g *Mizobata et al.*, 2002; *Waite et al.*, 2007; *McGillicuddy et al.*, 2007; *Kim et al.*, 2011; *Lehahn et al.*, 2011), and non-linear mechanisms for nutrient supply and Chl-a enhancement within anticyclonic eddies have been proposed (*Martin and Richards*, 2001; *Mahadevan et al.*, 2008), as well as the advection of warm high-chlorophyll waters by anticyclones (*Lehahn et al.*, 2011).

Another plausible physical explanation for positive correlations between SST and Chl-a is linked to the meandering and eastward advection of waters in the ACC (*Meskhidze et al.*, 2007). Upwelling and downwelling motions were observed in the meandering of the PF (*Strass et al.*, 2002). An ocean-plankton model suggests that due to the fast surface currents of the ACC, enhanced Chl-a can occasionally occur in downwelling areas, and low Chl-a can occur in upwelling areas (*Hense et al.*, 2003). This is because newly upwelled water near the surface has low Chl-a, but it is rich in nutrients and therefore can sustain phytoplankton growth while it is advected, and until a downwelling event occurs.

Wind-driven Ekman currents are another factor that can supply nutrients and restratify or destratify the mixed layer in cases when the wind stress has a component directed along the front (*Thomas and Ferrari*, 2008; *D'Asaro et al.*, 2011). When the wind is oriented down front, as is most likely the case over the ACC fronts, northward Ekman transport carries waters from the cold side of the front to the warm side which tends to destabilize the water column to the north, driving convective mixing and a reduction of stratification. In the SAZ, one suggestion is that micronutrients are supplied by northward Ekman transport of nutrient-rich waters from the Polar Frontal Zone (PFZ, the region between the PF and SAF, e.g. *Pollard et al.*, 2002).

Such Ekman transport would carry cold SSTs from the south. Therefore, under the assumption that nutrients limit summertime growth, upwelling or mixing and the horizontal advection of nutrients from the south would all imply negative correlations between Chl-a and SST, but we showed this is not the case in the SAZ (see red in Figure 2.10a). In the PFZ, however, the negative correlations between SST and Chl-a (Figure 2.10a) could be consistent with a destabilizing effect of Ekman advection. This perhaps suggests a preconditioning of stratification imposed by frontal dynamics and nutrient-limited conditions to the north of the PF that is alleviated during periods of Ekman advection of cold and nutrient-rich waters from the south.

2.4 Summary and Conclusions

In this study we have explored the influence of the atmospheric forcing on upper ocean processes (i.e. MLD deepening and Ekman-induced upwelling) that can influence summer Chl-a variability in the Southern Ocean. Recognizing the limitations of a correlation analysis, which does not allow for the determination of causality, we analyze correlation patterns between Chl-a and physical variables, focusing mainly on the potential of nutrient entrainment through the base of the seasonal mixed layer, although other possible mechanisms have also been discussed.

On daily to weekly timescales, summer Chl-a is more influenced by wind-induced entrainment through MLD deepening than by Ekman-induced upwelling. The wind-stress curl, which drives Ekman pumping, showed weak correlations with Chl-a. Ekman pumping, subject to horizontal convergences and divergences, may be more influential on longer timescales (*de Szoeke*, 1980; *Fiechter and Moore*, 2009), and/or on regional and eddy scales.

Wind speed and Chl-a show significant correlations over large areas in the Southern Ocean, confirming that strong winds measurably influence phytoplankton blooms (*Kahru et al.*, 2010). However, in contrast with *Kahru et al.* (2010) who used year-round data, we find strong winds enhance Chl-a in the summer suggesting wind-driven entrainment helps sustain phytoplankton blooms.

The impact of wind-driven entrainment on Chl-a is broader on daily timescales, and it is associated with atmospheric synoptic storm scales. More surprisingly, positive correlations between wind speed and Chl-a are found even over regions with deep summer mixed layers, suggesting that anomalous winds have the potential to deepen the mixed layer, entraining subsurface waters into the euphotic zone effectively without completely eroding the seasonal mixed layer. Using rates of change of MLD from Argo floats, *Tagliabue et al.* (2014) find negligible Fe entrainment fluxes from transient MLD deepening. Our results based on high resolution satellite data suggest transient MLD deepening may entrain additional Fe on shorter timescales than those resolved by Argo floats (i.e. 10 days at most).

With our approach and the available data, however, we cannot address whether the influence of winds on surface Chl-a is through entrainment of nutrients impacting phytoplankton growth rates, entrainment of phytoplankton-rich waters from a subsurface Chl-a maximum or reduced grazing pressure on phytoplankton. The underlying process can have profound implications on the biological pump, and the acquisition of subsurface Chl-a and nutrient data in the Southern Ocean would be beneficial to help shed light on these. A better understanding of Southern Ocean biology and biogeochemistry is essential regarding projections for the Southern Ocean carbon sink.

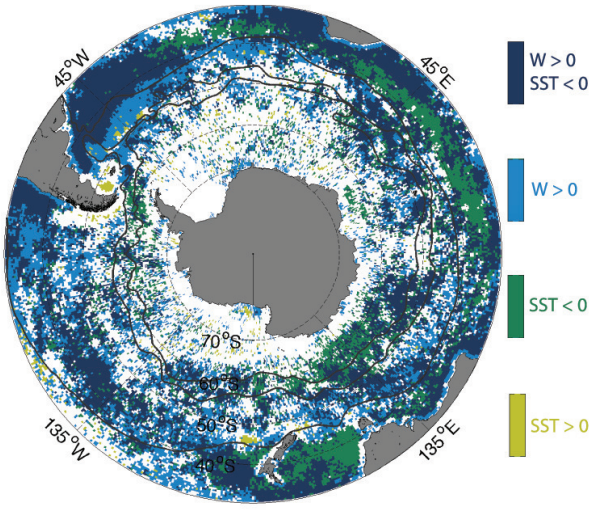

Figure 2.11: Summary figure showing pixels were positive anomalies of Chl-a are associated with positive anomalies in wind speed (light blue), negative anomalies in SST (dark green), both positive anomalies in wind speed and negative anomalies in SST (blue), and positive anomalies in SST (light green). Regions in blue are consistent with enhanced Chl-a associated with wind-driven entrainment of cold and presumably nutrient-rich waters at synoptic timescales. This map was constructed based on significant partial correlations of spatially smoothed and high-pass filtered data in the time domain (i.e. spatial scales $>$ 350 km and timescales $<$ 10 days), controlling for Q_{net}.

As a response to global warming and ozone depletion, Southern Hemisphere westerlies have intensified and shifted southward predominantly in the summer (*Thompson et al.*, 2011). This study suggests that phytoplankton biomass could increase in response to higher summer winds, with potential atmospheric CO_2 drawdown and subsequent enhancement of the biological pump (*Marinov et al.*, 2008), counteracting the outgassing of carbon through enhanced upwelling of deep waters that are rich in dissolved inorganic carbon (*Russell et al.*, 2006). Moreover, given that stratification is expected to increase in a changing climate (e.g. *Capotondi et al.*, 2012), the importance of wind-driven entrainment might increase more than linearly in the future.

2.5 Acknowledgments

We thank the data processing workgroups from JPL, GlobColour, RSS, NCEP and the Argo program for providing the data, and James Holte for the MLD estimates from Argo. Microwave OI SST data are produced by Remote Sensing Systems and sponsored by National Oceanographic Partnership Program (NOPP), the NASA Earth Science Physical Oceanography Program, and the NASA MEaSUREs DISCOVER Project. Data are available at www.remss.com. NASAs Research, Education and Applications Solution Network (REASoN) and MEaSURES programs funded development of the CCMP wind fields, which are distributed by the Physical Oceanography Distributed Active Archive Center (http://podaac.jpl.nasa.gov/). Chl-a data are processed and distributed by ACRI-ST GlobColour service (http://hermes.acri.fr), supported by EU FP7 MyOcean ESA GlobColour Projects, using ESA ENVISAT MERIS data, NASA MODIS and SeaWiFS data. Heat fluxes from the CFSR reanalysis are available at http://rda.ucar.edu. The Research Data Archive is managed by the Data Support Section of the Computational and Information Systems Laboratory at the National Center for Atmospheric Research in Boulder, Colorado. This work was funded by a NASA NESFF fellowship (NNX12AN41H 001), the NASA Physical Oceanography Program (NNX08AI82G), and NSF grants (ARRA OCE0850350 and ANT-0948338). This work was supported by NSFs Southern Ocean Carbon and Climate Observations and Modeling (SOCCOM) project under the NSF Award PLR-1425989. We thank Lynne Talley, Peter Franks, the reviewers for a careful reading and suggestions to improve this manuscript, and Alberto Piola and Rob Pinkel for useful discussions.

Chapter 2, in full, is a reprint of the material as it appears in *Journal of*

Geophysical Research Oceans: **Carranza M. M.** and Gille S. T. (2015). Southern Ocean wind-driven entrainment enhances satellite chlorophyll-a through the summer, *J. Geophys. Res. Oceans*, 120, doi:10.1002/ 2014JC010203. The dissertation author was the primary investigator and author on this paper.

Chapter 3

Frequent chlorophyll-a fluorescence maxima and unevenness within Southern Ocean hydrographic mixed layers

The mixed-layer depth (MLD), the homogeneous layer in hydrographic properties, is fundamentally different from the mixing layer depth: tracers that are homogenized within a mixing layer are not necessarily homogenized within a mixed layer defined by hydrographic properties. Here, we exploit continuous vertical profiles of Chl-a fluorescence from biogeochemical Argo floats and elephant seal tags in the Southern Ocean to assess Chl-a fluorescence vertical structure within hydrographically defined mixed layers. We identify profiles with deep Chl-a fluorescence maxima (DFM) by fitting the profiles to functional forms (i.e. Gaussians, sigmoids, exponentials and their combinations). More than 30% of nighttime profiles are identified as

having DFM. The depth of the DFM is compared to the MLD, as determined based on several commonly used definitions. We find that a significant fraction of DFM are found within the MLD (20-80%, depending on MLD definition), suggesting that assuming Chl-a fluorescence to be throughly mixed within a hydrographically defined mixed layer is a weak assumption that could prove to be wrong.

3.1 Introduction

The turbulent boundary layer, the layer of the ocean in direct contact with atmospheric forcing that is actively mixing, can be fundamentally different from the mixed layer, the weakly stratified remnant layer of a past turbulent event (e.g. *Brainerd and Gregg*, 1995). Phytoplankton and biogeochemical tracers are not necessarily thoroughly mixed in a mixed layer that is homogeneous in density (hereafter, a hydrographic mixed layer), and their distributions within the mixed layer will depend on the level of turbulence. The tradeoff between the timescale that it takes a gradient of a property to form and the timescale that it takes mixing to destroy it determines whether the property is homogeneous or gradients can exist in a hydrographic mixed layer (e.g. *Franks*, 2014). Theoretical and numerical studies have shown that the ratio between timescales of biological and turbulent processes determines the spatial distribution of plankton and will affect their spatial heterogeneity relative to passive tracers (*Abraham*, 1998; *Mahadevan and Campbell*, 2002; *Tzella and Haynes*, 2007).

Light decreases exponentially with depth, and turbulence stirs phytoplankton, exposing them to fluctuations in ambient light (*Lewis et al.*, 1984a). To optimize their photosynthetic capacity and/or prevent damage from high light intensity, phytoplankton respond physiologically to changes in ambient light (on timescales of seconds

to a few days, (e.g. *Denman*, 1983; *Post et al.*, 1984; *Claustre et al.*, 1994; *Griffith et al.*, 2010)). The history of their exposure to light will also impact growth rates (e.g. *Marra*, 1978; *Denman*, 1983). The vertical distribution of photo-adaptive properties (e.g. Chl-a fluorescence) results from the interaction between photo-adaptation (the biological adjustment of plankton to light intensity, including non-photochemical quenching) and vertical mixing by turbulent processes (e.g. *Cullen and Lewis*, 1988; *MacIntyre*, 2008). Thus, the distribution of physiological properties can be related to vertical displacement of phytoplankton in the water column and mixing rates (*Falkowski*, 1983). Vertical gradients in Chl-a fluorescence may exist in a hydrogaphically mixed layer if the timescale of photo-adaptation is shorter than that of turbulent processes in the mixed layer. In contrast, uniform Chl-a fluorescence will prevail if turbulent processes are fast enough that mixing occurs with a timescale shorter than that of photo-adaptation.

Many theoretical studies have related mixing rates with the distribution of photo-adaptive properties (e.g. *Lewis et al.*, 1984a; *Dusenberry*, 2000) and have postulated the level of turbulence in the mixed layer may allow for gradients in phytoplankton growth and/or accumulation at any given depth within a mixed layer (e.g. *Huisman et al.*, 1999; *Taylor and Ferrari*, 2011a), but few have shown Chl-a fluorescence and/or phytoplankton accumulation within a mixed layer from *in situ* observations (*Ryther and Hulburt*, 1960; *Falkowski*, 1983; *Therriault et al.*, 1990; *Chiswell*, 2011). In this paper we exploit continuous vertical profiles of Chl-a fluorescence from novel *in situ* sensors that are being deployed in the Southern Ocean (*Guinet et al.*, 2013; *Russell et al.*, 2014) to demonstrate that Chl-a fluorescence gradients can exist within a hydrographic mixed layer and/or in remnant mixed layers more often than

commonly thought.

The Southern Ocean contains mode water formation regions that are characterized by deep winter mixed layers (e.g. *Sallée et al.*, 2006; *Dong et al.*, 2008; *Holte et al.*, 2012), and it is subject to strong synoptic scale atmospheric forcing year round (e.g. *Vera*, 2003). Deep winter mixed layers result in thick remnant mixed layers (typified by weakly stratified layers below the summer mixed layer containing winter mixed layer water that is left behind after the deep mixed layers restratify in spring and summer (see e.g. *Cole et al.*, 2010)). Storm events in summer can also lead to thinner weakly stratified remnant mixed layers below an actively mixing summer mixed layer (*Talley et al.*, 2011). The existence of weakly stratified layers within the seasonal mixed layer can have consequences for vertical distributions of phytoplankton and/or photo-adaptive properties due to the varying levels of turbulence (*Huisman et al.*, 1999; *Taylor and Ferrari*, 2011a). Turbulence levels will vary due to the competing effects of different physical mechanisms that occur in the upper ocean (e.g., convective, wind-driven, wave-driven turbulence or Langmuir circulations, *Franks*, 2014). For example, turbulence levels near the surface are largely influenced by atmospheric forcing (i.e. buoyancy fluxes and winds, e.g. *Taylor and Ferrari* (2011a); *Chiswell* (2011)), whereas turbulence at the base of the mixed layer can be generated by shear instabilities and internal wave breaking. Mesoscale eddies and fronts, which are ubiquitous features in the Southern Ocean, also provide regions with varying levels of turbulence and convergences in the flow, that may lead to plankton accumulation near fronts (e.g. *Franks and Walstad*, 1997b; *Hopkinson et al.*, 2007; *Taylor et al.*, 2012; *Powell and Ohman*, 2015). Stratification of phytoplankton (i.e. gradients within mixed layers) is thus likely to occur in deep remnant mixed

layers, where turbulence may be reduced relative to a more actively mixing surface layer, in shallow weakly stratified mixed layers that develop in the spring (*Chiswell*, 2011), as well as near fronts.

We hypothesize that intermittent atmospheric forcing from synoptic storms (with fluctuations between 2-10 days) may allow for periods of quiescence and reduced levels of turbulence in hydrographically defined mixed layers, allowing for the existence of Chl-a fluorescence gradients or subsurface maxima within a well-mixed hydrographic mixed layer. In other words, in between storms, reduced levels of turbulence within hydrographic mixed layers may allow phytoplankton inhomogeneities, and their distribution within the mixed layer will depend on the varying levels of turbulence (*Franks*, 2014).

Bio-optical *in situ* sensors from profiling floats and elephant seal tags that carry new bio-logging devices are populating the Southern Ocean, providing unprecedented estimates of Chl-a fluorescence that allow assessment of the vertical structure of Chl-a fluorescence in all seasons and under sea ice (Fig. 3.1a). Time series plots of Chl-a fluorescence profiles from these (Fig. 3.1b and c) reveal two consistent patterns: Chl-a is enhanced within the mixed layer throughout the seasons (unlike in the North Atlantic, where wintertime Chl-a frequently drops to background levels in deep waters), and significant Chl-a variance within the mixed layer suggests the existence of Chl-a fluorescence vertical gradients and deep Chl-a fluorescence maxima within hydrographically defined mixed layers.

In this study, we exploit these new measurements from floats and Southern elephant seals to assess the vertical structure of Chl-a fluorescence within the mixed layer and the seasonality in the occurrence of subsurface maxima. We provide a

statistical description of the observed patterns in the Southern Ocean as a whole, but regional differences may be expected within the Southern Ocean (*IOCCG*, 2015). We present the datasets used (Section 3.2), and some of their limitations (Section 3.3). By fitting fluorescence profiles to typical functional forms we identify profiles that show prominent subsurface maxima (Section 3.3). We identify the mixed-layer depth (MLD) using several definitions based on density criteria. Results are presented in Section 3.4, where we compare the depth of deep fluorescence maximum (DFMD) with the MLD, for all MLD definitions used, quantify the number of profiles with DFM that lie above the MLD for each month of the year, and present metrics of Chl-a fluorescence variability in the mixed layer.

3.2 Data

We exploit Conductivity-Temperature-Density (CTD) and Chl-a fluorescence vertical profiles from novel in-situ sensors that provide year-round measurements in the open Southern Ocean, as well as under sea ice.

3.2.1 Southern-elephant Seal Tags

Southern elephant seals with oceanographic sensors provide measurements in regions that are rarely observed with traditional oceanographic platforms, and unlike most floats are capable of sampling under ice. Elephant seals equipped with conductivity-temperature-depth satellite-relayed data loggers (CTD SRDLs) at sub-Antarctic islands have substantially increased the number of observations during winter and in the sea-ice zone (e.g. *Charrassin et al.*, 2008; *Roquet et al.*, 2013; *Fedak*, 2012). The CTD profiles from these sensors have accuracies close to those from Argo

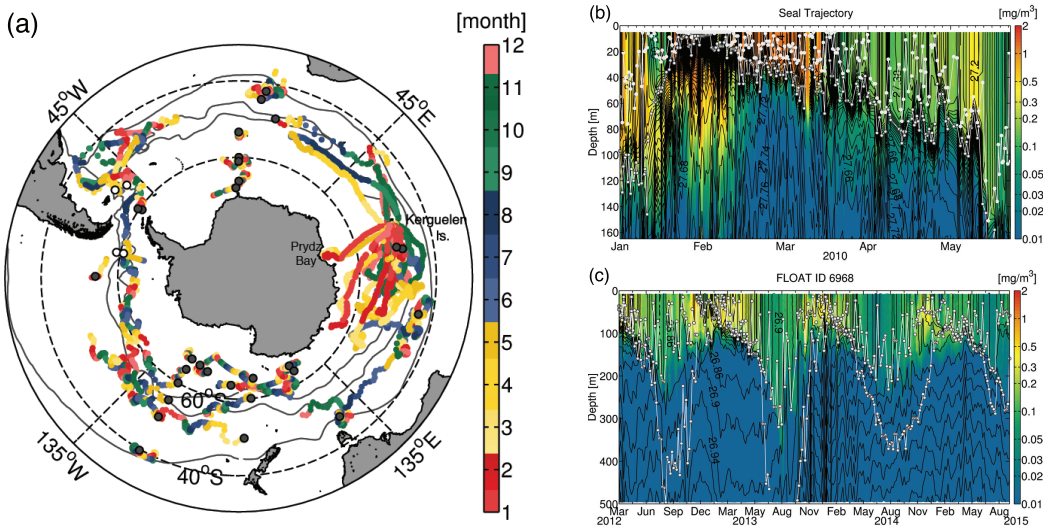

Figure 3.1: (a) Locations of Chl-a profiles from elephant seal tags deployed off Kerguelen Is., EM-APEX (white dots) and Argo floats (black dots) with bio-optical sensors, color coded by month of the year when data were collected. The mean positions of the Subtropical Front (STF), Sub-Antarctic Front (SAF) and Polar Front (PF) from *Orsi et al.* (1995) are shown in black contours for reference. Chl-a as a function of time and depth, with density contours overlaid (in black), MLD estimates using the density threshold criterion of 0.005 and 0.125 kg m^{-3} (white lines) for (b) an elephant seal summertime through fall round-trip from Kerguelen Is. to Antarctica and (c) an Argo float deployed in the south Pacific sector of the Southern Ocean (FloatViz ID 6968).

profiling floats (*Roquet et al.*, 2011; *Fedak*, 2012). CTD-SRDL tags deployed in the Kerguelen Islands (see Fig. 3.1a) for the first time included a compact fluorometer (Cyclops-7 from Turner Designs) from which Chl-a fluorescence profiles can be derived (*Guinet et al.*, 2013). These new bio-logging devices were deployed on 27 elephant seals between December 2007 and February 2011, and calibrated Chl-a fluorescence profiles were made available by *Guinet et al.* (2013). Calibration procedures included pre-deployment tests against HPLC analysis of filtered samples and post-deployment inter-calibration of the different fluorometers. Elephant seals in their long foraging trips dive continuously to depths up to 2000 m during day and night, about 60 times a day. Due to power supply and Advanced Research and Global Observation Satellite (ARGOS) bandwidth limitations, 1-3 Chl-a fluorescence profiles per day were recorded in the top 180 m of ascent (with 2 s temporal resolution) and were averaged in 10 m bins from 5 m to 175 m (*Xing et al.*, 2012; *Jaud et al.*, 2012). The seals typically travel distances of 35-65 km per day, resulting in a spatial resolution along their track of about 25 km (*Charrassin et al.*, 2008), covering a vast sector of the Southern Indian Ocean (Fig. 3.1a) as they migrate to the Kerguelen Plateau, Antarctic waters, and the interfrontal zone between the Subtropical and Polar Fronts where they forage (*Dragon et al.*, 2010). To document the pre-breeding winter foraging trips, instruments were deployed in January and February at the end of the annual moult (*Charrassin et al.*, 2010). From a total of 3333 profiles, 1208 profiles were acquired in fall (March-April-May, MAM), 386 in winter (June-July-August, JJA), 605 in spring (September-October-November, SON) and 1134 in summer (December-January-February, DJF). Observations in austral spring are less frequent than in summer because this is the time of year when elephant seals breed and moult ashore

(*Fedak*, 2012).

3.2.2 Biogeochemical Floats

Compared with seals, biogeochemical floats provide higher vertical resolution (i.e. 2.5-10m, variable with depth) but coarser temporal sampling (i.e. ∼5-10 days, with a few exceptions). Some of the recently deployed Southern Ocean Carbon and Climate Observations and Modeling project (SOCCOM) floats have ice-avoidance capabilities that have allowed them to be deployed in regions that experience seasonal sea ice. Under sea ice or in rough sea state conditions floats do not acquire GPS position at the surface, and for the purposes of this study, we recovered the float position by linear interpolation of the latitude and longitude coordinates along the float trajectory. The bio-optical sensors on these floats measure Chl-a fluorescence (λ_{ex} = 470 nm, λ_{em} = 695 nm) and optical backscattering (λ= 700 nm) from which estimates of Chl-a fluorescence and particle concentration can be derived.

Data from bio-optical sensors on Argo floats are available from SOCCOM's website (http://soccom.princeton.edu). We use the set of 30 floats in the Southern Ocean (Fig. 3.1a, gray circles) equipped with an Environmental Characterization Optics Fluorometer-Scattering (ECO FLBB-AP2) sensor from WETLabs (last updated on May 5, 2016). These sampled 1189 Chl-a fluorescence profiles, along with temperature, conductivity (salinity) and pressure, typically recording 59 or 60 depth intervals during each profile in their ascent towards the surface every 5-7 days. They sample at higher rates as they approach the surface, resulting in a depth-dependent vertical resolution of 50 m from their parking depth of 1000 m up to 400 m, 10 m between 100-400 m and 5 m for the top 100 m.

Four Electromagnetic Autonomous Profiling Explorer (EM-APEX, *Sanford et al.* (2005)) floats that also carried ECO FLBB-AP2 sensors of identical characteristics as well as CTD's were deployed during Diapycnal and Isopycnal Mixing Experiment in the Southern Ocean (DIMES, *Ledwell et al.*, 2011) cruises (float IDs 4594, 4595, 4596, 4597), providing additional Chl-a fluorescence profiles over Drake Passage and the southwest Atlantic (Fig. 3.1a, white circles). These floats mostly recorded measurements every ∼2.5 m both during ascent and descent, at depths of up to ∼200 m (with some exceptions), and with variable sampling intervals during their missions (from 7-bursts a day to every 10 days). Due to the odd behavior of some of the floats, we only use profiles where pressure was either monotonically increasing or decreasing.

3.3 Methods

WETLabs' calibrations of Chl-a fluorescence rely on pure Chl-a or on phytoplankton monocultures that may not be representative of *in situ* phytoplankton communities (*Proctor and Roesler*, 2010). Species composition, relative pigment composition, cell size, nutrient status, growth phase, photoacclimation, and incident irradiance may uncouple the relationship between fluorescence and Chl-a (*Cullen*, 1982; *Mitchell and Kiefer*, 1988; *Proctor and Roesler*, 2010). Although Southern Ocean waters are not considered optically complex, different phytoplankton assemblages can contain varying amounts of other pigments (e.g., Chl-b and Chl-c) that can alter the bio-optical relationships (e.g. *Dierssen*, 2010). Moreover, Southern Ocean waters have considerable amounts of optically active substances such as colored-dissolved organic matter (CDOM, *Siegel*, 2002; *Del Castillo and Miller*, 2011) that may impact the retrieval of pigment fluorescence by absorbing the excitation energy. High-

Performance-Liquid-Cromatography (HPLC) analyses of water samples are desirable to further calibrate Chl-a fluorescence at each profile, but these measurements are not possible with autonomous platforms.

Some of the float data we use come from sensor test deployments, for which HPLC measurements from water samples are not available. Even if samples are collected at the deployment site (e.g. as is the case for SOCCOM floats), these are of limited utility for validating actual concentrations because floats may sample different regimes during the course of their mission (*Perry et al.*, 2008). There is an ongoing effort to calibrate Chl-a fluorescence using existing HPLC measurements in the Southern Ocean in combination with satellite Chl-a match-ups to provide best estimates of float Chl-a concentrations. WETLabs Chl-a concentrations from floats show biases of a factor of 2-7, with WETLabs Chl-a overestimating Chl-a concentrations from HPLC. Here, we use WETLabs' calibration values for Chl-a concentrations, but divide them by a factor of 2, because detailed assessments of Southern Ocean data suggest that the WETLabs values are biased high. Because of calibration uncertainties, in our analyses we subtract deep water (i.e., clearest water) values for each profile and show Chl-a fluorescence profiles in relative units. This allows us to assess vertical structure throughout the seasons and under sea-ice in a historically under-sampled region.

During daylight hours and especially near noon, Chl-a fluorescence is known to be decreased by non-photochemical quenching (i.e., the reduction of the fluorescence emission in surface waters due to ambient irradiance, NPQ) which may result in artificial deep Chl-a fluorescence maxima (*Jaud et al.*, 2012). Daytime fluorescence quenching is a recognized phenomenon in the Southern Ocean (*Holm-Hansen et al.*,

2000) and was detected throughout the elephants-seal and float datasets (*Sackmann et al.*, 2008; *Xing et al.*, 2012; *Biermann et al.*, 2015; *Boss and Haentjens*, 2016). Although these studies have proposed methods to correct for NPQ effects, those applicable with the available float data (with exception of the one proposed by *Biermann et al.* (2015)), rely on the assumption that fluorescence is well mixed in a hydrographically defined mixed layer (*Sackmann et al.*, 2008; *Xing et al.*, 2012). Because this assumption may prove to be wrong (and it is our working hypothesis), we use nighttime profiles only to avoid NPQ effects.

The use of nighttime Chl-a fluorescence proved to be a valid approach for studying temporal variability in Chl-a concentrations in the subtropical oceans (*Winn et al.*, 1995). We select nighttime profiles taking into account the local time of day at each profile location, local sunrise and sunset times. Local times for sunrise and sunset were calculated using MATLAB functions from the AIR-SEA Toolbox (version 2.0) that were adapted by Rich Pawlowicz. Some Argo floats and elephant seals profiled south of the Antarctic Circle (i.e., 117 float profiles and 50 seal profiles south of 66.6° S), and therefore sampled in areas of continuous day or night. Nearly 63% of the Argo profiles, 50% of EM-APEX and 44% of elephant seal profiles were sampled during the night (i.e., 3502 profiles). A number of these did not acquire data near the surface (i.e. above 10-m depth) or were incomplete and were discarded, and a total of 2805 nighttime profiles are analyzed in this study.

Depth-dependent changes in light attenuation can lead to changes in phytoplankton intracellular pigment concentration due to photo-acclimation (see, e.g., *Cullen*, 1982), and a subsurface Chl-a maximum does not necessarily correspond to a phytoplankton biomass increase. Optical backscattering (Bb), a proxy for particle

concentration, provides another index of phytoplankton biomass in the open ocean that covaries with phytoplankton biomass (*Behrenfeld et al.*, 2005; *Martinez-Vicente et al.*, 2013) but is not susceptible to photo-acclimation (*Behrenfeld and Boss*, 2003). Kendall's concordance coefficient is a non-parametric test suitable for testing monotonic positive relationships among variables that are intended to estimate the same general property (*Legendre*, 2005; *Cullen and Eppley*, 1981). The parameter ranges from 0 (no agreement) to 1 (complete agreement). For the float data for which Bb measurements are available, over 96% of concomitant nighttime Chl-a fluorescence and Bb profiles show good agreement, based on Kendall's concordance parameter greater than 0.9 (and 99% give a parameter greater than 0.8). Therefore, we infer that vertical profiles of Chl-a fluorescence in the Southern Ocean are to first order dominated by changes in phytoplankton biomass, in agreement with satellite based assessments (*Siegel et al.*, 2013).

Before attempting to locate subsurface Chl-a fluorescence maxima, all profiles were smoothed by applying a 3-point median filter in order to suppress single-point subsurface maxima that could be associated with random noise. *Briggs et al.* (2011) proposed a higher-order filter, but we found that for our data, the higher-order filter significantly truncated the magnitude of the subsurface maxima, and that a 3-point median filter suppressed subsurface maxima represented by a single point.

3.3.1 Profile Fits and Deep Chl-a Maxima

Because subsurface Chl-a fluorescence profiles exhibit well-defined maxima (i.e., above the instrument noise level) below the surface that are not necessarily larger in magnitude than the surface value, a criterion based on a percentage increase relative

to the surface (e.g *Grenier et al.*, 2015) may underestimate the occurrence of deep Chl-a fluorescence maxima (DFM). Thus, we identify profiles with DFM by fitting the Chl-a fluorescence profile shape to functional forms expected to represent a wide range of regimes: (a) a sigmoid profile characterized by a well mixed homogeneous layer, (b) a surface intensified exponential, (c) a Gaussian representing Chl-a maxima; as well as the combination of (d) a Gaussian with a sigmoid and (e) a Gaussian with an exponential (Fig. 3.2). Equations for all the different functional forms largely follow the ones used by *Mignot et al.* (2011), and are presented in the Appendix. First guesses for fitted parameters were estimated from the observed profiles. In particular, the depth of the Chl-a maximum was chosen based on the most prominent subsurface Chl-a fluorescence maximum (i.e., the greatest peak relative to the largest neighboring minima) if greater than the instrument noise level (i.e., 0.02 mg m^{-3}); otherwise, the surface value was chosen. The most prominent subsurface peak was usually deeper than the largest peak, which is based on Chl-a fluorescence absolute values (i.e., irrespective of neighboring values) that generally increase toward the surface. This choice was preferred to avoid Gaussian fits with insignificant maxima close to the surface, and to avoid missing profiles with prominent DFM below the surface mixed layer.

Among all fitted models, the best fit for each profile was chosen based on a 95% confidence Chi-square test for goodness of fit (e.g. *Press et al.*, 2007), which takes into account the number of fitted parameters for each functional form. That is, for each fitted fluorescence profile we computed $\chi^2 = \sum_{k=1}^{N} \frac{(F_k - \mu_k)^2}{\sigma^2}$, where N is the number of observations in each profile, F_k is the observed and μ_k the modeled fluorescence value at each depth level, considering a constant $\sigma^2 = 0.04$ mg m^{-3} (i.e.,

twice the instrument noise level in deep water). Thus, large values of the sample Chi-squared indicate significant deviations from the modeled values. The smallest profile Chi-squared (i.e. between all functional forms tested) was compared to the critical Chi-squared value (i.e. for a 5% significance level) from a theoretical Chi-squared distribution with $\nu = N - m$ degrees of freedom, where m is the number of fitted parameters in the model (see Appendix). If the profile Chi-square was smaller than the critical Chi-square then the fitted profile was chosen as the best model fit; otherwise, it was rejected.

Although a significant number of profiles were fitted to non-Gaussians (i.e. 40% were either (a) or (b)), most were fitted to Gaussians (i.e. 60% of profiles were either (c), (d) or (e)). Non-Gaussian profiles were almost all sigmoids (i.e. 97%), and most Gaussians were embedded in a homogeneous layer (i.e. 58% were (c), and the remainder approximately evenly distributed as either (d) or (e)). However, some of the Gaussian fits showed maxima located near the surface (i.e. $\leq$ 20-m depth) and were not considered in our analyses of DFM (i.e. $\sim$ 13 % of Gaussians were discarded).

We took a conservative approach in defining profiles with DFM. Gaussian fits with subsurface maxima (i.e. 47%) were interpreted as having a DFM only if peak prominence was greater than 0.04 mg m^{-3}. In addition, all profile fits were visually inspected for consistency, and in a few cases in which the subsurface maximum was larger in the fit than in the observations, the profile was re-evaluated based on the smallest Chi-square. More than 30% of profiles were classified as having DFM. For all profiles with DFM (i.e. deeper than 20 m), peak magnitude and peak depth in the observations were well correlated with those inferred from the profile fits ($r = 0.96$

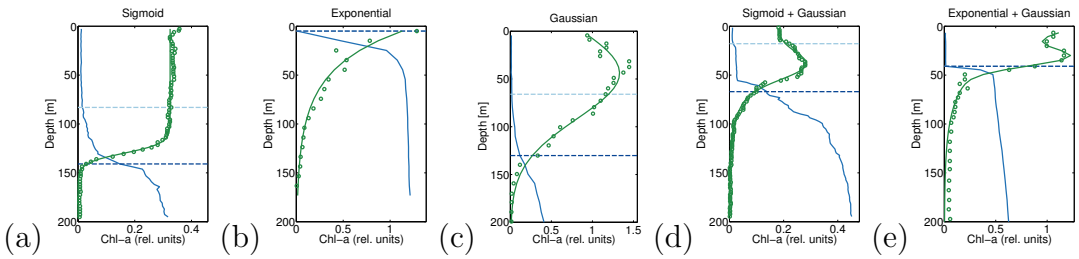

Figure 3.2: Examples of Chl-a fluorescence vertical profiles (relative units) fitted to a (a) sigmoid, (b) exponential, (c) Gaussian, (d) Gaussian + sigmoid and (e) Gaussian + exponential. The best fit (black line) to the observations (circles) was selected based on a Chi-square goodness of fit test with constant standard deviation of twice the instrument noise level (i.e., 0.04 mg m^{-3}) and taking into account the number of fitted coefficients (see Appendix). Density profiles (light gray) with the deepest and shallowest estimate of MLD (dashed gray line) are also shown (rescaled by subtracting the potential density value at the surface).

for peak magnitude and $r = 0.92$ for peak depth, for N=1251 and 99% confidence).

3.3.2 Unevenness Indeces

Chl-a fluorescence gradients and variance within the mixed layer may exist, even if prominent DFM are not well defined. Under the assumption that the overall variability across the region should exceed the variability within a given day mixed layer, the degree of variance of Chl-a fluorescence within the mixed layer is assessed by means of a standard deviation (STD) index, calculated as the standard deviation within the mixed layer for a given profile normalized by the standard deviation of all measurements within the mixed layer for all observations in the Southern Ocean binned together. A more commonly used metric for variance in Chl-a and ecological data is the coefficient of variation, which normalizes the standard deviation by the mean (e.g. *Håkanson et al.*, 2003; *Djavidnia et al.*, 2010). However, the coefficient of variation is only meaningful for variables on a ratio scale (i.e. with a well defined

zero) and not for potential density. Also, because the coefficient of variation uses the mean, it will be sensitive to Chl-a fluorescence absolute values, which are subject to large uncertainties (see Section 3.2.2), and, thus, we opted not to use this metric.

The normalization by a regional standard deviation facilitates the comparison with variance in potential density, which by definition should be homogeneous within the mixed layer. The STD index gives the fraction of variance in a given mixed layer relative to the regional variability. We show the STD index normalizing by the regional standard deviation within mixed layers for each month of the year (Fig. 3.6a), and for June observations only, as representative of austral winter conditions, when variability is expected to be the smallest (Fig. 3.6b). Small values indicate a relatively homogeneous profile. A value close to one indicates that variability within the mixed layer can be as large as the variability in the entire region, whereas values greater than 1 indicate that variability within the mixed layer is larger than the regional variability, and thus imply a relatively heterogenous mixed layer.

Chl-a fluorescence is known to be log-normally distributed (*Campbell*, 1995), and a STD index computed by accounting for log-normality of the data would give larger values than the ones presented here (i.e., ignoring log-normality in the data). The values here are intended to contrast the degree of variability in Chl-a fluorescence within the mixed layer, relative to potential density. The STD index based on the log-normal model gives higher values particularly for the largest threshold criteria (>5), which gives deeper MLD and therefore a greater range of fluorescence, but with the same overall seasonal trends.

The mean vertical gradient within the mixed layer provides another index of inhomogeneities in Chl-a fluorescence in the mixed layer. Fig. 3.6b also shows

absolute values for Chl-a fluorescence and potential density depth averaged over the mixed layer.

3.3.3 Mixed-layer Depth

Estimates of MLD are based on potential density referenced to the surface. Potential density was computed from *in situ* temperature and salinity profiles using the international thermodynamic equation of seawater (TEOS-10) and the MATLAB Gibbs Seawater (GSW) Oceanographic Toolbox from *McDougall and Barker* (2011). The floats employ a Sea-Bird SBE-41 CTD, which is expected to resolve differences in density of 0.002 kg m^{-3} (*Kilbourne and Girton*, 2015).

We use standard MLD definitions from *Holte and Talley*'s (2009) algorithm, including threshold (i.e., density difference from the surface) and density gradient criteria, as well as several other thresholds (MATLAB code are available at http://mixedlayer.ucsd.edu). We show results for *Holte and Talley*'s (2009) density algorithm, the most commonly used density thresholds: 0.03 kg m^{-3} (*de Boyer Montégut et al.*, 2004) and 0.125 kg m^{-3} (*Kara et al.*, 2000; *Boss et al.*, 2008; *Boss and Behrenfeld*, 2010); as well as fine-density thresholds that have been proposed to better capture the mixing layer depth: 0.01 kg m^{-3} (e.g. *Brainerd and Gregg*, 1995; *Thomson and Fine*, 2003; *Mignot et al.*, 2016) and 0.005 kg m^{-3}(*Kilbourne and Girton*, 2015). In all cases we use a surface reference depth of 10 m that avoids capturing effects of diurnal restratification (*de Boyer Montégut et al.*, 2004).

The MLD computed from individual profiles using relatively large thresholds (0.03-0.125 kg m^{-3}) represents the depth through which physical properties have been mixed in the recent past (i.e., last day or few days), but it does not give information

on how deep active mixing is reaching at the time and location when the profile is sampled. The MLD defined as the depth where density is 0.03 kg m^{-3} greater than the surface depicts the seasonal mixed layer and better captures the first spring restratification than the canonical larger criterion of 0.125 kg m^{-3} (*de Boyer Montégut et al.*, 2004), which usually gives very deep MLDs.

The MLD detection algorithm from *Holte and Talley* (2009) is designed to better capture the base of the homogeneous layer in weakly stratified regions, and often gives shallower MLDs than the threshold criterion, which is also the case for the float and elephant seal data (r=0.82, p <0.01). The fine-density threshold criteria (0.01 kg m^{-3} and 0.005 kg m^{-3}) often captures the actively mixing layer based on comparisons with microstructure data (*Brainerd and Gregg*, 1995). In a recent assessment of mixing layer depth, using a larger set of EM-APEX floats deployed during DIMES cruises, *Kilbourne and Girton* (2015) find a density threshold criteria of 0.005 kg m^{-3} to be more representative of the homogeneous layer in the Southern Ocean, which is largely driven by mechanical wind mixing.

3.4 Results

3.4.1 Deep Chl-a Fluorescence Maxima

Approximately 47% of profiles were fitted to Gaussian forms, most of which showed subsurface Chl-a maxima deeper than 10-m depth and were identified as having a DFM ($\sim$ 30%, see Section 3.3.1). We quantify the percentage of profiles with DFM in each season (Figure 3.3). The fraction of profiles with deep Chl-a maxima is larger in the summer (Fig. 3.3a) when strong stratification occurs, but the occurrence

of profiles that show subsurface enhancement is significant year round in float data. DFM in stratified surface waters are widespread features in the global oceans and can result from a broad range of interacting processes: local maxima in phytoplankton growth rates close to the nutricline, photo-acclimation of phytoplankton cells due to reduced light levels at depth, and/or physiologically influenced behavior of phytoplankton (e. g. swimming or buoyancy control) that can lead to aggregation in layers (for a review see *Cullen*, 2015). Although not as frequent and prominent as DFM characteristic of oligotrophic regions (Fig. 3.3b top, and see e.g. *Mignot et al.* (2014)) or coastal environments (e.g. *Cullen and Eppley*, 1981), DFM are not uncommon in the Southern Ocean and may occur regardless of the season.

Float data show a larger percentage of profiles with DFM than do elephant-seal data (Fig. 3.3a), with more than half of the profiles recorded in summer presenting DFM for float data. We hypothesize that this is because elephant seals and floats sample different oceanic regimes. While floats are advected by ocean currents at 1000-m depth, with no preference for surface Chl-a values, southern elephant seals forage over continental shelves, near fronts and eddies that promote localized small-scale blooms (*Campagna et al.*, 2006; *Charrassin et al.*, 2010; *Bailleul et al.*, 2010), which makes them biased samplers. Southern elephant seals off the Kerguelen Islands exploit the edge and core of highly turbulent eddies (*Bailleul et al.*, 2010), where Chl-a is expected to be well mixed throughout the water column. Also, the coarser resolution in elephant seal profiles suggests that some subsurface features may be missed, giving a smaller percentage of Chl-a profiles with DFM (Fig. 3.3a).

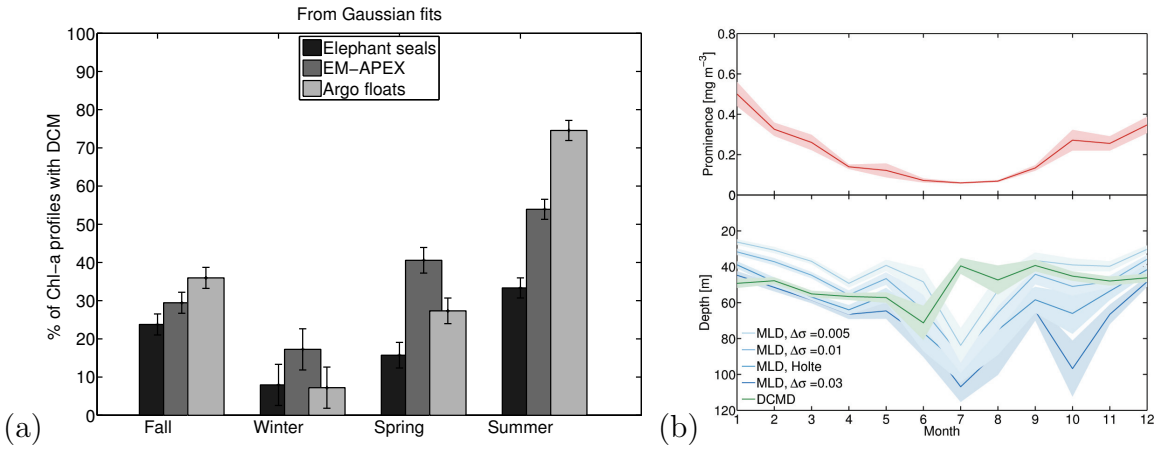

Figure 3.3: (a) Percentage of Chl-a fluorescence profiles with DFM for elephant seals (black), EM-APEX floats (dark grey) and Argo floats (light grey), considering a DFM when a profile was fitted to a Gaussian and showed a prominent peak below the surface (see Section 3.3.1). Error bars give the 95% confidence interval estimated from a bootstrap method. (b) Seasonality of DFM peak prominence (top), MLD and DFMD (bottom).

3.4.2 Deep Chl-a Maximum Depth and Mixed-layer Depth

The depth of the deep Chl-a maximum (DFMD) can lie above or below the MLD, depending on physical conditions and on the definition used for a mixed layer (Fig. 3.3b, bottom). For standard MLD definitions, DFMD is on average found above base of the mixed layer throughout the year, suggesting the existence of gradients within a hydrographically mixed layer defined using relatively large threshold criteria (e.g. *Holte and Talley*'s (2009) algorithm, the 0.03 kg m^{-3} density threshold criterion or 0.125 kg m^{-3} (not shown)). For fine-density threshold criteria, mean DFMD more often lies below the MLD from summer through fall, suggesting fine-density threshold criteria may better capture a homogeneous layer in Chl-a during that that time of the year.

Probability density of occurrence functions between DFMD and MLD better illustrate the sensitivity of DFMD relative to the MLD for each MLD definition

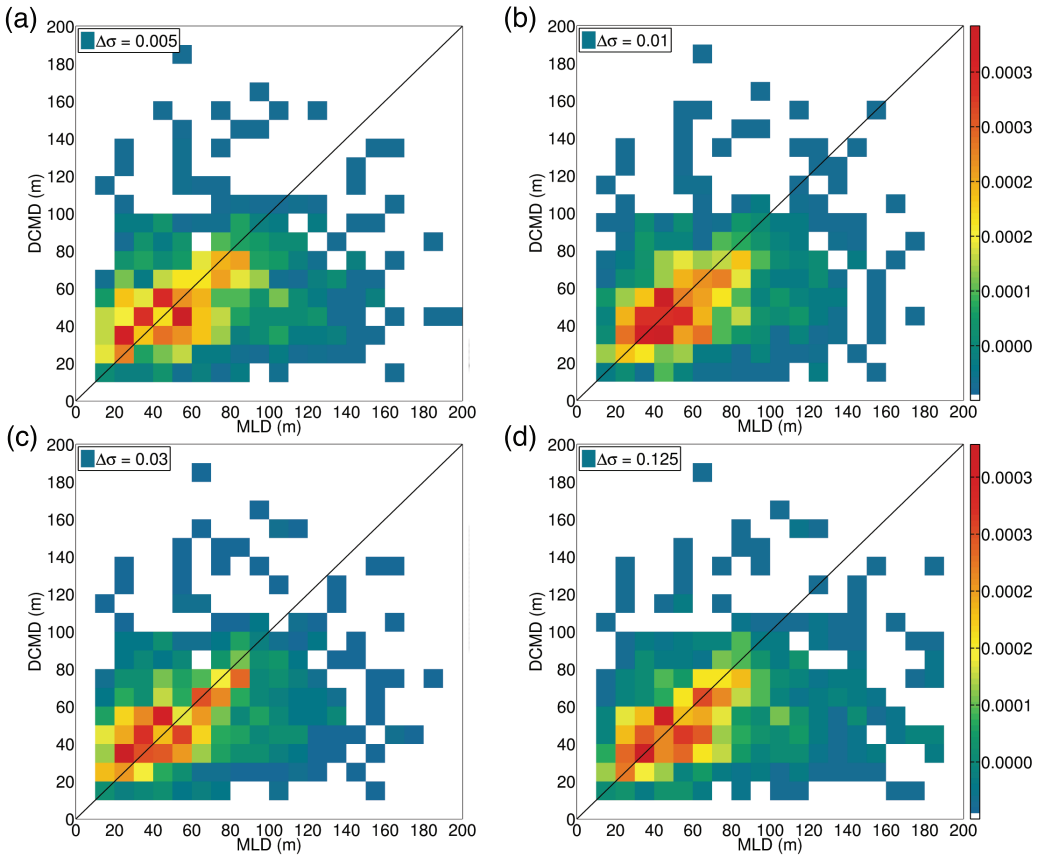

Figure 3.4: Two-dimensional probability density of occurrence functions between deep Chl-a-maximum depth (DFMD) and the MLD using a fine-density threshold of (a) 0.005 kg m^{-3}, (b) the density algorithm from *Holte and Talley* (2009), and density thresholds of (c) 0.03 kg m^{-3} and (d) 0.125 kg m^{-3}. Data includes only nighttime profiles from elephant seals, EM-APEX and Argo floats characterized by having DFM.

(Fig. 3.4). DFMs are more often found at the base of the mixed layer, but a significant fraction of profiles with DFMs lie below as well as above the MLD, even for the fine-threshold criterion of 0.005 kg m^{-3}, more closely related to the mixing-layer depth.

The percentage of profiles with DFMs that are shallower than the MLD for each month of the year and MLD definition is shown in Fig. 3.5a. Smaller density-threshold criteria generally show a lower percentage of profiles with DFM above the MLD than do larger threshold criteria, except in wintertime when the MLD is deep,

(a)

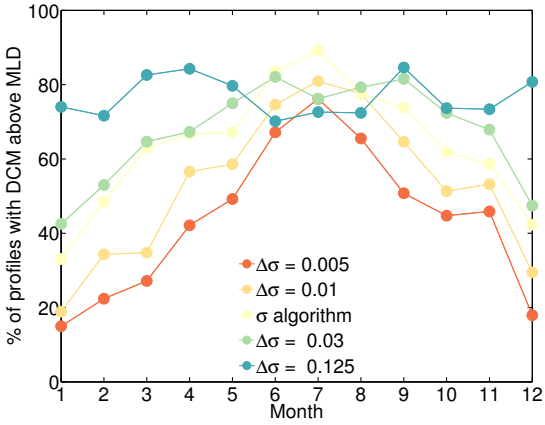

Figure 3.5: (a) Percentage of profiles with DFM above the MLD for different definitions of mixed layer in each month of the year.

and all definitions agree showing DFMD within the MLD. There is a wide range of variability in the fraction of profiles with DFM above the MLD for the different MLD definitions, varying between 20% to 80% in the phytoplankton growing seasons. This large range of variability holds even for more stringent definitions of DFM. For example, a larger choice of threshold for a Chl-a fluorescence prominent peak in our definition of DFM reduces the number of profiles with DFM in winter, but the trends and large variability among the different MLD criteria remain for other seasons in Fig. 3.5a.

3.4.3 Chl-a Variability in the Mixed Layer

Of all Chl-a fluorescence nighttime profiles evaluated in this study, over 60% were fitted to non-sigmoid forms, suggesting some degree of variability or gradients within the mixed layer regardless of whether a DFM is identifiable. During the phytoplankton growing season (September-March), the percentage of non-sigmoid profiles increases to 75%. As additional measures of inhomogeneities within the hydrographic mixed layer, we present monthly mean vertical gradients as well as the STD index

within the mixed layer for Chl-a fluorescence (see Section 3.3), which we contrast against potential density (Fig. 3.6).

Density profiles for most definitions (with the exception of the largest threshold criterion) show little variability in the mixed layer relative to the regional variability in each month, with a STD index of <0.05 year round (Fig. 3.6a, blue). In contrast, Chl-a fluorescence profiles vary by a larger fraction of the regional variability for all definitions used for the MLD (Fig. 3.6a, green), regardless of Chl-a absolute values (which do show seasonality). The monthly averaged STD index for Chl-a fluorescence in the mixed layer varies between ~ 0.1 for fine-density threshold criteria and nearly 0.5 for the largest threshold used for a mixed layer, and it is consistently larger than for potential density for all definitions of MLD.

A large range of variability in Chl-a fluorescence is not uncommon in bio-optical data (*Campbell*, 1995). How homogeneous is Chl-a fluorescence expected to be within the mixed layer? The STD index allows to compare variability within the mixed layer, relative to the regional variability in winter, when presumably the relatively stronger activity of storms (e.g. *Simmonds et al.*, 2003; *Ulbrich et al.*, 2009) is expected to homogenize properties across the upper Southern Ocean. Thus, one should expect that the variance within the mixed layer for a given profile will be less than the regional variance across all mixed-layer measurements in winter. When we normalize by the regional variability in winter, we find that the monthly averaged STD index for Chl-a fluorescence in the mixed layer varies between ~ 0.1 for a fine-density threshold criterion and over 1.6 for the the largest threshold, but the range of variability will be largest if a log-normal model is used to compute the STD index (see Section 3.3.2).

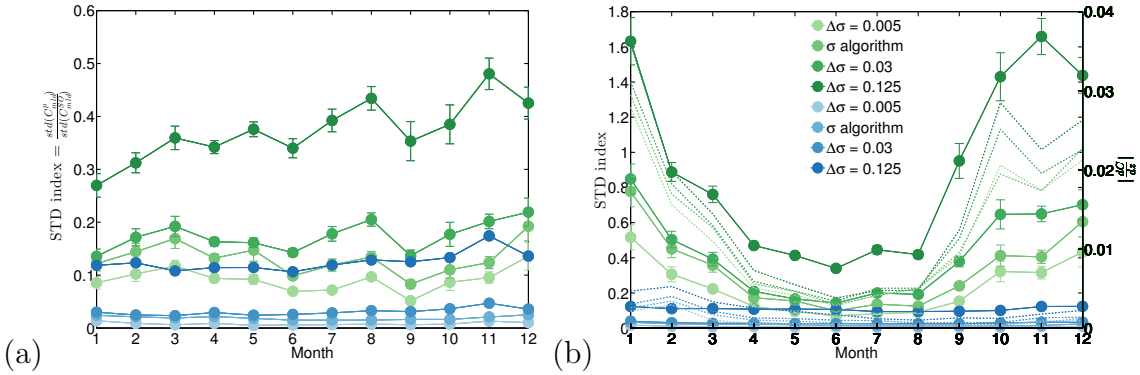

Figure 3.6: STD index within the MLD (i.e. the standard deviation within the mixed layer normalized by the regional standard deviation) for Chl-a fluorescence (green) and potential density (blue). Shades of blue and green indicate different MLD definitions (see legend). Error bars were computed by error propagation of the ratio. (a) Normalizing by the regional standard deviation in each month, and (b) normalizing by the winter standard deviation for the region (see Section 3.3.2). Mean vertical gradients (i.e. averaging absolute values) are also shown in dashed lines (right y-axis) in (b).

When compared against the winter regional variability in the mixed layer, the inhomogeneity in Chl-a fluorescence profiles within the mixed layer is not only dependent upon the definition used for a MLD, but also on season (Fig. 3.6b, thick lines). There is greater variability within hydrographic mixed layers during the phytoplankton growing season. In general, Chl-a fluorescence in the mixed layer is more homogeneous in late fall and winter, consistent with the seasonal deepening of the MLD and a hydrographic mixed layer more closely related to the mixing layer (*Chiswell*, 2011). Departures from homogeneity relative to the winter variability (i.e. STD index>0.2) occur in late winter, when sudden restratification may occur (see e.g. Fig. 3.1b and c) and the MLD is likely a poor proxy for the mixing layer depth. Vertical gradients in Chl-a fluorescence within the mixed layer show similar seasonality (Fig. 3.6b, dashed lines), albeit with larger mean values for Chl-a fluorescence relative to vertical gradients in potential density through the fall as well.

3.5 Discussion and Conclusions

New bio-optical data from floats and Southern elephant seals show that, even in the open Southern Ocean, where year-round harsh weather conditions might be expected to homogenize properties within mixed layers, subsurface Chl-a fluorescence maxima are not uncommon, and that Chl-a fluorescence may not be well mixed within the seasonal (hydrographically defined) mixed layer.

Southern Ocean DFM, although not as large as subsurface Chl-a fluorescence maxima found in subtropical regions, can occur in all seasons, albeit with higher frequency of occurrence in summer. The occurrence of deep Chl-a maxima in the Southern Ocean has been documented (*Holm-Hansen et al.*, 2005; *Charrassin et al.*, 2010). *Holm-Hansen et al.* (2005) indicated that deep Chl-a maxima are predominant over deep ocean basins, where enrichment of surface waters with Fe from coastal sediments or upwelling processes are minimal, and in pelagic waters south of the Polar Front where Chl-a concentrations in the upper mixed layer are very low (generally < 0.2 mg m^{-3}). Elephant seal data showed numerous areas to be characterized by deep fluorescence maxima that were undetectable with satellites, with fluorescence intensities up to 5 times the surface values (*Charrassin et al.*, 2010), and were also observed in nighttime profiles by *Biermann et al.* (2015). Deep Chl-a maxima are usually characteristic of the summer season when the upper ocean is well stratified and a seasonal mixed layer develops (e.g., *Holm-Hansen et al.*, 2005; *Gaube et al.*, 2013; *Mignot et al.*, 2014).

Subsurface Chl-a fluorescence maxima are more often found at or near the base of the MLD, suggesting a strong dependence on turbulence levels for Chl-a accumulation at depth in the Southern Ocean. The observation that DFMD are more

often found close to the MLD suggests the importance of physical mechanisms in the formation and maintenance of DFM, but identifying the mechanisms of maintenance of DFM layers requires data that are unavailable from autonomous platforms (e.g. phytoplankton specific growth rates, species composition and depth distribution of grazing pressure) and is outside the scope of this study.

Perhaps more important, regardless of the definition chosen for mixed layer, is that a significant number of DFM are found within the mixed layer. This is true year round for the most commonly used definitions of MLD (e.g. *de Boyer Montégut et al.*, 2004; *Holte and Talley*, 2009), including during winter and spring for the best estimate of the Southern Ocean mixing-layer depth, which can be inferred from fine-density threshold criteria (*Kilbourne and Girton*, 2015). The large range of variability in the fraction of profiles with DFM above the MLD for different MLD definitions (∼20-80%) suggests that caution should be exersized when defining the layer that is assumed to be mixed in Chl-a fluorescence, since nearly 20% of profiles with subsurface fluorescence enhancement will show the deep maxima above the MLD (even if a fine-density threshold criterion for MLD detection is used). Particularly in summer, whether the DFM lies above or below the MLD is largely dependent on the threshold criterion for MLD detection chosen. The fact that most profiles with DFM lie below the MLD defined by fine-density thresholds, but above MLDs defined by larger threshold criteria, suggests that reduced turbulence in remnant mixed layers may allow for DFM to form below the actively mixing layer that is in direct contact with the wind. The presence of ubiquitous fronts in the Southern Ocean, where convergences/divergences lead to plankton accumulation may also lead to DFM (*Franks and Walstad*, 1997b; *Taylor et al.*, 2012; *Powell and Ohman*, 2015) and gradients

within mixed layers.

Chl-a fluorescence maxima above the MLD suggest the existence of gradients within the hydrogaphically defined mixed layer, implying that Chl-a fluorescence may not be homogeneous within the homogeneous layer in density at the time of profiling. The ratio of variability within a given day mixed layer and the regional variability across Southern Ocean mixed layers is remarkably constant year round for all but one definition of MLD (i.e., the 0.125 kg m^{-3} threshold criterion), and Chl-a is consistently more heterogeneous than density for all definitions. Chl-a fluorescence variability within the mixed layer for a given day is, on average, between 20% and 50% the regional variability across the entire Southern Ocean, which is consistently higher than the 5% for potential density. Although the STD index for the mixed layer relative to wintertime regional variability indicate relatively homogeneous profiles in winter, Chl-a fluorescence variance and vertical gradients are significantly larger, compared with potential density, during the phytoplankton growing season.

The existence of gradients and unevenness in Chl-a fluorescence within mixed layers presented here indicates periods when the biological timescale of adaptation to the light gradient is faster than the rate of mixing through the light gradient. Although the existence of Chl-a fluorescence gradients can result from physiological adaptation to ambient light and does not necessarily imply gradients in phytoplankton biomass (e.g. *Cullen and Eppley*, 1981), observations in the North Atlantic have shown that phytoplankton can be unevenly distributed in deep winter mixed layers (*Ryther and Hulburt*, 1960).

Our results suggest that intermittent atmospheric forcing may allow for long enough periods of quiescence and reduced turbulence in deep mixed layers, resulting in

DFM and/or Chl-a unevenness within the seasonal mixed layer. Southern Hemisphere extratropical cyclones can have life spans between 2-10 days, but considering the mean duration of storms that persist beyond 1 day is just over 3 days (*Simmonds and Keay*, 2000), and that typically the frequency of occurrence is roughly one storm per week at any given location over the storm tracks, a period of 3-4 days of quiescence between storms can be sufficient for biological processes to take place before the next mixing event homogenizes the mixed layer.

This study aims to emphasize that the absence of density stratification in the mixed layer does not imply vertical mixing and homogeneous layers in other properties. Our results confirm that the mixed layer defined by standard density threshold criteria is a poor indicator of the active turbulent layer (*Franks*, 2014), and fine-density threshold criteria are usually a better proxy for the depth of active turbulence (except in spring, when all definitions seem to fail at capturing the turbulent layer). These observations suggest intermittent turbulence within mixed layers may occur more often than commonly assumed, and assuming biogeochemical tracers are well mixed in a hydrographically defined mixed layer can be dangerous and may lead to erroneous interpretations.

3.6 Appendix

Appendix: Profile Fits

The equations for the functional forms fitted to the profile data are those presented by *Mignot et al.* (2011), or linear combinations of them. These are a sigmoid (a):

$$F(z) = \frac{F_{surf}}{1 + e^{(Z_{1/2} - z) * s}}, \tag{3.1}$$

with $m = 3$ fitted coefficients: a surface value,F_{surf}, the depth where the surface value reduces to one half, $Z_{1/2}$, and the sigmoid fit slope at $Z_{1/2}$, s; an exponential (b):

$$F(z) = F_{surf} e^{-\frac{\ln 2}{Z_{1/2}} z}, \tag{3.2}$$

with $m = 2$ fitted coefficients: F_{surf}, and $Z_{1/2}$; a Gaussian (c):

$$F(z) = F_{max} e^{-\frac{(z - Z_{max})^2}{dz^2}}, \tag{3.3}$$

with $m = 3$ fitted coefficients: the maximum value F_{max}, the depth of the maximum Z_{max}, and a proxy for the maximum thickness, dz; (d) a linear combination of a Gaussian with an exponential:

$$F(z) = F_{surf} e^{-\frac{\ln 2}{Z_{1/2}} z} + F_{max} e^{-\frac{(z - Z_{max})^2}{dz^2}}, \tag{3.4}$$

with $m = 5$ fitted coefficients: F_{surf}, $Z_{1/2}$, Z_{max}, F_{max}, and dz; and (e) a linear combination of a Gaussian with a sigmoid:

$$F(z) = \frac{F_{surf}}{1 + e^{(Z_{1/2} - z) * s}} + F_{max} e^{-\frac{(z - Z_{max})^2}{dz^2}}, \tag{3.5}$$

with $m = 6$ fitted coefficients: F_{surf}, $Z_{1/2}$, s, Z_{max}, F_{max}, and dz.

3.7 Acknowledgments

This work was funded by a NASA NESFF fellowship (NNX12AN41H 001), the NASA Physical Oceanography Program (NNX08AI82G), NSF grants (ARRA OCE0850350 and ANT-0948338) and the Southern Ocean Carbon and Climate Observations and Modeling (SOCCOM) Project funded by National Science Foundation, Division of Polar Programs (NSF PLR -1425989), supplemented by NOAA and NASA. We thank all the people involved in the calibration, deployment and acquisition of subsurface Chl-a data used in this study and for making it available to the science community. Thanks to the DIMES project for the deployment of EM-APEX floats, MBARI and SOCCOM for collecting and making the float data freely available (http://soccom.princeton.edu/content/soccom-observations). Southern elephant seal data were downloaded from www.earth-syst-sci-data.net/5/15/2013/doi: 10.5194/essd-5-15-2013, and bio-optical data from biogeochemical Argo floats are available at http://www.mbari.org/chemsensor/floatviz.htm. We thank James Holte for his MATLAB code to estimate MLD, available at http://mixedlayer.ucsd.edu. The MATLAB function used to estimate sunrise and sunset times is available at http://mooring.ucsd.edu/software/matlab/doc/toolbox/geo/suncycle.html.

Chapter 4

Wind modulation of upwelling at the shelf-break front off Patagonia: Observational evidence

The South-Atlantic Patagonian shelf is the largest chlorophyll-a (Chl-a) hot spot in Southern Ocean color images. While a persistent 1500-km long band of high Chl-a along the shelf-break front (SBF) is indicative of upwelling, the mechanisms that drive it are not entirely known. Along-front wind oscillations can enhance upwelling and provide a nutrient pumping mechanism at shelf break fronts of western boundary currents. Here, we assess wind-induced upwelling at the SBF off Patagonia from daily satellite Chl-a and winds, historical hydrographic observations, cross-shelf Chl-a fluorescence transects from two cruises, and *in situ* winds and water column structure from a mooring site. Satellite Chl-a composites segregated by along-front wind direction indicate that surface Chl-a is enhanced at the SBF with southerly winds, and suppressed with northerly winds. Northerly winds also result in enhanced

Chl-a further offshore (∼25-50 km). Synoptic transects as well as mean hydrographic sections segregated by along-front winds show isopycnals tilted upward for southerly winds. Spring observations from the mooring also suggest that southerly winds de-stratify the water column and northerly winds restratify, in agreement with Ekman transport interacting with the front. Moreover, changes in water column temperature lag along-front wind forcing by about 3-4 days, consistent with estimates of Ekman spin-up time for the spring. Our results suggest that oscillations in along-front winds, on timescales typical of atmospheric storms (2-10 days), can significantly modulate the upwelling and productivity at the SBF off Patagonia, revealing the importance of wind-induced upwelling for shelf-slope exchange at shelf-break fronts of western boundary currents.

4.1 Introduction

Continental shelves support high primary productivity and are responsible for more than 40% of the carbon sequestration of the world's ocean (e.g. *Muller-Karger*, 2005). The Patagonian shelf, located along the eastern coastline of South America from about 38°S to 55°S, is a productive marine environment comparable to those found in upwelling systems of eastern boundary currents (e.g. *Carr and Kearns*, 2003; *Garcia et al.*, 2008), in terms of primary productivity (*Garcia et al.*, 2008; *Lutz et al.*, 2010; *Segura et al.*, 2013) and higher trophic levels (*Acha et al.*, 2004; *Bogazzi et al.*, 2005; *Campagna et al.*, 2006; *Falabella*, 2009) The Patagonian shelf stands out as a hot spot in satellite chlorophyll-a (Chl-a), indicative of phytoplankton abundance, with typical Chl-a values an order of magnitude larger than those found in the open ocean sustaining the largest marine ecosystem of the Southern Hemisphere (*Bisbal*,

1995; *Longhurst*, 2007; *Heileman*, 2009). Large diatom blooms are responsible for substantial rates of absorption of atmospheric CO_2 (*Schloss et al.*, 2007; *Garcia et al.*, 2008; *Carreto et al.*, 2016), making the region one of the strongest CO_2 sinks per unit area of the world's ocean (*Bianchi*, 2005; *Bianchi et al.*, 2009; *Arruda et al.*, 2015).

A prominent narrow band of high satellite Chl-a along the shelf break closely follows the 200-m isobath (see Fig. 4.1a) and is persistent in climatological means (e.g. *Acha et al.*, 2004; *Saraceno et al.*, 2005; *Rivas*, 2006; *Romero et al.*, 2006; *Signorini et al.*, 2006). Such persistent enhancement of Chl-a at the shelf break is indicative of upwelling of nutrient-rich waters, but the mechanisms that drive such upwelling are still under debate (see Section 4.2). Regardless of the mechanism behind the formation and maintenance of the strong upwelling at the shelf break front (SBF) off Patagonia, winds have the potential to enhance the nutrient supply to the euphotic zone and may impact Chl-a concentrations by several means.

On scales of atmospheric synoptic storms, high winds can enhance surface Chl-a concentrations through enhanced mechanical wind mixing (e.g. *Swart et al.*, 2014; *Carranza and Gille*, 2015). Over the Patagonian shelf, high winds enhance satellite Chl-a over the northern shelf in summer, when strong stratification that inhibits the exchange with presumably nutrient-rich subsurface waters develops, but correlations between wind speed and Chl-a anomalies are generally low over the shelf break, showing relative minima (see *Carranza and Gille*, 2015, their Fig. 7a).

Wind directionality, however, can also modify upwelling rates near fronts. Directional winds may interact with the frontal circulation and modulate the location and intensity of the upwelling. Theoretical and numerical studies supported by observations have shown that winds and diabatic vertical mixing can modify the

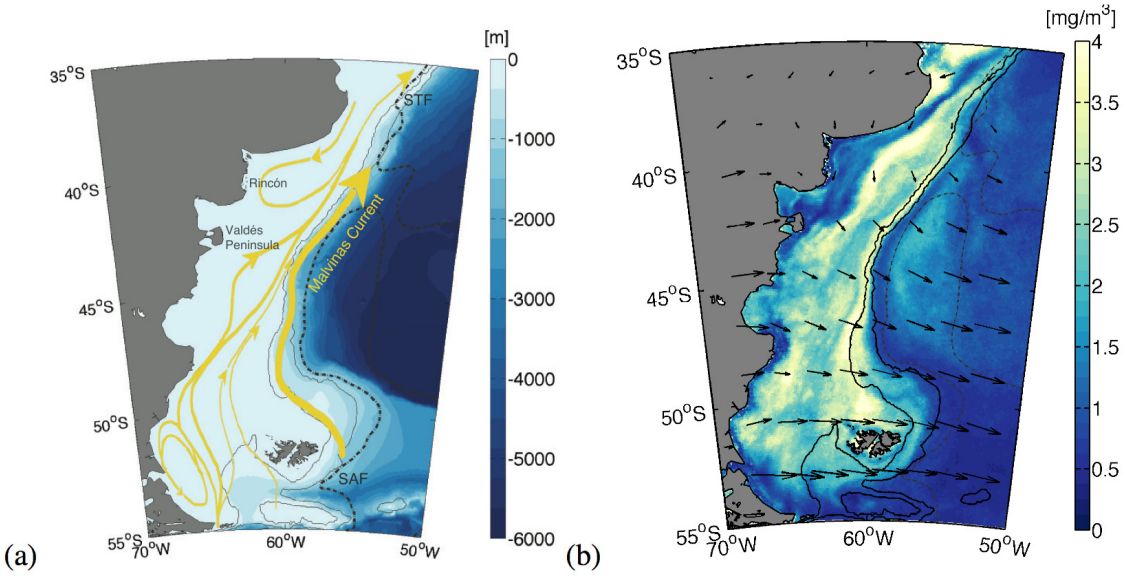

Figure 4.1: (a) Bathymetry of the Patagonian shelf from GEBCO with schematic of mean circulation, adapted from *Piola and Falabella* (2009). (b) Chl-a amplitude (annual maximum - annual minimum) based on monthly means for the period 2000-2011, with mean summer wind vectors overlaid. Solid black contours indicate the 200m and 1000m isobaths. The Sub-Antarctic Front (SAF) from *Orsi et al.* (1995) is shown by the dashed black line.

ageostrophic vertical circulation associated with open ocean fronts (e.g. *Thompson*, 2000; *Thomas and Lee*, 2005; *Nagai et al.*, 2006; *Thomas and Ferrari*, 2008). Down-front winds (i.e. in the direction of the frontal jet) can enhance frontogenesis as a consequence of wind-driven gravitational instabilities and non-linear Ekman pumping, modifying upwelling/subduction rates in mesoscale oceanic fronts (*Thomas and Lee*, 2005; *Thomas and Ferrari*, 2008). In the vicinity of a jet, enhanced upwelling may also be caused by along-front wind stress (wind−surface current) variations in the cross-front direction itself (*Dewar and Flierl*, 1987; *Zhang et al.*, 2013).

At shelf-break fronts of western boundary currents, oscillations in the along-front component of the winds can also modulate the upwelling, providing a mechanism for transient nutrient supply to the euphotic zone (*Houghton et al.*, 1988; *Franks and*

Walstad, 1997a; *Fratantoni*, 2003; *Siedlecki et al.*, 2011), with stronger oscillating winds of longer periods resulting in higher biological production. Based on a numerical model configured for the MAB, *Siedlecki et al.* (2011) suggest that when wind oscillations are aligned with a shelf-break front, Ekman transport in the surface layer can tilt the isopycnals associated with the front changing cross-front circulation patterns and frontal upwelling. At a SBF that separates less dense shelf waters from denser open ocean waters and in the absence of alongshore pressure gradients, up-front winds are expected to flatten isopycnals, producing upwelling of nutrient-rich waters in the Bottom Boundary Layer (BBL) from the slope onto the shelf (i.e. on-welling, see *Siedlecki et al.* (2011)). The reversal of the winds (i.e., down-front winds), by steepening isopycnals, provides a mechanism for nutrient pumping to the euphotic layer, with potential consequences for primary production. For the Patagonian shelf configuration, upwelling at the SBF would be favored by southerly winds (i.e. from the south) associated with onshore Ekman transport in the surface layer, and more vertical isopycnals. In contrast, northerly winds (i.e. from the north) with associated Ekman transport offshore tend to restratify and flatten isopycnals at the front (see schematic in Fig. 4.2, adapted for the Southern Hemisphere from *Siedlecki et al.*, 2011).

Although winds in the Patagonia region are not predominantly upwelling favorable or downfront with respect to the western boundary current, synoptic weather (i.e., wind fluctuations of 2-10 days, (e.g. *Vera*, 2003)) can produce wind patterns that substantially deviate from the prevailing westerly mean wind fields (*Jones and Simmonds*, 1993; *Vera*, 2003; *Eichler and Gottschalck*, 2013), and variability in the along-shelf component of the winds can potentially modulate the upwelling and pro-

ductivity of the SBF off Patagonia.

This study takes advantage of satellite data and the existing *in situ* observations in the region to evaluate the hypothesized wind-induced upwelling mechanism associated with along-front wind oscillations and the interaction with frontal isopycnals (*Siedlecki et al.*, 2011), although upwelling due to differential wind stress is also discussed. We use high-resolution satellite observations of winds and ocean color as well as hydrography and *in situ* Chl-a fluorescence measurements from cruises and a mooring site to assess whether along-front winds modulate the upwelling at the SBF off Patagonia, and to what extent these upwelling patterns modulate biological productivity. We address the biological impact of the oscillating wind effect on the upwelling through the Chl-a response. Section 4.2 describes general characteristics of the Patagonian shelf region and proposed mechanisms for the local upwelling at the shelf break. In Section 4.3 we present the data sources used. Satellite-based results suggest that along-front winds can modulate Chl-a at the SBF potentially through isopycnal tilting, and are presented in Section 4.4.1. Synoptic evidence of isopycnal tilting under opposing along-front wind conditions from hydrographic sections across the SBF (Section 4.4.2), as well as composite sections from historical hydrographic stations segregated by wind direction (Section 4.4.3) are also in agreement with the theory (*Siedlecki et al.*, 2011). Further evidence of wind-driven upwelling from a SBF mooring site that acquired meteorological and water column hydrographic data is presented in Section 4.4.4. Results are further discussed in Section 4.5 and conclusions follow in Section 4.6.

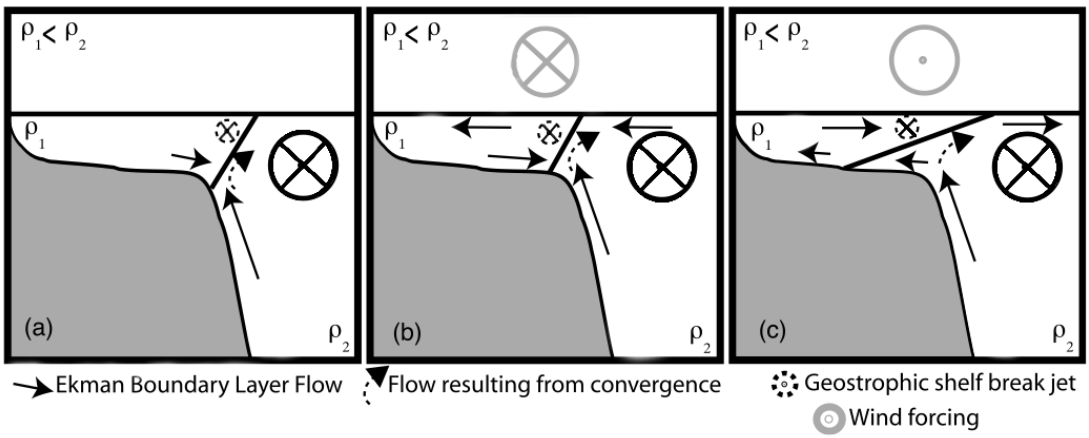

Figure 4.2: Schematic diagram showing the effect of along-front winds on the upwelling at a shelf-break front, adapted for the Southern Hemisphere and modified from *Siedlecki et al.* (2011). In their model, alongshore variations (i.e., frontal meandering and eddies) are neglected. Frontal structure with (a) no-wind forcing, (b) southerly winds, and (c) northerly winds. Southerly winds lead to Ekman transport in the surface layer onshore, steepening frontal isopycnals and enhancing the upwelling at the shelf break, whereas northerly winds lead to offshore Ekman transport, flattening isopycnals and suppressing upwelling at the SBF. Note that for the no wind scenario, the presence of a slope jet with strong shear in their model produces a reversal of the flow at depth over the slope and, hence, convergence in the BBL. The role of this process in the Patagonian SBF is questionable due to the presence of a strong slope current, and the dominant mechanism at play is uncertain (see e.g. *Matano and Palma*, 2008). Nonetheless, upwelling is expected to occur at the SBF off Patagonia in the no-wind case as well, and we kept the arrows as in the original schematic.

4.2 Background: General characteristics of the Patagonian shelf and physical mechanisms for shelf-break upwelling

The Patagonian shelf spans over 1.2 million km^2 of ocean and is under the influence of predominantly westerly winds and high tidal energy (e.g., *Palma et al.*, 2004). The circulation over the shelf is characterized by wind-driven northeastward

flow of low salinity waters that outflow from the Strait of Magellan (*Guerrero and Piola*, 1997; *Palma et al.*, 2004). The shelf is bounded on the east by the northward flowing Malvinas Current (i.e., slope western boundary current, see Fig. 4.1a) which supplies cold nutrient-rich Subantarctic waters to the shelf (*Piola et al.*, 2010; *Painter et al.*, 2010). On the shelf's outer edge, the 1500-km long SBF separates the Malvinas Current (T<15°C, S_p ∼34.2 psu, e.g. *Valla and Piola*, 2015) from seasonally warmer and relatively fresher shelf waters (S_p <33.9 psu, e.g. *Guerrero and Piola*, 1997; *Palma et al.*, 2008). The transition between shelf and open ocean waters, is therefore characterized by moderate cross-front temperature and salinity gradients (*Romero et al.*, 2006; *Painter et al.*, 2010; *Valla and Piola*, 2015). Observations show that the shelf break salinity front, which closely follows the 33.9 psu isohaline (*Piola et al.*, 2010; *Painter et al.*, 2010), is associated with nitrate maxima, located at or inshore of the surface temperature minimum and density maximum (*Romero et al.*, 2006; *Painter et al.*, 2010; *Poulton et al.*, 2013; *Valla and Piola*, 2015). The seasonal variability in light intensity and nutrient supply to the mixed layer associated with changes in stratification control the strong variability of phytoplankton abundance (*Signorini et al.*, 2006). Though nutrient observations are scarce, recent adjoint sensitivity experiments suggest that phytoplankton productivity is limited by macronutrients (i.e. nitrate) over the shelf, whereas in the outer shelf, productivity is presumably iron limited (*Song et al.*, 2016). Bottom shelf water, presumably rich in iron, could also be a source of iron to the outer shelf (*Siedlecki et al.*, 2012). Therefore, the exchange of water masses across the SBF impacts biological productivity (e.g. *Piola et al.*, 2010; *Brink*, 2016). However, the underlying mechanisms that regulate the cross-shelf exchange between the open ocean and shelf waters in this region are not well

known.

Shelf-break upwelling can be generated by internal processes associated with the convergence and detachment of the BBL over shelves dominated by cyclonic currents (e.g. *Gawarkiewicz and Chapman*, 1992; *Chapman and Lentz*, 1994; *Chapman*, 2002). However, BBL detachment cannot fully explain the strong upwelling inferred from observations at the SBF off Patagonia (*Matano and Palma*, 2008; *Miller et al.*, 2011). *In-situ* and remote sensing observations suggest that intense shelf-break upwelling can reach $13-29$ m day^{-1} (*Valla and Piola*, 2015), while average modelled upwelling rates are 8 m day^{-1} (*Matano and Palma*, 2008; *Combes and Matano*, 2014). Using numerical experiments based on idealized conditions for the Patagonian shelf, *Matano and Palma* (2008) showed that, in the absence of an externally imposed horizontal density gradient and the presence of a strong slope current flowing in the direction of coastally trapped waves (i.e., Malvinas Current), the magnitude of upwelling generated by the detachment of the BBL is very small (i.e. $\sim$0.2 m day^{-1}). Instead, they found that the upwelling at the SBF off Patagonia is mainly driven by horizontal flow divergences due to the spreading of the western boundary current onto the shelf, and the magnitude of the upwelling is proportional to the slope current transport. The shelf-break upwelling mechanism proposed by *Matano and Palma* (2008) is controlled by the along-shelf pressure gradient, which drives downstream divergences of the slope current. Their theory is supported by analytical solutions of the simplified shallow-water equations (e.g. *Miller et al.*, 2011), as well as by higher resolution modeling experiments with realistic bathymetry and forcing (*Combes and Matano*, 2014). *In situ* surface current observations are sparse in the region, and the magnitude of such process remains to be tested with observations.

Although, in the northern sector of the Patagonia continental slope, observations show zonal displacements of the Malvinas current flow and baroclinic jets that are responsible for slope water intrusions to the shelf (*Carreto et al.*, 1995; *Franco et al.*, 2008; *Piola et al.*, 2010, 2013), the steady northward flow is mostly barotropic and strongly controlled by bottom topography (*Vivier and Provost*, 1999; *Piola et al.*, 2010, 2013). In the absence of alongshore variations (i.e., frontal meandering and eddies), oscillating winds may produce net upward pumping of nutrients at the shelf break on sub-seasonal timescales (i.e., <15 days, *Siedlecki et al.* (2011)).

Previous studies that have looked into wind-driven physical controls of satellite Chl-a in the Patagonian shelf region have focused on seasonal to inter-annual timescales or have analyzed case studies, often based on *in situ* observations and models (e.g. *Saraceno et al.*, 2005; *Garcia et al.*, 2008; *Signorini et al.*, 2009; *Machado et al.*, 2013). *Saraceno et al.* (2005) discussed satellite Chl-a variability at the SBF in relation to directional winds in the context of inter-annual variability of spring blooms; years with stronger northerly winds were associated with higher Chl-a concentrations than years when northerly winds were moderate or from the south. They suggested that eastward Ekman transport could result in the interleaving of the different water masses at the SBF and enhance vertical stability, retaining phytoplankton in the euphotic zone (*Podestá*, 1990). Coastally-trapped waves, generated by remote wind forcing, were also suggested as a possible mechanism that could explain 70-day fluctuations in SST and Chl-a 8-day fields (*Saraceno et al.*, 2005), in agreement with previous studies (*Vivier and Provost*, 1999; *Vivier et al.*, 2001). The modulation of the upwelling at the SBF off Patagonia by the winds, on sub-seasonal timescales shorter than 15 days, which is the focus of our study, has not been previously addressed from

observations.

4.3 Data and Methods

4.3.1 Satellite data

We use satellite winds and Chl-a estimates to evaluate the influence of along-front winds on phytoplankton blooms near the SBF off the eastern coast of Patagonia. The long satellite records (i.e., 12 years) allow us to assess statistical significance and complement evidence of wind-induced upwelling at the SBF from *in situ* observations.

Daily satellite Chl-a serves as a proxy for phytoplankton biomass within one optical depth of the surface. The data are available at 9-km resolution, covering the period 2000-2011 for which satellite wind data are also available. We use satellite Chl-a derived using the Southern Ocean SPGANT algorithm (*Mitchell and Kahru*, 2009), which uses the maximum band-ratio algorithm (*O'Reilly et al.*, 1998), but with coefficients fitted to Southern Ocean data, and which merges satellite data from several sensors (i.e. OCTS, SeaWiFS, MODIS-Aqua and VIIRS). Although SPGANT has not been validated against *in situ* Chl-a for this particular region, our conclusions do not rely on Chl-a absolute values and are not sensitive to the choice of the Chl-a dataset used (e.g. Chl-a from GlobColour leads to qualitatively similar results). Because Chl-a is log-normally distributed, for averaging we use a geometric mean, obtained by averaging the logarithm of Chl-a and then inverse-transforming the averaged logarithm (*IOCCG*, 2004).

We use Cross-calibrated Multi Platform (CCMP) 6-hourly winds for the period 2000-2011 (*Atlas et al.*, 2011b). CCMP winds result from a 4-D variational analysis

based on multiple satellite datasets, *in situ* winds and European Centre for Medium-Range Weather Forecasts (ECMWF) analysis winds. Data gaps in CCMP winds are expected due to rain, since satellite wind measurements are affected by rain (*Atlas et al.*, 2011b). CCMP winds are preferred over single-scatterometer winds because they capture the high-frequency variability in the winds and show coherence with high-resolution *in situ* winds from meteorological buoys up to the diurnal scale (*Carranza and Gille*, 2015). In addition, unlike single-scatterometer winds, CCMP winds show no directional bias against *in situ* observations from buoys. Both microwave radiometers and scatterometer measurements are more closely related to wind stress (i.e. momentum relative to the ocean) than to the actual wind (*Atlas et al.*, 2011b), but are reported as 10-m equivalent neutral wind speed for calibration purposes. The conversion of stress to wind speed at 10-m height considers influences of atmospheric stability (*Bourassa et al.*, 2010); however, equivalent neutral winds are also relative to currents (*Kelly et al.*, 2001; *Chelton*, 2004). For this analysis, 25-km resolution winds were linearly interpolated into the 9-km grid of the Chl-a data.

The 9-km resolution of the satellite data resolves frontal variability over spatial scales greater than 18 km. This is sufficient considering that the frontal region (i.e. the horizontal scale over which isopycnals slope upward) from theoretical considerations scales approximately as twice the Rossby radius of deformation (*Franks*, 1992), which gives R$\sim$10-15 km for a density contrast between shelf and slope water masses of $\sim$ 0.8-1 kg m^{-3}, a total water column depth of 200 m, and a range of latitudes between $\sim$38°-50°S characteristic of the Patagonian SBF.

4.3.2 *In situ* observations

We extend the analysis from satellite fields to examine processes occurring throughout the water column in the vicinity of the SBF using the historical database of hydrographic stations collected in the region by the Servicio de Hidrografía Naval (SHN, www.hidro.gov.ar/ceado/ceado.asp) and the Instituto Nacional de Investigación y Desarrollo Pesquero (INIDEP, http://www.inidep.edu.ar/oceanografia/) in Argentina. A summary of all *in-situ* observations used in this study is presented in Table 4.1.

Historical hydrographic stations

We examined the historical database of hydrographic stations from the SHN from 1987 onwards, when CCMP satellite winds are available, as well as stations collected by INIDEP for the years 1992-1998. For this study, we analyzed stations within 200 km of the 200 m isobath, between approximately 38°S and 50°S. We restricted the analyses to stations south of 38°S to avoid buoyancy effects from the La Plata River plume, which outflows anticyclonically towards the north near 36°S, and may hinder dynamical effects at the shelf-break associated with oscillating winds (for the plume extent see e.g. *Piola et al.*, 2000, 2008; *Guerrero et al.*, 2014; *Matano et al.*, 2014). Hydrographic stations for transects across the SBF off Patagonia were sampled in the years 1988-1994, 1996, 1997, 2005 and 2006 during different seasons.

Conductivity-temperature-density (CTD) vertical profiles were available for all stations included in our analyses. Absolute salinity, conservative temperature and derived density from these quantities were computed using the international thermodynamic equation of seawater (TEOS-10) and the MATLAB Gibbs Seawater

(GSW) Oceanographic Toolbox from *McDougall and Barker* (2011).

GEF cruises

In 2005 and 2006, hydrographic stations for transects across the SBF off Patagonia were sampled during Global Environmental Facility (GEF) Patagonia cruises on board R/V ARA Puerto Deseado. Cross-shelf transects were carried out in October 2005 (GEF-1), March 2006 and September 2006 (GEF-3) with a horizontal resolution of ∼25 km. CTD profiles for all GEF cruises are available at the National Oceanographic Data Center, and details of the data processing are reported by *Charo and Piola* (2014). In this work, we present results from two hydrographic transects acquired during GEF-1 and GEF-3 that were sampled with opposing meridional wind conditions, at ∼41°S (off Rincón) and at ∼44°S (off Valdés Peninsula).

During GEF-1 and GEF-3 the CTD was equipped with a SeaPoint Chl-a fluorescence sensor. In addition, 5-liter water samples were collected with a 12-bottle rosette sampler for analysis of dissolved oxygen and Chl-a concentration among other biological parameters (*Lutz et al.*, 2010; *Gómez et al.*, 2011; *Segura et al.*, 2013; *Perez-Cenci et al.*, 2014; *Carreto et al.*, 2016). Water samples were collected at the surface and at 2-3 selected depths (i.e. within and below fluorescence maxima), and Chl-a extraction was performed using a fluorometric method as well as High Performance Liquid Chromatography (HPLC, *Lutz et al.*, 2010; *Carreto et al.*, 2016). Both methodologies showed a significant correlation between Chl-a fluorescence measured by the fluorometer and Chl-a concentration from water samples for all GEF-1 stations. However, *Lutz et al.* (2010) also report that the ratio of Chl-a concentration to fluorescence showed large variability in the vertical and that some stations showed

near-surface photo-inhibition.

For the two hydrographic transects presented in this study, some stations were sampled at noon when Chl-a fluorescence can be affected by non-photochemical quenching, resulting in reduced Chl-a fluorescence at the surface. A linear adjustment of Chl-a fluorescence with Chl-a concentrations extracted from water samples was performed to account for non-photochemical quenching at the surface. Because not all stations had water samples at depth, we used a linear regression based on all available water samples for each cruise. First, voltage counts measured by the fluorometer were converted to Chl-a fluorescence using scale factors provided by SeaPoint Inc. and offset values determined by measuring the sensor output in the dark. The r^2 (e.g. squared correlation coefficient) between Chl-a fluorescence and Chl-a concentration from water samples yields r^2 =0.69 for all GEF-1 samples (n=163), and r^2 =0.61 for GEF-3 (n=113). For both cruises, no consistent overestimation or underestimation by the fluorometer was observed. Chl-a fluorescence was re-calibrated by multiplying by the slope of a Type I linear regression, forced to intercept zero, between Chl-a concentration from water samples (y-axis) and Chl-a fluorescence (x-axis). The correction factor was 1.13 for GEF-1, and 0.9 for GEF-3. A Type II regression, which minimizes the distance perpendicular to the regression line, assuming both variables are subject to measurement errors (see e.g., *Ricker*, 1973), yields qualitatively similar patterns regardless of the method used. Although the magnitude of adjusted Chl-a fluorescence is sensitive to the correction factor, the patterns of Chl-a fluorescence for the three vertical sections analyzed in this study were qualitatively similar. We report adjusted Chl-a fluorescence; however, Chl-a absolute values might not be accurate throughout the water column and should be interpreted with caution.

Because of the coarse horizontal resolution between stations, vertical sections of Chl-a fluorescence were objectively mapped based on the method of *Le Traon* (1990), assuming anisotropic, Gaussian statistics for the eddy field. We used a cross-front length scale of 75 km, based on cross-front autocorrelation of austral spring (Sep-Oct-Nov, SON) satellite Chl-a, and a vertical length scale of 50 m, inferred from the available vertical profiles of adjusted Chl-a fluorescence from GEF-1 and GEF-3 cruises. The data are assumed to have a priori uncorrelated noise, with a noise to signal ratio of 0.25, and interpolated data with error greater than 0.1 were masked.

GEF mooring site

During the October 2005 cruise, a mooring was deployed at the edge of the continental shelf close to the 200-m isobath. The mooring, located at 43.82°S and 59.67°W, measured meteorological and oceanographic data for 51 days, from October 16 to December 5 2005.

The mooring acquired high-resolution measurements of meteorological parameters as well as water column temperature and currents throughout the water column. A surface buoy equipped with meteorological sensors measured wind speed, direction and gustiness, air humidity, temperature and pressure. Wind measurements were sampled every second for 10-minute intervals centered at the hour. Hourly data were recorded internally and 3-hourly data were transmitted to shore via satellite telemetry in near real-time. Our analyses are based on hourly data. Subsurface temperature and conductivity MicroCAT sensors provided hourly measurements at six depth levels: 1m, 10m, 30m, 50m, 75m and 100m depths. Further details on the buoy specifications and these observations are reported by *Valla and Piola* (2015).

Table 4.1: Summary of *in-situ* observations presented in this study (weblinks for data sources can be found in the Data section and Acknowledgements.)

Data type	Location	Time Period	Wind
GEF1 Transect (Rincón)	∼41°S, 57°W	10 Oct 2005	northerly
GEF1 Transect (Valdés)	∼44°S, 60°W	13-15 Oct 2005	southerly
GEF3 Transect (Rincón)	∼41°S, 57°W	23-25 Oct 2006	southerly
GEF Mooring	∼44°S, 60°W	16 Oct - 5 Dec 2006	variable
Historical Hydrography (SHN and INIDEP)	see Fig 7a	1988-1989, 1992-1995, 1997-1998, 2003, 2005, 2006	variable

4.4 Results and Discussion

4.4.1 Composites of satellite Chl-a by wind direction

To investigate the role of along-front winds on Chl-a variability at the SBF, we first looked at composites of satellite Chl-a, segregating the data by wind direction (Fig. 4.3). We use summer data here because in the summer phytoplankton growth is presumed to be nutrient limited, and previous correlation analyses showed wind speed and satellite Chl-a to be correlated in summer in this region (*Carranza and Gille*, 2015), while correlations are weak and non-significant in other seasons. Each satellite Chl-a grid cell was screened for positive (i.e., southerly) or negative (i.e., northerly) along-front winds. Because north of ∼44°S the shelf break does not have a north-south orientation (see Figure 4.1), we rotated winds 35° clockwise north of 44°S and used meridional winds south of that latitude. Mean satellite Chl-a maps for along-front southerly winds, northerly winds and the difference between the two are shown in Figure 4.3.

Over the shelf break, onshore of the 200-m isobath, southerly winds are associated with enhanced satellite Chl-a (red in Figure 4.3c). Further offshore northerly

winds are associated with high Chl-a (blue band offshore of the 200-m isobath in Figure 4.3c). The red band of high Chl-a for southerly winds at the SBF is statistically significant (i.e. the difference is larger than the sum of standard errors for mean Chl-a maps). Offshore of the mean position of the SBF, Chl-a is enhanced with northerly winds, and, although the difference shown in Figure 4.3c is not statistically significant, because Chl-a is generally low, the spatial pattern is coherent along the length of the shelf break. This large-scale pattern emerges when we consider along-front winds, and there is no pattern associated with cross-front winds, implying no clear response of Chl-a to relaxations in along-front winds. Differences are more pronounced if we consider only along-front winds that are larger in magnitude than the cross-front wind component. However, because fewer cases meet these criteria, the statistically significant red band shows less spatial coherence (not shown). The same pattern also arises in correlation maps between anomalies of along-front winds and Chl-a at zero lag (not shown), but we present the composites to ease the interpretation.

The pattern of consistently high Chl-a or low Chl-a to either side of the SBF is more remarkable in the summer than during the other seasons. To better illustrate the cross-front shift in satellite Chl-a with changing along-front wind direction, in Figure 4.4, we compare mean Chl-a for all summer cases (in yellow) against mean Chl-a for southerly winds (red) and northerly winds (blue) for two cross-sections at the SBF, indicated by black dots in Figure 4.3c. Cases of southerly wind are less frequent than cases of northerly wind, because north of 50°S mean summer winds present a northerly component (see Fig. 4.1b), but in both of these transects, the Chl-a peak is shifted onshore of the SBF (i.e., defined here as the peak in the yellow curve) with southerly winds, and the difference between Chl-a for southerly winds and northerly

winds is significant compared with the overall summer mean. This cross-front shift in the location of the Chl-a peak with along-front wind direction suggests the influence of cross-front Ekman transport interacting with the sloping isopycnals at the front. In addition, the Chl-a difference between southerly and northerly wind composites is largest near the SBF and diminishes further away from the SBF (dashed gray curve in Figure 4.4).

Increased Chl-a at the SBF with southerly winds is consistent with the concept that enhanced upwelling at the shelf break occurs when Ekman transport is expected to move near-surface waters onshore (i.e., with southerly winds in the SH) and steepen isopycnals, as proposed by *Siedlecki et al.* (2011). On the other hand, northerly winds associated with high Chl-a offshore of the 200-m isobath may indicate upwelling of nutrients from the BBL, through isopycnal tilting, enhancing phytoplankton growth further offshore. However, satellite observations do not allow us to determine whether the surface signal results from surface advection of high Chl-a from shelf waters by Ekman transport or from isopycnal upwelling that would supply nutrients and enhance growth and/or upwell Chl-a from a subsurface maximum further offshore.

4.4.2 Isopycnal tilting, changes in stratification and *in situ* Chl-a: synoptic evidence

Ship-based hydrographic surveys provide a means to evaluate snapshots of the vertical structure across the shelf break. Several *in situ* hydrographic transects across the SBF were occupied during predominantly along-front wind events. We contrast the southerly and northerly wind cases. In all cases density sections show isopycnal tilting in agreement with induced Ekman transport at the surface, but

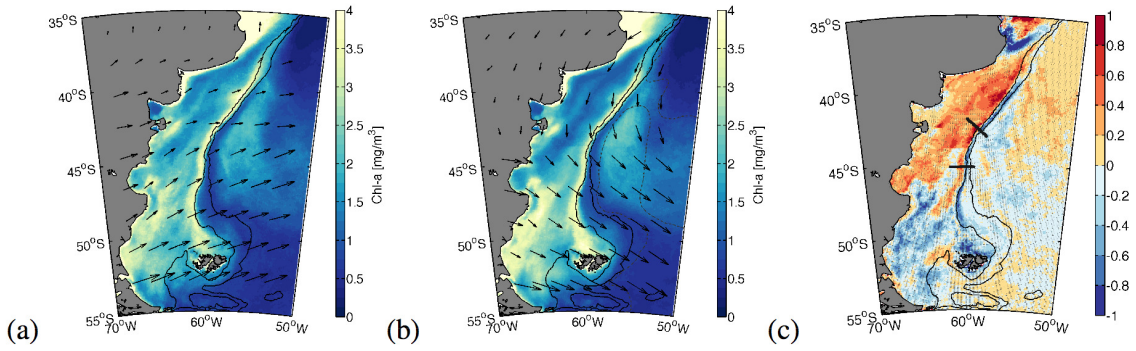

Figure 4.3: Composites of summer Chl-a for (a) southerly winds and (b) northerly winds, based on 4-day averages of CCMP winds for the period 2000-2011. (c) Difference between (a) and (b): red implies Chl-a is enhanced for southerly winds relative to northerly winds, and blue indicates enhanced Chl-a with northerly winds. Winds were rotated 35° clockwise north of 44°S to account for the change in the orientation of the sloping bathymetry. Shaded gray areas in (c) indicate that the difference is not statistically significant (i.e. less than the sum of standard errors for maps (a) and (b).)

because many were sampled in different years and/or in different seasons they are not easily compared. In this section we present two synoptic hydrographic transects across the SBF, off Rincón (at ∼41°S) and Valdés (at ∼44°S), selected because they were occupied during the same cruise, but with opposing wind directions. This allows us to look at isopycnal tilting due to oscillating along-front winds. On October 10 2005, Rincón was sampled during a northerly wind event (Fig. 4.5, a and b), then winds reversed direction and became from the south when Valdés was sampled on October 15 (Fig. 4.5, c and d). Because they were sampled 4-5 days apart in October 2005, and they are only 300 km apart, mean background hydrographic conditions were likely similar. A year later, in September 23-25 2006, Rincón was reoccupied when winds had reversed relative to October 2005, and it was sampled during a southerly wind event (Fig. 4.5, e and f). For all three occupations, the CTD carried a fluorometer from which an estimate of Chl-a concentration can be derived (see Section 4.3.2 for details).

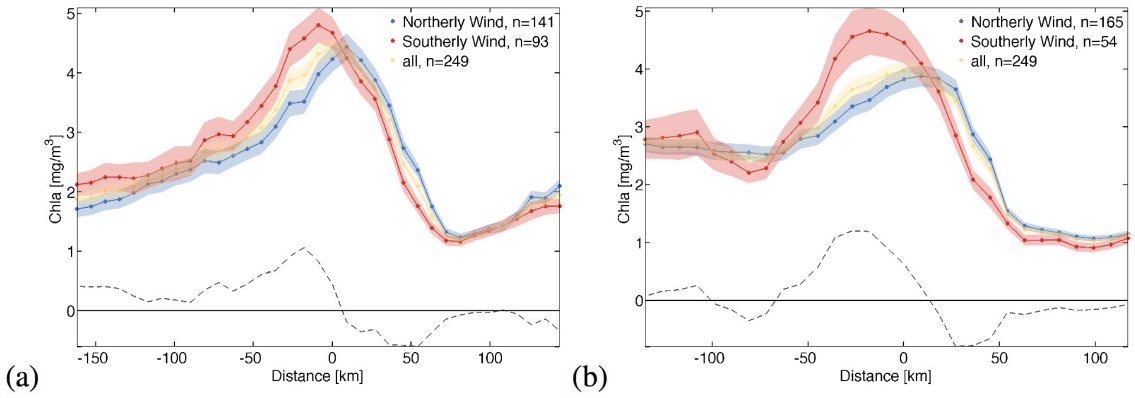

Figure 4.4: Mean summer satellite Chl-a for southerly winds (red), northerly winds (blue) and all summer cases (yellow) for the two transects across the shelf-break front shown in Figure 4.3c, in the (a) northern sector and (b) southern sector. The dashed gray line shows the difference between red and blue lines. The x-axis is the distance from the shelf-break front, defined as the pixel where mean summer Chl-a peaks (maximum in the yellow line).

Mean satellite winds and Chl-a maps, and vertical sections of adjusted Chl-a fluorescence with isopycnals overlaid in white contours for the three occupations are shown in Figure 4.5. For northerly winds (Fig. 4.5, a and b), flattened isopycnals are consistent with surface waters moving offshore in the Ekman layer. For southerly winds (Fig. 4.5, c-f), isopycnals tilt upward, which could result from onshore Ekman transport in the surface layer.

The analysis of water-mass properties for stations at the shelf break for these sections supports this hypothesis (Fig. 4.6). There are pronounced differences in the temperature-salinity (TS) structure at the shelf break stations between sections sampled during northerly-wind and southerly-wind events. Rincón's station at the SBF occupied during northerly winds shows a much warmer, fresher upper layer and a slightly colder, saltier bottom layer (red), than the station at the SBF occupied during a subsequent southerly wind event (light blue). The change in the vertical

thermohaline structure corroborates the offshore flux of warm-fresh shelf water in the upper layer and the compensating onshore flux of cold-salty slope water during the northerly wind event. The reoccupation of Rincón with southerly winds (blue) shows no evidence of shelf waters at the surface and much colder, saltier water at depth. (Although this station was deeper, we only show the upper 150 m to facilitate visual comparison.)

Offshore Ekman transport in the surface layer (i.e., northerly-wind case), flattens the isopycnals, and may imply an onshore flux of nutrient-rich waters from the Malvinas Current at depth (or onwelling). Conversely, onshore Ekman transport (i.e., southerly-wind case), steepening the isopycnal slopes, can potentially pump nutrients from the bottom-boundary layer to the surface enhancing phytoplankton growth and accumulation at the SBF, as suggested by *Siedlecki et al.* (2011). The Chl-a fluorescence signal is consistent with surface Chl-a enhancement further offshore for the case of northerly winds (Fig. 4.5b), suggesting upwelling along the sloping density layers from the bottom to the surface. With southerly winds (Fig. 4.5d and Fig. 4.5e), Chl-a is enhanced at the SBF, consistent with onshore Ekman transport and vertical isopycnals that would enhance upwelling, delivering nutrients to the surface.

To illustrate the spatial extent of the Chl-a signal at the surface, the left panels of Figure 4.5 show satellite Chl-a at the time when the transects were sampled. On October 10 2005, the northern sector of the SBF was cloudy, and satellite Chl-a could not be retrieved; instead we show three-day averaged satellite Chl-a. In the northern sector of the shelf break and during the predominantly northerly wind event, the band of high Chl-a extends offshore of the 200-m isobath (Fig. 4.5a). The enhanced vertical stratification associated with offshore flow of less dense shelf waters and onshore

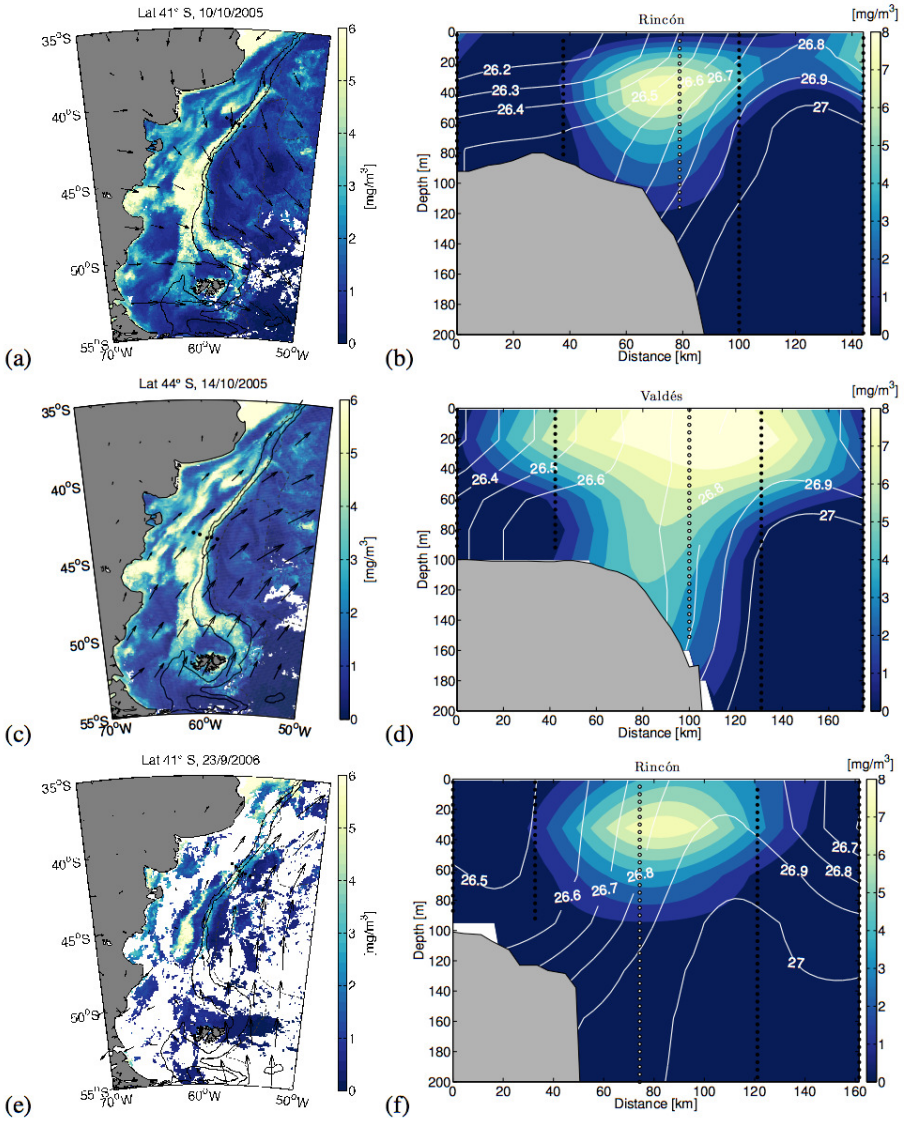

Figure 4.5: Satellite Chl-a and surface winds (left), vertical structure of adjusted Chl-a fluorescence (right, color bar) with density contours overlaid in white, for two transects across the shelf break. The northern transect (Rincón) was sampled on 10 October 2005, when winds were predominantly from the north (a,b). After 4 days, winds reversed direction and the southern transect (Valdés) was sampled on 14 October 2005 (c,d). Rincón, was revisited on 23-25 September 2006 when the winds were from the south (e,f). Vertical sections were objectively mapped (see Section 4.3.2) and values with uncertainty higher than 0.1 are masked. Black dots in the map and vertical sections indicate the location of hydrographic stations. White dots identify stations in the TS diagram of Figure 4.6.

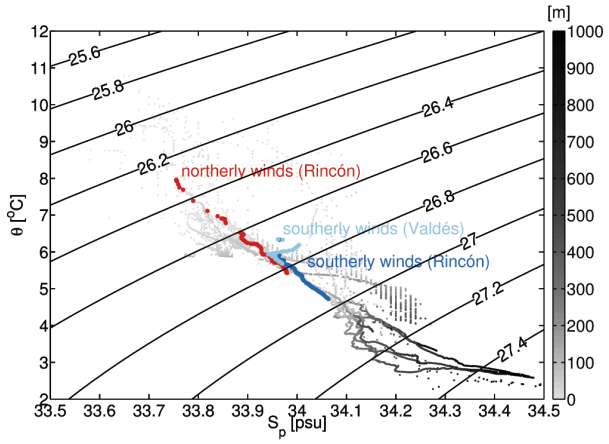

Figure 4.6: Temperature-Salinity (TS) diagram for stations at the shelf break indicated with white dots in vertical sections of Figure 4.5. In red: Rincón station at the SBF sampled with northerly winds on 10 October 2005 (for reference, station 11 from GEF-1), in light blue: Valdés station at the SBF sampled with southerly winds on 14 October 2005 (station 35 from GEF-1), and in blue: Rincón station at the SBF sampled during a southerly wind event on 23-25 September 2006 (station 53 from GEF-3). All stations at the SBF between 39°S and 44°S, deeper than 100 m and shallower than 1500 m, are shown as reference, with the color bar indicating depth.

flow of denser slope waters below the Ekman layer may prevent the upwelled water from reaching the surface at the shelf break. Thus, the highest Chl-a fluorescence is observed below the surface mixed layer (∼22 m). After winds reversed direction, the high band of Chl-a shifts onshore (Fig. 4.5c). This band of high satellite Chl-a is also apparent in the Chl-a anomaly maps relative to the climatological monthly mean for October (not shown). Cloud cover precludes a regional analysis of the surface Chl-a signal in September 2006.

4.4.3 Isopycnal tilting and changes in stratification: statistical significance

Hydrographic transects in Figure 4.5 provide evidence of isopycnal tilting with along-front wind reversals, but they only represent snapshots of water column structure for selected cruises. In this section we present composite hydrographic sections for southerly and northerly winds to assess the statistical significance of isopycnal tilting due to along-front changes in the wind. In Figure 4.7, we show mean austral winter and spring (June-November, JJASON) density sections across the SBF, with stations segregated by wind direction. In summer (DJF), strong stratification develops, the SBF is density-compensated and, therefore, the dynamical response of the front to along-front winds is less remarkable (not shown). Also, winds in the summer tend to be from the north and there are few cases of profiles sampled with southerly winds to evaluate the response of the SBF to changes in along-front winds.

To construct mean hydrographic transects (Fig. 4.7), for each hydrographic station we assigned a wind vector by collocating vertical profiles with satellite rotated winds in space (within 25 km of the satellite grid) and time (within 6 h of the satellite wind estimate). Stations were then segregated by either positive or negative along-front wind component. For comparison with no-wind conditions, for these transects, only cases when the along-front wind component was greater than 2 m s^{-1} were considered for either northerly (N=73 profiles) or southerly winds (N=94). Cases when along-front winds were less than 2 m s^{-1} were flagged as "calm" (i.e., relatively weak along-front winds), and mean density contours for calm conditions (N=67) are overlaid in white for reference in Figure 4.7. Mean density transects across the SBF were computed using *Linder et al.* (2004)'s algorithm, which bins profiles

according to cross-shelf distance from a given isobath to compute mean cross-shelf sections of hydrographic properties in regions of sloping bathymetry. We modified the algorithm to use a version of the General Bathymetric Chart of the Oceans (GEBCO) bathymetry field that has been corrected based on soundings from cruises, gridded at 3-minute resolution (0.05 degrees latitude and longitude). As a reference bathymetry line, for averaging profiles we use the 200-m isobath, which corresponds to the mean position of the SBF off Patagonia.

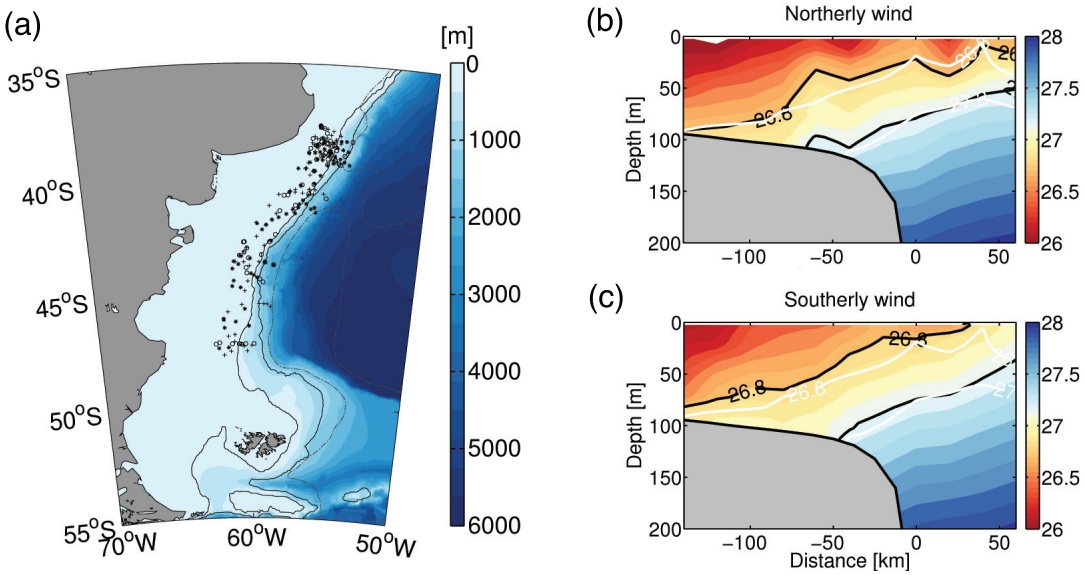

Figure 4.7: Mean hydrographic density sections based on vertical profiles sampled with (a) northerly winds (N=78) and (b) southerly winds (N=94) in winter and spring (JJASON), for stations between 38°S and 50°S. To segregate profiles, here, we used a threshold of 2 m s^{-1} for the intensity of along-front winds. Cases when the along-front wind component was less than 2 m s^{-1} were considered "calm", although stronger cross-front winds could occur in these cases. Mean density contours for calm conditions (N=67) are overlaid in white.

The mean density section for stations sampled with southerly winds (Fig. 4.7a) shows surfacing isopycnals tilted upward relative to the mean density section for stations sampled with northerly winds (Fig. 4.7b). The surfacing of isopycnals for northerly winds occurs further offshore than for southerly winds (Fig. 4.7), although

the foot of the front, defined here as the grounding of the isopycnals between 26.8 and 27.2 kg m^{-3}, does not show substantial displacement. For example, the outcrop of isopycnal 26.8 that occurs near the 200-m isobath with southerly winds, occurs ∼50 km offshore with northerly winds. The migration of the foot of the front is difficult to assess because of inhomogenities of the bathymetry along the 200-m isobath and the averaging procedure. In addition, the foot of the front is expected to lag changes in the winds by a few days (*Siedlecki et al.*, 2011). Nonetheless, the surface expression of the sloping isopycnals with changing along-front winds is a robust feature that shows in mean density sections for winter and spring.

Ekman transport can displace waters to either side of the front, modifying the stratification of the surface layer either by destratifying (i.e. with southerly winds) or restratifying (i.e. with northerly winds). As a measure of stratification, we computed the vertical density gradient between 100 m and the surface for stations within 50 km of the 200-m isobath. The vertical density gradient vs along-front wind component is shown in Figure 4.8, for stations in the latitude range between 38°S and 44°S. We find a negative correlation between stratification and the along-front component of the wind in agreement with theory: northerly winds (i.e.,V <0) typically result in more stratified waters in the upper 100 m, whereas southerly winds (i.e.,V >0) are associated with lower stratification. Although the correlation is low (r=-0.48, based on N=97), it is statistically significant at the 99% level. Selecting a smaller latitudinal range yields higher significant correlations (with N >50), and r varies between -0.3 and -0.7 with lower correlations south of 45°S, where bathymetric contours spread out and stratification is generally low due to large tidal amplitudes (*Combes and Matano*, 2014).

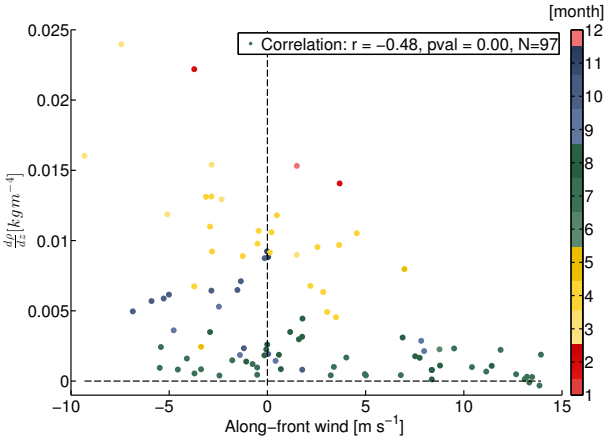

Figure 4.8: Scatter plot for the density gradient between 100m and the surface vs the along-front wind component, for stations between 38°S and 44°S. The correlation for the 97 stations at the SBF with CCMP wind data is -0.48, significant at the 99% level. The color bar shows the month of the year.

4.4.4 Water-column response to along-front winds

The mooring deployed at the shelf break in the location indicated in Figure 4.9a allows us to assess the water-column temperature response to oscillating meridional winds. The wind record shows several periods of oscillating meridional winds that are correlated with water temperature. The timeseries of meridional winds and surface water temperature anomalies (i.e., subtracting a linear trend) are shown in Figure 4.9. Following a period of southerly winds (i.e., positive meridional winds), temperature decreases.

The water-column temperature, salinity and density structure also show a much more homogeneous water column after southerly winds (blue in Fig. 4.10), in contrast to a more stratified water column after a period of northerly winds (red in Fig. 4.10). To illustrate this, in Figure 4.10 we show mean profiles estimated during 24-h periods following persistent wind events that lasted more than 1.5 days. This criterion results in 2 southerly wind events and 5 northerly wind events for the 51-day

record. Selecting wind events with a minimum duration of 1 day results in a larger number of events (4 southerly wind events and 8 northerly wind events) and shows a qualitatively similar structure (not shown), but differences are more pronounced when considering wind events that lasted more than 1.5 days. The longest southerly wind event in the record lasted more than 3 days (73 hours), in late October 2005. Mean temperature, salinity and density profiles for the last day of that event (i.e., on 29-30 October 2005) show no traces of shelf waters at the surface (e.g. $S_p > 33.8$ psu over the entire water column), and a thoroughly mixed water column in the top 100 m (not shown). Differences in surface density between northerly and southerly wind events are on average 0.25 kg m^{-3} but are larger than 0.4 kg m^{-3} for the events of longest duration (i.e., the above mentioned southerly wind event, and a northerly wind event that ended on 11 November 2005 and lasted 3.6 days).

Lagged cross-correlations between meridional winds and water column temperature anomalies at the six depth levels show a coherent signal in the upper 100 m (Fig. 4.11). For clarity, in Figure 4.11, we only show lagged cross-correlations with temperature at 1 m, at 50 m and at 100 m depths.

Cross correlations show that temperature responds to changes in the winds with a lag of ∼3-4 days, consistent with the Ekman spin-up time characteristic of the spring (i.e. $T_{Ek} = (\frac{K_z}{fd^2})^{-\frac{1}{2}} \times f^{-1}$ ∼2.4-4.8 days with d ∼20-40 m and K_z ∼10^{-4} m^2 s^{-1}). Positive lags imply that wind leads changes in temperature, and the negative correlation for the first significant peak is consistent with southerly winds associated with cold temperatures at the front, which is consistent with local upwelling. Ekman spin-up time is sensitive to the criterion used to identify mixed-layer depth and can vary between 2.4-12 days for mixed layers shallower than 100 m, assuming a mean

vertical diffusivity, $K_z \sim 10^{-4}$ m^2 s^{-1}. Mixed-layer depth estimates from the mooring record give a mean value of 33 m, using temperature and density threshold criteria from *de Boyer Montégut et al.* (2004), with a standard deviation of 9 m. Assuming d =30 m and $K_z = 10^{-4}$ m^2 s^{-1}, the Ekman spin-up time is 3.6 days. Larger diffusivities (i.e., $K_z > 10^{-4}$ m^2 s^{-1}) may be expected at frontal regions (e.g. see *Zhang et al.* (2013) for an estimate at the MAB shelf-break front). To our knowledge, there are no microstructure measurements or observational estimates of diffusivities in the region that can provide a better estimate of K_z. Note, however, that T_{Ek} is more sensitive to mixed-layer depth than to K_z, since T_{Ek} is proportional to d and to $\frac{1}{\sqrt{(K_z)}}$. A factor of 4 change in d will yield a factor of 4 change in T_{Ek}, but a factor of 4 change in K_z, will only change T_{Ek} by a factor of 2. Mean vertical diffusivities are also influenced by episodic winds. Strong wind events may lead to larger K_z values and a smaller Ekman spin-up time, but as K_z increases, d is expected to increase as well, partially compensating the associated error in our estimate of T_{Ek}.

A 7-8 day periodicity in the lagged-cross correlations is also noteworthy. However, frequency spectra for 6-hour CCMP wind time series from 1987-2011 at the mooring location do not show a significant peak of energy at that frequency (not shown), indicating that the recurrence of the oscillating meridional winds observed during the time period when the mooring was measuring is not typical for this region and/or time of the year. Wind reversals at 4-5 day intervals seem to dominate during part of the record, 25 Oct - 15 Nov, but before and after this time period the wind appears to reverse at shorter time scales (Fig. 4.9). Nonetheless, power spectral estimates show an increase of $\sim 20\%$ in spectral energy for meridional winds (relative to zonal winds) in the frequency range for periods between 2-10 days, which coincides

with periods for atmospheric synoptic scale fluctuations in the Southern Hemisphere (e.g. *Vera*, 2003).

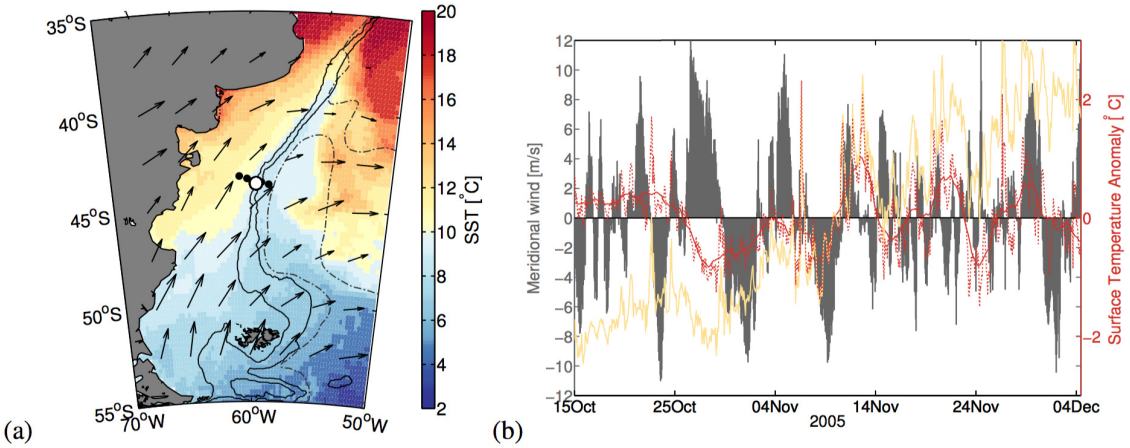

Figure 4.9: (a) Mean sea surface temperature (color bar) with wind vectors overlaid for the period October 16 to December 5 2005, when the mooring site at $\sim$ 44°S indicated by the white dot acquired hourly winds and water column temperature at six depth levels from the surface to 100 m (bottom depth at 185 m). (b) Time series of meridional winds (gray) and detrended sea surface temperature anomalies (red) at the mooring site indicated in (a). Positive meridional winds indicate southerly winds, and negative meridional winds indicate northerly winds. The yellow line shows the raw sea surface temperature time series at 1m. For correlation statistics between along-front winds and temperature see Fig. 4.11

4.5 Further Discussion

We have shown evidence for wind modulation of upwelling and Chl-a concentrations at the SBF off Patagonia from a diverse set of observations that include satellite observations and *in situ* measurements. The wind modulation at the SBF is associated with the along-front component of the winds, and it is consistent with the theory of enhanced shelf-break upwelling and the nutrient pumping mechanism postulated by *Siedlecki et al.* (2011). We find that southerly winds (i.e., down-front)

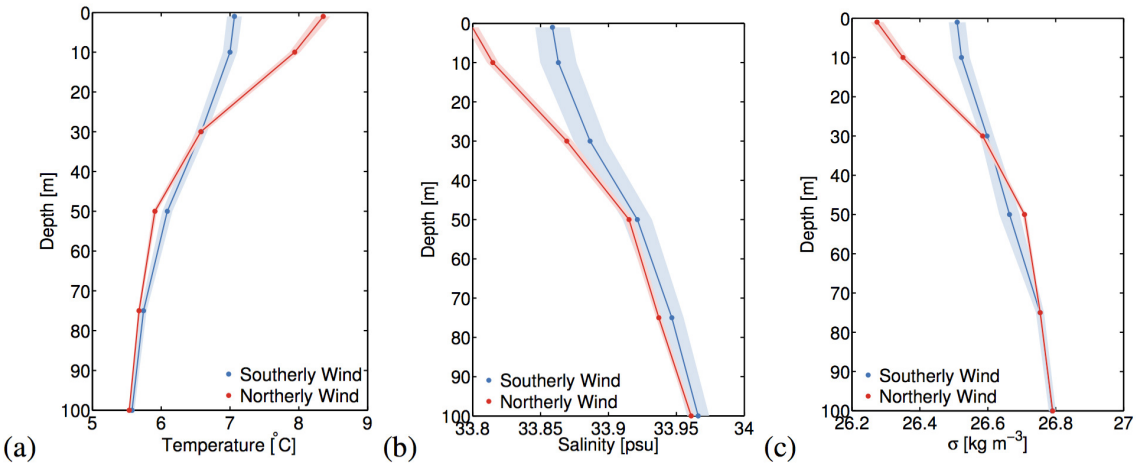

Figure 4.10: Mean (a) temperature, (b) salinity and (c) density profiles at the mooring location(bottom depth at 185 m), averaged over a 24-h period at the end of southerly wind events (in blue), and northerly wind events (in red). A southerly/northerly wind event was considered when positive/negative meridional winds persisted for more than 1.5 days, resulting in 2 southerly wind events (N=48), and 5 northerly wind events (N=120).

enhance satellite Chl-a at the SBF off Patagonia, destratify the water column and tilt isopycnals upward, possibly allowing for enhanced nutrient supply to the euphotic zone. Conversely, northerly winds are associated with enhanced stratification and flatter isopycnals, preventing nutrients and/or a subsurface Chl-a maxima from reaching the surface at the SBF but enhancing surface Chl-a further offshore. Some results pointing in this direction deserve further discussion.

The amplitude modulation of the satellite Chl-a signal by along-front winds is $< \pm 1$ mg m^{-3} (Fig. 4.3c), but the magnitude is likely underestimated for several reasons. Our satellite-based results pertain to summer, and the amplitude modulation of satellite Chl-a by along-front winds is incipient in the spring (not shown). Although stratification in summer may prevent the movement of the foot of the front and inhibit the nutrient pumping effect (*Siedlecki et al.*, 2011), factors other than nutrient limitation (e.g. light limitation, zooplankton grazing) may influence phytoplankton growth

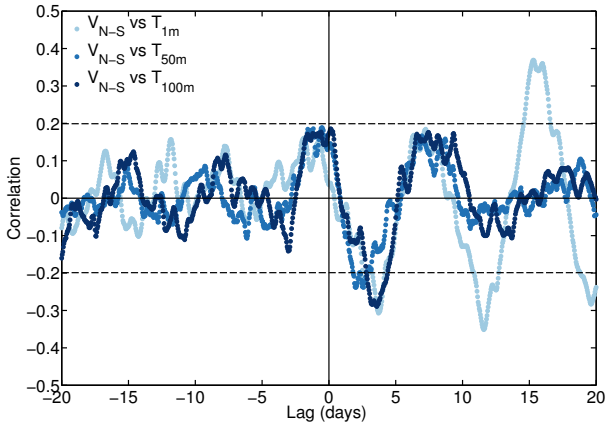

Figure 4.11: Lagged cross correlations between meridional winds and temperature (a) at the surface, (b) at 50 m, and (c) 100 m. Positive lags indicate wind is leading with respect to changes in water temperature. A negative correlation for the first significant peak implies southerly winds are associated with cold temperatures. The 95% confidence interval for significant correlations (indicated by the dashed black line) was computed for the time series subsampled every 12h (N_{eff}=101), such that temperature and meridional wind time series were uncorrelated.

and/or accumulation at the surface and explain the seasonal differences in the Chl-a response. In either season, an oscillation in along-front winds is required to pump water effectively from the near-bottom layer and the ocean interior to the ocean surface, and our satellite results based on Chl-a composites, can include northerly and southerly wind events that were not necessarily followed by a subsequent wind reversal persistent enough to allow time for the pumping mechanism to take place. Nonetheless, we are able to retrieve a signal from composites of satellite Chl-a from all cases of northerly vs southerly winds. The effect of subsequent along-front wind reversals in the water-column vertical structure, cross-front density structure, and Chl-a fluorescence signal is depicted by the two synoptic transects sampled during GEF-1 cruise (Fig. 4.5) as well as by the observations at the mooring site (Fig. 4.10 and Fig.4.11). For persistent wind events followed by persistent wind reversals, the amplitude modulation of the Chl-a signal is expected to be larger, e.g. differences in

surface Chl-a fluorescence can be greater than 5 mg m^{-3} (Fig. 4.5b and Fig. 4.5d). The Chl-a amplitude modulation due to along-front oscillating winds is significant compared to the $\sim$4 mg m^{-3} for the annual amplitude (Fig. 4.1b). Moreover, subsurface phytoplankton blooms deeper than one optical depth, that can occur particularly in summer (see e.g. *Hales et al.*, 2009), will be missed by the satellite (e.g. *Morel and Berthon*, 1989) when upwelling along the front could still be happening.

The cross-front horizontal displacement of the satellite Chl-a peak due to changing wind conditions is relatively small (i.e. $\sim$25-50 km), but large enough to be detectable from satellite observations and coarse resolution hydrographic transects. An offshore displacement of the high satellite Chl-a band at the SBF, relative to the 200-m isobath, from early spring to late summer, was reported by *Romero et al.* (2006), which could be related to the increased frequency of northerly wind events (and associated offshore Ekman transport) during the summer season.

The Chl-a response to alongshore winds might appear to conflict with results reported by *Saraceno et al.* (2005), who found that strong northerly winds lead to higher Chl-a in the northern part of the shelf and SBF, where our Fig. 4.3c shows red, implying higher Chl-a with southerly winds. However, their analysis focused on seasonal to inter-annual timescales, and by low-pass filtering, they suppressed the high-frequency wind variability that is the focus of this study. The differing correlation patterns suggest that different mechanisms operate on synoptic vs longer timescales.

Valla and Piola (2015) also carried out an independent assessment based on surface currents and temperature observations from another mooring at the SBF off Patagonia. Their results agree with ours in showing that high-frequency variabil-

ity (i.e., sub-seasonal) surface cooling events, linked to intense upwelling, lead to a significant increase in surface Chl-a at the SBF. Although their analysis does not include the effect of directional wind forcing, the intense cooling event they reported in January 2007, was coincident with southerly synoptic winds over the shelf break (their Fig. 13). They also reported onshore surface velocities prior to the cooling period and offshore velocities near its termination ($\sim$13-15 cm s^{-1}). Although the magnitude of the upwelling inferred from that event is in agreement with predictions from numerical experiments with realistic boundary conditions and forcing (*Combes and Matano*, 2014), as *Valla and Piola* (2015) pointed out, the timescales over which the cooling events occur in the model and observations do not agree (i.e., $\sim$180 days vs $\sim$5 days, respectively). Numerical simulations from *Combes and Matano* (2014) also suggested that the upwelling at the SBF off Patagonia is not sensitive to changes in local wind forcing, but these experiments were forced with monthly climatological mean winds that did not resolve the atmospheric synoptic activity. The timescales and duration of the cooling events reported by *Valla and Piola* (2015) (i.e., 3-18 days) are in closer agreement with wind-driven upwelling by along-front wind variability.

Wind-induced upwelling in the vicinity of a jet may also be caused by along-front wind stress (wind−surface current) variations in the cross-front direction itself (*Dewar and Flierl*, 1987; *Zhang et al.*, 2013). Assuming uniform winds that are stronger in magnitude than the surface current jet, the differential wind stress (i.e., wind-stress curl) to either side of the front can produce Ekman transport divergences and upwelling through Ekman pumping. Such mechanism would lead to upwelling onshore of the SBF, regardless of wind orientation: for southerly winds the effective stress is minimum at the core of the jet leading to smaller Ekman transport onshore

relative to either side of the jet, while for northerly winds, a maximum wind stress at the jet core would lead to greater offshore Ekman transport at the jet. In both cases, this results in surface divergence and upwelling onshore of the Malvinas Current jet. However, our results suggest that onshore of the Patagonian SBF, upwelling is enhanced with southerly winds but suppressed with northerly winds. This is likely due to the fact that in this region winds are generally much stronger than surface currents, thus the impact of the surface currents on the effective stress is minimal.

While changes in wind speed can lead to changes in vertical mixing, regardless of the direction of the wind, and thus can have an impact on Chl-a accumulation (e.g. *Carranza and Gille*, 2015), in this region the enhancement of Chl-a at the SBF differs depending on wind direction, and thus wind-speed-induced vertical mixing does not appear to be a dominant mechanism. The lack of correlation with cross-front or zonal winds at the SBF (not shown), further supports *Siedlecki et al.*'s [2011] theory, indicating that atmospheric synoptic storms, which are associated with fluctuations in meridional winds with periods between 2-10 days (e.g. *Vera*, 2003), can significantly enhance upwelling at the SBF off Patagonia, and also potentially at other shelf-break fronts of western boundary currents. For example, the modification of the density structure due to along-front wind oscillations in the synoptic band, was identified in observations from the New England SBF sector of the MAB (*Aikman et al.*, 1988; *Houghton et al.*, 1988; *Fratantoni*, 2003). However, despite persistent upwelling revealed from observations in the MAB, there is no persistent Chl-a enhancement at the SBF, possibly due to zooplankton grazing (*Zhang et al.*, 2013); baroclinic instabilities of the jet cause significant current variability (*Fratantoni*, 2003). The mechanism proposed by *Siedlecki et al.* (2011), who neglected along-shelf pressure gradients, may

be applicable in the Patagonian shelf, due to the barotropic nature and stability of the Malvinas Current (*Vivier and Provost*, 1999; *Piola et al.*, 2013), the relative low meandering and eddy kinetic energy observed (*Goni et al.*, 2011; *Artana et al.*, 2016), and the predominantly meridional orientation of the bathymetry.

Nutrient distributions for the synoptic transects presented in this study are reported by *Carreto et al.* (2016, their Fig. 5), who show higher nutrient concentrations at the SBF for the southerly wind case (i.e. Valdés, see Fig. 4.5c and d) compared with the northerly wind case (i.e. Rincón, see Fig. 4.5a and b), in agreement with the results presented here. Due to the lack of concomitant observations of nutrients, vertical diffusivities and/or vertical velocities, it is not possible to do a meaningful assessment of the upwelled nutrient fluxes associated with the along-front wind induced upwelling (e.g. *He et al.*, 2011). Although the existing nutrient data combined with the approach in *Valla and Piola* (2015) to estimate vertical velocities from the mooring site may prove useful for an estimate of the upwelled flux of nutrients, quantifying the role of this mechanism is out of the scope of this study but will be the focus of future work.

4.6 Conclusions

This work has demonstrated that wind forcing on sub-seasonal timescales is important for shelf-break exchange, and can lead to enhanced upwelling and Chl-a concentrations at shelf-break fronts of western boundary currents. We presented observational evidence that wind modulates the upwelling at the shelf-break front off Patagonia, consistent with a mechanism for nutrient pumping associated with along-front wind oscillations that was proposed by *Siedlecki et al.* (2011) based on a numer-

ical model. Composites of satellite Chl-a segregated by wind direction, hydrographic transects with Chl-a fluorescence across the shelf-break front sampled with opposing wind direction, and a mooring site that collected high-resolution wind and hydrographic data throughout the water column suggest that oscillations in along-front winds can modulate the vertical stratification and the upwelling at the shelf-break front off Patagonia, with biological implications. Atmospheric synoptic scale storms, characterized by fluctuations in meridional winds with periods between 2-10 days, can potentially induce shelf-break upwelling at other shelf-break fronts of western margins of ocean basins.

For the 1500-km long Patagonian SBF extending roughly meridionaly, the theory predicts that southerly winds (down-front), lead to Ekman transport onshore in the surface layer and tilt isopycnals upward, destratifying the water column and allowing upwelling of nutrients from deeper layers. Conversely, northerly winds (upfront) lead to offshore Ekman transport, flatten isopycnals, stratify the water column at the front and prevent nutrients and/or Chl-a from a subsurface maximum from reaching the surface. In agreement with theory, satellite observations show that surface Chl-a is enhanced at the SBF (i.e. onshore of the 200-m isobath) with southerly winds, and suppressed with northerly winds when surface Chl-a is enhanced further offshore (i.e $\sim$25-50 km). The Chl-a amplitude modulation by along front-winds inferred from satellite observations (in summer) is $\sim$25% of the mean annual Chl-a amplitude for the 12-year satellite record. Hydrographic transects from synoptic surveys as well as mean density sections from historical observations segregated by along-front wind direction, are also consistent with the theory. However, the Chl-a fluorescence difference between subsequent changes in along-front wind direction can be significantly

larger in the spring ($\pm$ 5 mg m^{-3}), compared to the summer estimate from satellite observations. Nutrient distributions for the synoptic transects presented in this study are in accord with the theory (see *Carreto et al.*, 2016). High resolution (i.e., hourly) wind and water column hydrographic time series collected in spring at the mooring site provide further evidence and show that southerly winds destratify the water column leading to cooling events, whereas northerly winds restratify the upper ocean and lead to warming events. Most importantly, the timescale for the water column response to changes in along-front winds inferred from the mooring site (i.e., 3-4 days) is consistent with estimates of Ekman spin-up time characteristic of the spring.

Recognizing the limitations of the existing observations at the SBF of Patagonia, we focused on presenting robust patterns of variability that indicate along-front wind-induced upwelling through the Chl-a response, without putting much emphasis on a quantitative assessment. A meaningful quantification of the upwelled nutrient fluxes, associated with the upwelling induced by along-front wind oscillations, will require concomitant observations of nutrient concentrations, vertical diffusivities and velocities for the three wind scenarios (i.e. northerly, southerly and calm conditions), and this can only be obtained from a high-resolution survey designed for that purpose.

4.7 Acknowledgments

We greatly acknowledge SHN and INIDEP from Argentina for collecting and providing all the *in situ* observations in the region, available from *Charo and Piola* (2014) and at http://www.inidep.edu.ar/oceanografia. Chris Linder for facilitating the MATLAB code to compute cross-front mean transects (available at http://www.

whoi.edu/science/PO/people/clinder/software.html. James Pringle for useful discussions, and two anonymous reviewers who contributed to improve this manuscript. Mati Kahru for processing and providing the satellite Chl-a data. NASAs Research, Education and Applications Solution Network (REASoN) and MEaSURES programs funded development of the CCMP wind fields, which are distributed by the Physical Oceanography Distributed Active Archive Center (http://podaac.jpl.nasa. gov/). MMC and STG were funded by a NASA NESFF fellowship (NNX12AN41H 001), NASA's Ocean Vector Wind Science Team (NASA NNX14A078G) and the Southern Ocean Carbon and Climate Observations and Modeling (SOCCOM) Project (NSF PLR-1425989). ARP acknowledges the support of grant CRN3070 from the Inter-American Institute for Global Change Research, which is supported by the US National Science Foundation grant GEO-1128040. SIR acknowledges the support of grant PIDDEF 47/12 from the Argentine Ministry of Defense.

Chapter 4, in full, has been submitted for publication of the material as it may appear in *Journal of Geophysical Research Oceans*: **Carranza M. M.**, Gille S. T., Piola A. R., Charo M. and Romero S. I. (2016). Wind modulation of the upwelling at the shelf-break front off Patagonia: Observational evidence, *J. Geophys. Res. Oceans*. The dissertation author was the primary investigator and author on this paper.

Chapter 5

Conclusions and future perspectives

In this thesis I have investigated the impact of synoptic-scale atmospheric forcing (i.e. winds and surface heat fluxes) on Southern Ocean Chl-a variability, which was used as a proxy for phytoplankton biomass to look at patterns of variability in relation to physical processes.

While the paradigm for Southern Ocean phytoplankton bloom development is that deep mixed layers (and presumably deep mixing) tend to reduce mean light levels preventing phytoplankton growth and/or accumulation within mixed layers, results from Chapter 2 suggest that wind-driven entrainment through mixed layer deepening can enhance phytoplankton growth in summer, as higher nutrient concentration waters from below the mixed layers are entrained into the surface layer (where Fe has presumably become depleted). However, although high winds can potentially entrain higher nutrient concentrations from below the mixed layer to the surface in a few hours or in less than a day (e.g. *Klein and Coste*, 1984; *Eppley and Renger*,

1988; *Marra et al.*, 1990), incubation experiments in water samples from the Southern Ocean indicate phytoplankton growth occurs >3-4 days after Fe addition (e.g. *de Baar et al.*, 2005). Further analyses of lagged correlations between wind speed and satellite Chl-a also indicate correlations are maximal at zero-lag time (from daily data) and vanish at 3-day lags (not shown), thus, suggesting that wind-driven entrainment of Fe impacting growth rates is unlikely at daily scales.

Subsurface Chl-a fluorescence data from floats and southern-elephant seal tags analyzed in Chapter 3 reveal that, even in the Southern Ocean, deep Chl-a fluorescence maxima are frequent in summer, but may also occur in other seasons. The higher frequency of occurrence of deep Chl-a fluorescence maxima in summer, that are found more often close to the base of the mixed layer, together with the fact that correlations between winds and satellite Chl-a are largest at zero lag time suggest wind-driven entrainment likely enhances surface Chl-a concentrations by eroding deep Chl-a maxima rather than impacting phytoplankton growth.

Chl-a fluorescence vertical profiles exhibit deep maxima, gradients and significant variance within homogeneous layers in density, confirming mixed layers in hydrographic properties are different from mixing layers (where active turbulence is expected to homogenize tracers), and suggesting intermittent levels of turbulence within hydrographically defined mixed layers are not uncommon. The presence of Chl-a fluorescence gradients and consistently higher variability (relative to potential density) within hydrographic mixed layers suggests the timescales of photo-adaptation to light are shorter than the mixing timescales. This suggests that, despite expected stormy weather year round in the Southern Ocean, periods of quiescence between storms are long enough to allow for phytoplankton photo-adaptation (and thus, Chl-

a fluorescence gradients to form) within hydrographic mixed layers.

Estimates of vertical mixing in the surface mixed layer from direct measurements are difficult to obtain (*Brainerd and Gregg*, 1995) and/or rely on methods or parameterizations that fail in regions of strong pycnoclines or weak stratification (e.g. *Gregg et al.*, 2003; *Osborn*, 1980; *Thorpe*, 1977), and are usually valid below the base of the mixed layer. There is, however, potential for the use of bio-optical measurements as photo-adaptive properties to quantitatively estimate turbulence within mixed layers and infer mixing rates (*Falkowski*, 1983; *Lewis et al.*, 1984b; *Therriault et al.*, 1990). The use of photo-adaptive properties to infer mixing rates requires comparable timescales of mixing and photo-adaptation (*Lewis et al.*, 1984a; *Dusenberry*, 2000), and in my future research, I will pursue quantifying the ratio between these timescales to assess mixing rates within mixed layers from the new generation of Argo floats (i.e., biogeochemical Argo floats). On atmospheric-synoptic scales, high winds influence satellite Chl-a variability suggesting an impact on phytoplankton blooms. As new subsurface data from bio-optical sensors become available in the Southern Ocean and fill data gaps under cloudy conditions, not only at the surface but through the water column, an interesting experiment (leveraging the combination of satellite winds and biogeochemical Argo float data) would be to address the impact of individual atmospheric synoptic storms (and/or anticyclonic systems, presumably associated with periods of quiescence) on phytoplankton bloom development in a Lagrangian sense (i.e., following a synoptic system).

This thesis work emphasizes that knowledge of characteristic timescales and spatial scales of variability of physical and biological processes are key to understanding the coupling/uncoupling between physics and biology. The Ocean Observatories

Initiative (OOI) is providing unprecedented high-resolution time series of biogeochemical and physical properties at two sites in the Southern Ocean (i.e., in the southeast Pacific and Argentine basin), allowing for a detail assessment of decorrelation scales and characteristic timescales of variability of physical and biogeochemical parameters that can enlighten bio-physical interactions on atmospheric-synoptic scales in the Southern Ocean.

The significant influence of directional wind forcing on the upwelling at the shelf-break front off Patagonia, investigated in Chapter 4 through the Chl-a response, contributes to our understanding of shelf-slope exchange processes. A meaningful quantification of the upwelled nutrient fluxes, associated to the upwelling induced by along-front wind oscillations, will require concomitant observations of nutrient concentrations, vertical diffusivities and velocities for the three wind scenarios (i.e. northerly, southerly and calm conditions) that are only possible to obtain from a high-resolution survey designed for that purpose. The outcome of this study can motivate and help guide future field experiments aimed at quantifying the role of wind-induced upwelling by along-front winds in the region, as well as its relative importance with the upwelling induced by BBL detachment or divergences of the Malvinas Current.

Bibliography

Abraham, E. R. (1998), The generation of plankton patchiness by turbulent stirring, *Nature*, *391*(6), 577–580.

Acha, E., H. Mianzan, R. Guerrero, M. Favero, and J. Bava (2004), Marine fronts at the continental shelves of austral South America: Physical and ecological processes, *Journal of Marine Systems*, *44*(1-2), 83–105.

Aikman, F., H. W. OU, and R. W. Houghton (1988), Current Variability Across the New-England Continental Shelf-Break and Slope, *Continental Shelf Research*, *8*(5-7), 625–651.

Alexander, M., A. Capotondi, A. Miller, F. Chai, R. Brodeur, and C. Deser (2008), Decadal variability in the northeast Pacific in a physical-ecosystem model: Role of mixed layer depth and trophic interactions, *Journal of Geophysical Research*, *113*, C02017, doi:10.1029/2007JC004359.

Alexander, M. A., J. D. Scott, and C. Deser (2000), Processes that influence sea surface temperature and ocean mixed layer depth variability in a coupled model, *Journal of Geophysical Research*, *105*(C7), 16,823–16,842.

Allison, D. B., D. Stramski, and B. G. Mitchell (2010), Seasonal and interannual variability of particulate organic carbon within the Southern Ocean from satellite ocean color observations, *Journal of Geophysical Research*, *115*, C06002, doi:10.1029/2009JC005347.

Arrigo, K. R., A. Weiss, and W. Smith Jr (1998), Physical forcing of phytoplankton dynamics in the southwestern Ross Sea, *Journal of Geophysical Research*, *103*(C1), 1007–1021.

Arrigo, K. R., G. L. Van Dijken, and S. Bushinsky (2008), Primary production in the Southern Ocean, 1997–2006, *Journal of Geophysical Research*, *113*, C08004, doi:10.1029/2007JC004551.

Arruda, R., P. H. R. Calil, A. A. Bianchi, S. C. Doney, N. Gruber, I. Lima, and G. Turi (2015), Air-sea CO_2 fluxes and the controls on ocean surface $\underline{p}CO_2$ seasonal variability in the coastal and open-ocean southwestern Atlantic Ocean: a modeling study, *Biogeosciences*, *12*(19), 5793–5809.

Artana, C., R. Ferrari, Z. Koenig, M. Saraceno, A. R. Piola, and C. Provost (2016), Malvinas Current variability from Argo floats and satellite altimetry, *Journal of Geophysical Research: Oceans*.

Atlas, R., R. N. Hoffman, J. Ardizzone, S. M. Leidner, J. C. Jusem, D. K. Smith, and D. Gombos (2011a), A Cross-calibrated, Multiplatform Ocean Surface Wind Velocity Product for Meteorological and Oceanographic Applications, *Bulletin of the American Meteorological Society*, *92*(2), 157–174.

Atlas, R., R. N. Hoffman, J. Ardizzone, S. M. Leidner, J. C. Jusem, D. K. Smith, and D. Gombos (2011b), A Cross-calibrated, Multiplatform Ocean Surface Wind Velocity Product for Meteorological and Oceanographic Applications, *Bulletin of the American Meteorological Society*, *92*(2), 157–174, doi:10.1175/2010BAMS2946.2.

Babanin, A. V., A. Ganopolski, and W. R. C. Phillips (2009), Wave-induced upper-ocean mixing in a climate model of intermediate complexity, *Ocean Modelling*, *29*(3), 189–197.

Bailleul, F., C. Cotté, and C. Guinet (2010), Mesoscale eddies as foraging area of a deep-diving predator, the southern elephant seal, *Marine Ecology Progress Series*, *408*, 251–264, doi:10.3354/meps08560.

Baker, A. R., and P. Croot (2010), Atmospheric and marine controls on aerosol iron solubility in seawater, *Marine Chemistry*, *120*(1), 4–13.

Baldwin, M. P. (2001), Annular modes in global daily surface pressure, *Geophysical Research Letters*, *28*(21), 4115–4118.

Behrenfeld, M., E. Boss, D. Siegel, and D. Shea (2005), Carbon-based ocean productivity and phytoplankton physiology from space, *Global Biogeochemical Cycles*, *19*, GB1006, doi:10.1029/2004GB002299.

Behrenfeld, M., K. H. Halsey, and A. J. Milligan (2008), Evolved physiological responses of phytoplankton to their integrated growth environment, *Philosophical Transactions of the Royal Society B: Biological Sciences*, *363*, 2687–2703.

Behrenfeld, M. J. (2010), Abandoning Sverdrup's critical depth hypothesis on phytoplankton blooms, *Ecology*, *91*(4), 977–989.

Behrenfeld, M. J., and E. Boss (2003), The beam attenuation to chlorophyll ratio: an optical index of phytoplankton physiology in the surface ocean?, *Deep Sea Research Part I: Oceanographic Research Papers*, *50*(12), 1537–1549, doi:10.1016/j.dsr.2003.09.002.

Behrenfeld, M. J., R. T. O'malley, D. A. Siegel, C. R. Mcclain, J. L. Sarmiento, G. C. Feldman, A. J. Milligan, P. G. Falkowski, R. M. Letelier, and E. S. Boss (2006), Climate-driven trends in contemporary ocean productivity, *Nature*, *444*, 752–755.

Belcher, S. E., A. L. M. Grant, K. E. Hanley, B. Fox-Kemper, L. Van Roekel, P. P. Sullivan, W. G. Large, A. Brown, A. Hines, D. Calvert, A. Rutgersson, H. Pettersson, J.-R. Bidlot, P. A. E. M. Janssen, and J. A. Polton (2012), A global perspective on Langmuir turbulence in the ocean surface boundary layer, *Geophysical Research Letters*, *39*, L18605, doi:10.1029/2012GL052932.

Bianchi, A. A. (2005), Vertical stratification and air-sea CO 2fluxes in the Patagonian shelf, *Journal of Geophysical Research*, *110*(C7), doi:10.1029/2004JC002488.

Bianchi, A. A., D. R. Pino, H. G. I. Perlender, A. P. Osiroff, V. Segura, V. Lutz, M. L. Clara, C. F. Balestrini, and A. R. Piola (2009), Annual balance and seasonal variability of sea-air CO_2 fluxes in the Patagonia Sea: Their relationship with fronts and chlorophyll distribution, *Journal of Geophysical Research*, *114*, C03018, doi:10.1029/2008JC004854.

Biermann, L., C. Guinet, M. Bester, A. Brierley, and L. Boehme (2015), An alternative method for correcting fluorescence quenching, *Ocean Science*, *11*(1), 83–91, doi:10.5194/os-11-83-2015-supplement.

Bisbal, G. A. (1995), The Southeast South American shelf large marine ecosystem: Evolution and components, *Marine Policy*, *19*(1), 21–38.

Blain, S., B. Quéguiner, L. Armand, S. Belviso, B. Bombled, L. Bopp, A. Bowie, C. Brunet, C. Brussaard, F. Carlotti, U. Christaki, A. Corbière, I. Durand, F. Ebersbach, J.-L. Fuda, N. Garcia, L. Gerringa, B. Griffiths, C. Guigue, C. Guillerm, S. Jacquet, C. Jeandel, P. Laan, D. Lefèvre, C. Lo Monaco, A. Malits, J. Mosseri, I. Obernosterer, Y.-H. Park, M. Picheral, P. Pondaven, T. Remenyi, V. Sandroni, G. Sarthou, N. Savoye, L. Scouarnec, M. Souhaut, D. Thuiller, K. Timmermans, T. Trull, J. Uitz, P. van Beek, M. Veldhuis, D. Vincent, E. Viollier, L. Vong, and T. Wagener (2007), Effect of natural iron fertilization on carbon sequestration in the Southern Ocean, *Nature*, *446*, 1070–1074.

Bogazzi, E., A. Baldoni, A. Rivas, P. Martos, R. Reta, J. L. ORENSANZ, M. Lasta, P. Dell'Arciprete, and F. Werner (2005), Spatial correspondence between areas of concentration of Patagonian scallop (Zygochlamys patagonica) and frontal systems in the southwestern Atlantic, *Fisheries Oceanography*, *14*(5), 359–376.

Bonekamp, H., A. Sterl, and G. J. Komen (1999), Interannual variability in the Southern Ocean from an ocean model forced by European Centre for Medium?Range Weather Forecasts reanalysis fluxes, *Journal of Geophysical Research*, *104*(C6), 13,317–13,331.

Boss, E., and M. Behrenfeld (2010), In situ evaluation of the initiation of the North Atlantic phytoplankton bloom, *Geophysical Research Letters*, *37*(18), doi:10.1029/2010GL044174.

Boss, E., D. Swift, L. Taylor, P. Brickley, R. Zaneveld, S. Riser, M. J. Perry, and P. G. Strutton (2008), Observations of pigment and particle distributions in the western North Atlantic from an autonomous float and ocean color satellite, *Limnology and Oceanography*, *53*(5, part 2), 2112–2122.

Boss, E. B., and N. Haentjens (2016), Primer regarding measurements of chlorophyll fluorescence and the backscattering coefficient with WETLabs FLBB on profiling floats, *SOCCOM Technical Report 2016-1*, pp. 1–11.

Bourassa, M. A., E. Rodriguez, and R. Gaston (2010), NASA's Ocean Vector Winds Science Team Workshops, *Bulletin of the American Meteorological Society*, *91*(7), 925–928.

Box, G. E. P., G. M. Jenkins, and G. C. Reinsel (1994), *Time Series Analysis: Forecasting and Control*, John Wiley & Sons Inc.

Boyd, P. (2002), Environmental factors controlling phytoplankton processes in the Southern Ocean, *Journal of Phycology*, *38*, 844–861.

Boyd, P. W., and M. J. Ellwood (2010), The biogeochemical cycle of iron in the ocean, *Nature Publishing Group*, *3*(10), 675–682.

Boyd, P. W., E. Ibisanmi, S. G. Sander, K. A. Hunter, and G. A. Jackson (2010), Remineralization of upper ocean particles: Implications for iron biogeochemistry, *Limnology and Oceanography*, *55*(3), 1271–1288.

Brainerd, K. E., and M. C. Gregg (1995), Surface mixed and mixing layer depths, *Deep-Sea Research Part I*, *42*(9), 1521–1543.

Briggs, N., M. J. Perry, I. Cetinić, C. Lee, E. D'Asaro, A. M. Gray, and E. Rehm (2011), Deep-Sea Research I, *Deep-Sea Research Part I*, *58*(10), 1031–1039, doi: 10.1016/j.dsr.2011.07.007.

Brink, K. H. (2016), Cross-Shelf Exchange, *Annual Review of Marine Science*, *8*(1), 59–78.

Campagna, C., A. R. Piola, M. Rosa Marin, M. Lewis, and T. Fernández (2006), Southern elephant seal trajectories, fronts and eddies in the Brazil/Malvinas Confluence, *Deep Sea Research Part I: Oceanographic Research Papers*, *53*(12), 1907–1924, doi:10.1016/j.dsr.2006.08.015.

Campbell, J. (1995), The lognormal distribution as a model for bio-optical variability in the sea, *Journal of Geophysical Research*, *100*(C7), 13,237–13,254.

Capotondi, A., M. A. Alexander, N. A. Bond, E. N. Curchitser, and J. D. Scott (2012), Enhanced upper ocean stratification with climate change in the CMIP3 models, *Journal of Geophysical Research*, *117*, C04031, doi:10.1029/2011JC007409.

Carr, M.-E., and E. J. Kearns (2003), Production regimes in four Eastern Boundary Current systems, *Deep Sea Research Part II: Topical Studies in Oceanography*, *50*(22-26), 3199–3221.

Carranza, M. M., and S. T. Gille (2015), Southern Ocean wind-driven entrainment enhances satellite chlorophyll-a through the summer, *Journal of Geophysical Research*, *120*, doi:10.1002/2014JC010203.

Carreto, J. I., V. A. Lutz, M. O. Carignan, A. Colleoni, and S. G. De Marco (1995), Hydrography and Chlorophyll-a in a Transect From the Coast to the Shelf-Break in the Argentinian Sea, *Continental Shelf Research*, *15*(2-3), 315–336.

Carreto, J. I., N. G. Montoya, M. O. Carignan, R. Akselman, E. M. Acha, and C. Derisio (2016), Environmental and biological factors controlling the spring phytoplankton bloom at the Patagonian shelf-break front - Degraded fucoxanthin pigments and the importance of microzooplankton grazing, *Progress In Oceanography*, doi:10.1016/j.pocean.2016.05.002.

Chapman, D. C. (2002), Sensitivity of a Model Shelfbreak Front to the Parameterization of Vertical Mixing, *Journal of Physical Oceanography*, *32*, 3291–3298.

Chapman, D. C., and S. J. Lentz (1994), Trapping of a coastal density front by the bottom boundary layer, *Journal of Physical Oceanography*, *24*(7), 1464–1479.

Charo, M., and A. Piola (2014), Hydrographic data from the GEF Patagonia cruises, *Earth System Science Data Discussions*, *7*(1), 89–106, doi:10.5194/essdd-7-89-2014.

Charrassin, J.-B., M. Hindell, S. R. Rintoul, F. Roquet, S. Sokolov, M. Biuw, D. Costa, L. Boehme, P. Lovell, and R. Coleman (2008), Southern Ocean frontal structure and sea-ice formation rates revealed by elephant seals, *Proceedings of the National Academy of Sciences of the United States of America*, *105*(33), 11,634–11,639.

Charrassin, J.-B., F. Roquet, Y. H. Park, F. Bailleul, C. Guinet, M. Meredith, K. Nicholls, S. Thorpe, Y. Tremblay, and D. Costa (2010), New insights into Southern Ocean physical and biological processes revealed by instrumented elephant seals, *Proceedings of OceanObs 09: Sustained Ocean Observations and Information for Society (Vol. 2), Venice, Italy, 21-25 September 2009, Hall, J., Harrison DE & Stammer, D., Eds., ESA Publication WPP-306.*

Chelton, D. B. (2004), Satellite Measurements Reveal Persistent Small-Scale Features in Ocean Winds, *Science*, *303*(5660), 978–983.

Chisholm, S. W. (2000), Oceanography: stirring times in the Southern Ocean, *Nature*, *407*, 685–687.

Chiswell, S. (2011), Annual cycles and spring blooms in phytoplankton: don't abandon Sverdrup completely, *Marine Ecology Progress Series*, *443*, 39–50.

Claustre, H., P. Kerhervé, J. C. Marty, and L. Prieur (1994), Phytoplankton photoadaptation related to some frontal physical processes, *Journal of Marine Systems*, *5*(3), 251–265.

Close, S. E., and H. Goosse (2013), Entrainment-driven modulation of Southern Ocean mixed layer properties and sea ice variability in CMIP5 models, *Journal of Geophysical Research*, *118*(6), 2811–2827.

Cole, S. T., D. L. Rudnick, and J. A. Colosi (2010), Seasonal evolution of upper-ocean horizontal structure and the remnant mixed layer, *Journal of Geophysical Research*, *115*(C4), C04,012.

Combes, V., and R. P. Matano (2014), A two-way nested simulation of the oceanic circulation in the Southwestern Atlantic, *Journal of Geophysical Research: Oceans*, pp. n/a–n/a, doi:10.1002/2013JC009498.

Cullen, J., and M. R. Lewis (1988), The kinetics of algal photoadaptation in the context of vertial mixing, *Journal of Plankton Research*, *10*, 1039–1063.

Cullen, J. J. (1982), The deep chlorophyll maximum: comparing vertical profiles of chlorophyll a, *Canadian Journal of Fisheries and Aquatic Sciences*, *39*(5), 791–803.

Cullen, J. J. (2015), Subsurface Chlorophyll Maximum Layers: Enduring Enigma or Mystery Solved?, *Annual Review of Marine Science*, *7*(1), 207–239.

Cullen, J. J., and R. W. Eppley (1981), Chlorophyll maximum layers of the Southern-California Bight and possible mechanisms of their formation and maintenance, *Oceanologica acta*, *4*(1), 23–32.

D'Asaro, E., C. Lee, L. Rainville, R. Harcourt, and L. Thomas (2011), Enhanced Turbulence and Energy Dissipation at Ocean Fronts, *Science*, *332*, 318–322.

de Baar, H. J., J. T. De Jong, D. C. Bakker, B. M. Löscher, C. Veth, U. Bathmann, and V. Smetacek (1995), Importance of iron for plankton blooms and carbon dioxide drawdown in the Southern Ocean, *Nature*, *373*, 412–415.

de Baar, H. J. W. d., P. W. Boyd, K. H. Coale, M. R. Landry, A. Tsuda, P. Assmy, D. C. E. Bakker, Y. Bozec, R. T. Barber, M. A. Brzezinski, K. O. Buesseler, M. Boyé, P. L. Croot, F. Gervais, M. Y. Gorbunov, P. J. Harrison, W. T. Hiscock, P. Laan, C. Lancelot, C. S. Law, M. Levasseur, A. Marchetti, F. J. Millero, J. Nishioka, Y. Nojiri, T. v. Oijen, U. Riebesell, M. J. A. Rijkenberg, H. Saito, S. Takeda, K. R. Timmermans, M. J. W. Veldhuis, A. M. Waite, and C.-S. Wong (2005), Synthesis of iron fertilization experiments: From the Iron Age in the Age of Enlightenment, *Journal of Geophysical Research*, *110*, C09S16, doi:10.1029/2004JC002601.

de Boyer Montégut, C., G. Madec, A. S. Fischer, A. Lazar, and D. Iudicone (2004), Mixed layer depth over the global ocean:An examination of profile data and a profile-based climatology, *Journal of Geophysical Research*, *109*, C12003, doi:10.1029/2004JC002378.

de Szoeke, R. A. (1980), On the effects of horizontal variability of wind stress on the dynamics of the ocean mixed layer, *Journal of Physical Oceanography*, *10*, 1439–1454.

Del Castillo, C. E., and R. L. Miller (2011), Horizontal and vertical distributions of colored dissolved organic matter during the Southern Ocean Gas Exchange Experiment, *Journal of Geophysical Research*, *116*, C00F07, doi:10.1029/2010JC006781.

Denman, K. (1983), Time and space scales of vertical mixing and advection of phytoplankton in the upper ocean, *Limnology and Oceanography*.

Dewar, W. K., and G. R. Flierl (1987), Some Effects of the Wind on Rings, *Journal of Physical Oceanography*, *17*(10), 1653–1667.

Dierssen, H. M. (2010), Perspectives on empirical approaches for ocean color remote sensing of chlorophyll in a changing climate, *Proceedings of the National Academy of Sciences*, *107*(40), 17,073–17,078, doi:10.1073/pnas.0913800107.

Djavidnia, S., F. Mélin, and N. Hoepffner (2010), Comparison of global ocean colour data records, *Ocean Science*.

Doney, S. C. (2003), Mesoscale variability of Sea-viewing Wide Field-of-view Sensor (SeaWiFS) satellite ocean color: Global patterns and spatial scales, *Journal of Geophysical Research*, *108*(C2), 3024, doi:10.1029/2001JC000843.

Dong, S., S. T. Gille, J. Sprintall, and C. Gentemann (2006), Validation of the Advanced Microwave Scanning Radiometer for the Earth Observing System (AMSR-E) sea surface temperature in the Southern Ocean, *Journal of Geophysical Research*, *111*, C04002, doi:10.1029/2005JC002934.

Dong, S., J. Sprintall, S. T. Gille, and L. Talley (2008), Southern Ocean mixed-layer depth from Argo float profiles, *Journal of Geophysical Research*, *113*, C06013, doi:10.1029/2006JC004051.

Dragon, A.-C., P. Monestiez, A. Bar-Hen, and C. Guinet (2010), Linking foraging behaviour to physical oceanographic structures: Southern elephant seals and mesoscale eddies east of Kerguelen Islands, *Progress In Oceanography*, *87*(1-4), 61–71, doi:10.1016/j.pocean.2010.09.025.

Dusenberry, J. (2000), Steady-state single cell model simulations of photoacclimation in a vertically mixed layer: implications for biological tracer studies and primary productivity, *Journal of Marine Systems*.

Eichler, T. P., and J. Gottschalck (2013), A Comparison of Southern Hemisphere Cyclone Track Climatology and Interannual Variability in Coarse-Gridded Reanalysis Datasets, *Advances in Meteorology*, *2013*(19), 1–16.

Eppley, R. (1972), Temperature and phytoplankton growth in the sea, *Fish. Bull*, *70*(4), 1063–1085.

Eppley, R., and E. Renger (1988), Nanomolar increase in surface layer nitrate concentration following a small wind event, *Deep Sea Research*, *35*(7), 1119–1125.

Falabella, V. (2009), Atlas del Mar Patagónico, especies y espacios. V. Falabella, C. Campagna y J. Croxall (Eds.), Wildlife Conservation Society and BirdLife International, Buenos Aires.

Falkowski, b. P. G. (1983), Light-shade adaptation and vertical mixing of marine phytoplankton: A comparative field study , *Journal of Marine Research*, *41*, 215–237.

Fauchereau, N., A. Tagliabue, L. Bopp, and P. M. S. Monteiro (2011), The response of phytoplankton biomass to transient mixing events in the Southern Ocean, *Geophysical Research Letters*, *38*, L17601, doi:10.1029/2011GL048498.

Fedak, M. A. (2012), Deep-Sea Research II, *Deep Sea Research Part II ...*, pp. 1–7, doi:10.1016/j.dsr2.2012.07.007.

Fennel, K., M. R. Abbott, Y. Spitz, J. Richman, and D. Nelson (2003), Impacts of iron control on phytoplankton production in the modern and glacial Southern Ocean, *Deep Sea Research Part II*, *50*, 833–851.

Fiechter, J., and A. M. Moore (2009), Interannual spring bloom variability and Ekman pumping in the coastal Gulf of Alaska, *Journal of Geophysical Research*, *114*, C06004, doi:10.1029/2008JC005140.

Fitch, D. T., and J. K. Moore (2007), Wind speed influence on phytoplankton bloom dynamics in the Southern Ocean Marginal Ice Zone, *Journal of Geophysical Research*, *112*, C08006, doi:10.1029/2006JC004061.

Fox-Kemper, B., R. Ferrari, and R. Hallberg (2008), Parameterization of Mixed Layer Eddies. Part I: Theory and Diagnosis, *Journal of Physical Oceanography*, *38*(6), 1145–1165.

Franco, B. C., A. R. Piola, A. L. Rivas, A. Baldoni, and J. P. Pisoni (2008), Multiple thermal fronts near the Patagonian shelf break, *Geophysical Research Letters*, *35*(2), L02,607.

Franks, P. J., and L. J. Walstad (1997a), Phytoplankton patches at fronts: A model of formation and response to wind events, *Journal of Marine Research*, *55*(1), 1–29.

Franks, P. J. S. (1992), Phytoplankton blooms at fronts: patterns, scales and physical forcing mechanisms, *Reviews in Aquatic Sciences*, *6*(2), 121–137.

Franks, P. J. S. (2014), Has Sverdrup's critical depth hypothesis been tested? Mixed layers vs. turbulent layers, *ICES Journal of Marine Science*, doi:10.1093/icesjms/fsu175.

Franks, P. J. S., and L. J. Walstad (1997b), Phytoplankton patches at fronts: A model of formation and response to wind events, *Journal of Marine Research*, *55*(1), 1–29, doi:10.1357/0022240973224472.

Frants, M., S. T. Gille, M. Hatta, W. T. Hiscock, M. Kahru, C. I. Measures, B. G. Mitchell, and M. Zhou (2013), Analysis of horizontal and vertical processes contributing to natural iron supply in the mixed layer in southern Drake Passage, *Deep Sea Research Part II*, *90*, 68–76.

Fratantoni, P. S. (2003), Variability of the shelf break jet in the Middle Atlantic Bight: Internally or externally forced?, *Journal of Geophysical Research*, *108*(C5), 3166.

Garcia, V. M. T., C. A. E. Garcia, M. M. Mata, R. C. Pollery, A. R. Piola, S. R. Signorini, C. R. Mcclain, and M. D. Iglesias-Rodriguez (2008), Environmental factors controlling the phytoplankton blooms at the Patagonia shelf-break in spring, *Deep Sea Research Part I: Oceanographic Research Papers*, *55*(9), 1150–1166.

Gaube, P., D. B. Chelton, P. G. Strutton, and M. Behrenfeld (2013), Satellite observations of chlorophyll, phytoplankton biomass, and Ekman pumping in nonlinear mesoscale eddies, *Journal of Geophysical Research: Oceans*, doi:10.1002/jgrc.20477.

Gawarkiewicz, G., and D. C. Chapman (1992), The Role of Stratification in the Formation and Maintenance of Shelf-Break Fronts, *Journal of Physical Oceanography*, *22*, 753–773.

Gibbons, J. D. (1985), *Nonparametric Statistical Inference*, 2 ed., M. Dekker.

Gille, S. T. (2005), Statistical characterization of zonal and meridional ocean wind stress, *Journal of Atmospheric and Oceanic Technology*, *22*(9), 1353–1372.

Gómez, M. I., A. Piola, G. Kattner, and V. A. Alder (2011), Biomass of autotrophic dinoflagellates under weak vertical stratification and contrasting chlorophyll levels in subantarctic shelf waters, *Journal of Plankton Research*, *33*(8), 1304–1310.

Goni, G. J., F. Bringas, and P. N. Dinezio (2011), Observed low frequency variability of the Brazil Current front, *Journal of Geophysical Research*, *116*(C10), C10,037.

Gregg, M. C., T. Sanford, and D. Winkel (2003), Reduced mixing from the breaking of internal waves in equatorial waters, *Nature*, *422*(6931), 513–515.

Grenier, M., A. Della Penna, and T. W. Trull (2015), Autonomous profiling float observations of the high-biomass plume downstream of the Kerguelen Plateau in the Southern Ocean, *Biogeosciences*, *12*(9), 2707–2735, doi:10.5194/bg-12-2707-2015-supplement.

Griffith, G. P., R. Vennell, and M. J. M. Williams (2010), An algal photoprotection index and vertical mixing in the Southern Ocean, *Journal of Plankton Research*, *32*(4), 515–527, doi:10.1093/plankt/fbq003.

Guerrero, R. A., and A. R. Piola (1997), Masas de agua en la plataforma continental, *El Mar Argentino y sus Recursos Pesqueros*, *1*, 107–118.

Guerrero, R. A., A. R. Piola, H. Fenco, R. P. Matano, V. Combes, Y. Chao, C. James, E. D. Palma, M. Saraceno, and P. T. Strub (2014), The salinity signature of the cross-shelf exchanges in the Southwestern Atlantic Ocean: Satellite observations, *Journal of Geophysical Research: Oceans*, *119*(11), 7794–7810.

Guinet, C., X. Xing, E. Walker, and P. Monestiez (2013), Calibration procedures and first dataset of Southern Ocean chlorophyll a profiles collected by elephant seals equipped with a newly developed CTD-fluorescence tags, *Earth Syst. Sci. Data*, *5*, 15–29.

Håkanson, L., J. M. Malmaeus, U. Bodemer, and V. Gerhardt (2003), Coefficients of variation for chlorophyll, green algae, diatoms, cryptophytes and blue-greens in rivers as a basis for predictive modelling and aquatic management, *Ecological modelling*, *169*(1), 179–196.

Hales, B., R. D. Vaillancourt, L. Prieto, J. Marra, R. Houghton, and D. Hebert (2009), Journal of Marine Systems, *Journal of Marine Systems*, *78*(3), 426–441.

Hauck, J., C. Völker, D. A. Wolf-Gladrow, C. Laufkotter, M. Vogt, O. Aumont, L. Bopp, E. T. Buitenhuis, S. C. Doney, J. Dunne, N. Gruber, T. Hashioka, J. John, C. L. Quéré, I. Lima, H. Nakano, R. Séférian, and I. Totterdell (2015), On the Southern Ocean CO2 uptake and the role of the biological carbon pump in the 21st century, *Global Biogeochemical Cycles*, *29*(9), 1451–1470.

He, R., K. Chen, K. Fennel, G. G. Gawarkiewicz, and D. J. McGillicuddy, Jr. (2011), Seasonal and interannual variability of physical and biological dynamics at the shelfbreak front of the Middle Atlantic Bight: nutrient supply mechanisms, *Biogeosciences*, *8*(10), 2935–2946.

Heileman, S. (2009), Patagonian Shelf: LME, *The UNEP Large Marine Ecosystem Report: A perspective on changing conditions in LMEs of the world's Regional Seas. UNEP Regional Seas Report and Studies*, pp. 735–746.

Hense, I., R. Timmermann, A. Beckmann, and U. Bathmann (2003), Regional ecosystem dynamics in the ACC: simulations with a three-dimensional ocean-plankton model, *Journal of Marine Systems*, *42*(1-2), 31–51.

Henson, S. A., and A. C. Thomas (2007), Interannual variability in timing of bloom initiation in the California Current System, *Journal of Geophysical Research*, *112*, C08007, doi:10.1029/2006JC003960.

Hoffmann, L. J., I. Peeken, and K. Lochte (2008), Iron, silicate, and light co-limitation of three Southern Ocean diatom species, *Polar Biology*, *31*(9), 1067–1080.

Holm-Hansen, O., A. F. Amos, and C. D. Hewes (2000), Reliability of estimating chlorophyll a concentrations in Antarctic waters by measurement of in situ chlorophyll a fluorescence, *Marine ecology progress series. Oldendorf*, *196*, 103–110.

Holm-Hansen, O., M. Kahru, and C. D. Hewes (2005), Deep chlorophyll a maxima (DCMs) in pelagic Antarctic waters. II. Relation to bathymetric features and dissolved iron concentrations, *Marine Ecology Progress Series*, *297*, 71–81.

Holte, J., and L. Talley (2009), A New Algorithm for Finding Mixed Layer Depths with Applications to Argo Data and Subantarctic Mode Water Formation*, *Journal of Atmospheric and Oceanic Technology*, *26*(9), 1920–1939.

Holte, J., J. Gilson, T. L., and D. Roemmich (2010), Argo Mixed Layers, online document, Scripps Institution of Oceanography, http://mixedlayer.ucsd.edu, Accessed 20 September 2011.

Holte, J. W., L. D. Talley, T. K. Chereskin, and B. M. Sloyan (2012), The role of air-sea fluxes in Subantarctic Mode Water formation, *Journal of Geophysical Research*, *117*(C3).

Hopkinson, B., B. G. Mitchell, and R. Reynolds (2007), Iron limitation across chlorophyll gradients in the southern Drake Passage: Phytoplankton responses to iron addition and photosynthetic indicators of iron stress, *Limnology and ...*.

Hoskins, B., and K. I. Hodges (2005), A new perspective on Southern Hemisphere storm tracks, *Journal of Climate*, *18*, 4108–4129.

Houghton, R. W., F. Aikman, and H. W. OU (1988), Shelf-Slope Frontal Structure and Cross-Shelf Exchange at the New-England Shelf-Break, *Continental Shelf Research*, *8*(5-7), 687–710.

Huisman, J., P. van Oostveen, and F. Weissing (1999), Critical depth and critical turbulence: two different mechanisms for the development of phytoplankton blooms, *Limnology and Oceanography*, pp. 1781–1787.

IOCCG (2004), *Guide to the creation and use of ocean-colour, Level-3, binned data products*, *Reports of the International Ocean Colour Coordinating Group*, vol. No. 4, IOCCG, Dartmouth, Canada.

IOCCG (2015), Ocean Colour Remote Sensing in Polar Seas, *IOCCG Report Number 16*.

Jaud, T., A.-C. Dragon, J. V. Garcia, and C. Guinet (2012), Relationship between Chlorophyll a Concentration, Light Attenuation and Diving Depth of the Southern Elephant Seal Mirounga leonina, *PLoS ONE*, *7*(10), e47,444, doi:10.1371/journal.pone.0047444.t004.

Jickells, T. D. (2005), Global Iron Connections Between Desert Dust, Ocean Biogeochemistry, and Climate, *Science*, *308*, 67–71.

Jones, D. A., and I. Simmonds (1993), A Climatology of Southern-Hemisphere Extratropical Cyclones, *Climate Dynamics*, *9*(3), 131–145.

Kahru, M., and B. G. Mitchell (2010), Blending of ocean colour algorithms applied to the Southern Ocean, *Remote Sensing Letters*, *1*(2), 119–124.

Kahru, M., S. T. Gille, R. Murtugudde, P. G. Strutton, M. Manzano-Sarabia, H. Wang, and B. G. Mitchell (2010), Global correlations between winds and ocean chlorophyll, *Journal of Geophysical Research*, *115*, C12040, doi:10.1029/2010JC006500.

Kara, A. B., P. A. Rochford, and H. E. Hurlburt (2000), An optimal definition for ocean mixed layer depth, *Journal of Geophysical Research*, *105*(C7), 16,803–16,821.

Kelly, K. A., S. Dickinson, M. J. McPhaden, and G. C. Johnson (2001), Ocean currents evident in satellite wind data, *Geophysical Research Letters*, *28*(1), 2469–2472.

Kilbourne, B. F., and J. B. Girton (2015), Surface boundary layer evolution and near-inertial wind power input, *Journal of Geophysical Research: Oceans*, *120*(11), 7506–7520.

Kim, D., E. J. Yang, K. H. Kim, C. W. Shin, J. Park, S. Yoo, and J. H. Hyun (2011), Impact of an anticyclonic eddy on the summer nutrient and chlorophyll a distributions in the Ulleung Basin, East Sea (Japan Sea), *ICES Journal of Marine Science*, *69*(1), 23–29.

Klein, P., and B. Coste (1984), Effects of wind-stress variability on nutrient transport into the mixed layer, *Deep Sea Research*, *31*(1), 21–37.

Knox, G. A. (2007), *Biology of the Southern Ocean, Second Edition*, 116 pp.

Korb, R., M. Whitehouse, A. Atkinson, and S. Thorpe (2008), Magnitude and maintenance of the phytoplankton bloom at South Georgia: a naturally iron-replete environment, *Marine Ecology Progress Series*, *368*, 75–91.

Krauss, W., R. Döscher, A. Lehmann, and T. Viehoff (1990), On eddy scales in the eastern and northern North Atlantic Ocean as a function of latitude, *Journal of Geophysical Research*, *95*(C10), 18,049–18,056.

Kukulka, T., A. J. Plueddemann, J. H. Trowbridge, and P. P. Sullivan (2009), Significance of Langmuir circulation in upper ocean mixing: Comparison of observations and simulations, *Geophysical Research Letters*, *36*, L10603, doi:10.1029/2009GL037620.

Lancelot, C., A. de Montety, H. Goosse, S. Becquevort, V. Schoemann, B. Pasquer, and M. Vancoppenolle (2009), Spatial distribution of the iron supply to phytoplankton in the Southern Ocean: a model study, *Biogeosciences*, *6*(12), 2861–2878.

Lapeyre, G., P. Klein, and B. Hua (2006), Oceanic restratification forced by surface frontogenesis, *Journal of Physical Oceanography*, *36*(8), 1577–1590.

Le Quéré, C., L. Bopp, and I. Tegen (2002), Antarctic circumpolar wave impact on marine biology: A natural laboratory for climate change study, *Geophysical Research Letters*, *29*(10), 1407, doi:10.1029/2001GL014585.

Le Traon, P. Y. (1990), A Method for Optimal Analysis of Fields With Spatially Variable Mean, *Journal of Geophysical Research*, *95*, 13,543–13,547.

Ledwell, J. R., L. C. St Laurent, J. B. Girton, and J. M. Toole (2011), Diapycnal Mixing in the Antarctic Circumpolar Current, *Journal of Physical Oceanography*, *41*(1), 241–246, doi:10.1175/2010JPO4557.1.

Lee, T., O. Wang, W. Tang, and W. T. Liu (2008), Wind stress measurements from the QuikSCAT-SeaWinds scatterometer tandem mission and the impact on an ocean model, *Journal of Geophysical Research*, *113*, C12019, doi:10.1029/2008JC004855.

Legendre, P. (2005), Species associations: the Kendall coefficient of concordance revisited, *Journal of Agricultural, Biological, and Environmental Statistics*, *10*(2), 226–245.

Lehahn, Y., F. d'Ovidio, M. Lévy, Y. Amitai, and E. Heifetz (2011), Long range transport of a quasi isolated chlorophyll patch by an Agulhas ring, *Geophysical Research Letters*, *38*, L16610, doi:doi:10.1029/2011GL048588.

Lévy, M., P. Klein, and M. Ben Jelloul (2009), New production stimulated by high-frequency winds in a turbulent mesoscale eddy field, *Geophysical Research Letters*, *36*, L16603, doi:10.1029/2009GL039490.

Lewis, M. R., J. J. Cullen, and T. R. Platt (1984a), Relationships between vertical mixing and photoadaptation of phytoplankton: similarity criteria, *Marine ecology progress ...*.

Lewis, M. R., E. P. W. Horne, J. J. Cullen, N. S. Oakey, and T. Platt (1984b), Turbulent motions may control phytoplankton photosynthesis in the upper ocean, *Nature*, *311*(5), 49–50.

Li, M., and C. Garrett (1997), Mixed layer deepening due to Langmuir circulation, *Journal of Physical Oceanography*, *27*, 121–132.

Li, M., K. Zahariev, and C. Garrett (1995), Role of Langmuir circulation in the deepening of the ocean surface mixed layer, *Science*, *270*, 1955–1957.

Linder, C. A., G. G. Gawarkiewicz, and R. S. Pickart (2004), Seasonal characteristics of bottom boundary layer detachment at the shelfbreak front in the Middle Atlantic Bight, *Journal of Geophysical Research*, *109*, C03049, doi:10.1029/2003JC002032.

Llido, J., V. Garçon, J. Lutjeharms, and J. Sudre (2005), Event-scale blooms drive enhanced primary productivity at the Subtropical Convergence, *Geophysical Research Letters*, *32*, L15611, doi:10.1029/2005GL022880.

Longhurst, A. (2007), The Atlantic Ocean, *Ecological geography of the sea, 2nd edn. Elsevier Science Publishers, New York*, pp. 131–268.

Lovenduski, N. S., and N. Gruber (2005), Impact of the Southern Annular Mode on Southern Ocean circulation and biology, *Geophysical Research Letters*, *32*, L11603, doi:10.1029/2005GL022727.

Luo, C., N. Mahowald, and N. Meskhidze (2005), Estimation of iron solubility from observations and a global aerosol model, *Journal of Geophysical Research*, *110*, D23307, doi:10.1029/2005JD006059.

Lutz, V. A., V. Segura, A. I. Dogliotti, D. A. Gagliardini, A. A. Bianchi, and C. F. Balestrini (2010), Primary production in the Argentine Sea during spring estimated by field and satellite models, *Journal of Plankton Research*, *32*(2), 181–195.

Machado, I., M. Barreiro, and D. Calliari (2013), Variability of chlorophyll-a in the Southwestern Atlantic from satellite images Seasonal cycle and ENSO influences, *Continental Shelf Research*, *53*(C), 102–109, doi:10.1016/j.csr.2012.11.014.

MacIntyre, S. (2008), Turbulent Mixing and Resource Supply to Phytoplankton , *Physical Processes in Lakes and Oceans. Coastal and Estuarine Studies*, *54*, 561–590.

Mahadevan, A., and J. Campbell (2002), Biogeochemical patchiness at the sea surface, *Geophysical Research Letters*, *29*(19), 32–1–32–4.

Mahadevan, A., L. N. Thomas, and A. Tandon (2008), Comment on "Eddy/Wind Interactions Stimulate Extraordinary Mid-Ocean Plankton Blooms", *Science*, *320*, 448b.

Marinov, I., M. Follows, A. Gnanadesikan, J. L. Sarmiento, and R. D. Slater (2008), How does ocean biology affect atmospheric pCO2? Theory and models, *Journal of Geophysical Research*, *113*, C07032, doi:10.1029/2007JC004598.

Maritorena, S., and D. Siegel (2005), Consistent merging of satellite ocean color data sets using a bio-optical model, *Remote Sensing of Environment*, *94*, 429–440.

Marra, J. (1978), Phytoplankton Photosynthetic Response to Vertical Movement in a Mixed Layer, *Marine Biology*, *46*, 203–208.

Marra, J., and R. Barber (2005), Primary productivity in the Arabian Sea: a synthesis of JGOFS data, *Progress In Oceanography*, *65*, 159–175.

Marra, J., R. Bidigare, and T. Dickey (1990), Nutrients and mixing, chlorophyll and phytoplankton growth, *Deep Sea Research*, *37*, 127–143.

Martin, A. P., and K. J. Richards (2001), Mechanisms for vertical nutrient transport within a North Atlantic mesoscale eddy, *Deep Sea Research Part I—*, *48*, 757–773.

Martin, J., R. Gordon, and S. Fitzwater (1990a), Iron in Antarctic waters, *Nature*, *345*, 156–158.

Martin, J., S. Fitzwater, and R. Gordon (1990b), Iron deficiency limits phytoplankton growth in Antarctic waters, *Global Biogeochemical Cycles*, *4*, 5–12.

Martin, P., M. R. van der Loeff, N. Cassar, P. Vandromme, F. d'Ovidio, L. Stemmann, R. Rengarajan, M. Soares, H. E. González, F. Ebersbach, R. S. Lampitt, R. Sanders, B. A. Barnett, V. Smetacek, and S. W. A. Naqvi (2013), Iron fertilization enhanced net community production but not downward particle flux during the Southern Ocean iron fertilization experiment LOHAFEX, *Global Biogeochemical Cycles*, *27*, 871–881, doi:10.1002/gbc.20077.

Martinez-Vicente, V., G. Dall'Olmo, G. Tarran, E. Boss, and S. Sathyendranath (2013), Optical backscattering is correlated with phytoplankton carbon across the Atlantic Ocean, *Geophysical Research Letters*, *40*(6), 1154–1158, doi:10.1002/grl.50252.

Matano, R. P., and E. D. Palma (2008), On the Upwelling of Downwelling Currents, *Journal of Physical Oceanography*, *38*, 2482, doi:10.1175/2008JPO3783.1.

Matano, R. P., V. Combes, A. R. Piola, R. Guerrero, E. D. Palma, P. Ted Strub, C. James, H. Fenco, Y. Chao, and M. Saraceno (2014), The salinity signature of the cross-shelf exchanges in the Southwestern Atlantic Ocean: Numerical simulations, *Journal of Geophysical Research: Oceans*, *119*(11), 7949–7968.

McDougall, T. J., and P. M. Barker (2011), Getting started with TEOS-10 and the Gibbs Seawater (GSW) Oceanographic Toolbox, *SCOR/IAPSO WG127*, pp. 1–34.

McGillicuddy, D. J., L. A. Anderson, N. R. Bates, T. Bibby, K. O. Buesseler, C. A. Carlson, C. S. Davis, C. Ewart, P. G. Falkowski, S. A. Goldthwait, D. A. Hansell, W. Jenkins, R. Johnson, V. K. Kosnyrev, J. R. Ledwell, Q. P. Li, D. A. Siegel, and

D. K. Steinberg (2007), Eddy/Wind Interactions Stimulate Extraordinary Mid-Ocean Plankton Blooms, *Science*, *316*, 1021–1026.

McPhaden, M. J., M. F. Cronin, and D. C. McClurg (2008), Meridional Structure of the Seasonally Varying Mixed Layer Temperature Balance in the Eastern Tropical Pacific, *Journal of Climate*, *21*, 3240–3260.

Meskhidze, N., A. Nenes, W. Chameides, C. Luo, and N. Mahowald (2007), Atlantic Southern Ocean productivity: Fertilization from above or below?, *Global Biogeochemical Cycles*, *21*, GB2006, doi:10.1029/2006GB002711.

Mignot, A., H. Claustre, F. D'Ortenzio, X. Xing, A. Poteau, and J. Ras (2011), From the shape of the vertical profile of in vivo fluorescence to Chlorophyll-a concentration, *Biogeosciences*, *8*(8), 2391–2406, doi:10.5194/bg-8-2391-2011.

Mignot, A., H. Claustre, J. Uitz, A. Poteau, F. D'ortenzio, and X. Xing (2014), PUBLICATIONS, pp. 1–21, doi:10.1002/(ISSN)1944-9224.

Mignot, A., R. Ferrari, and K. A. Mork (2016), Spring bloom onset in the Nordic Seas, *Biogeosciences*, *13*(11), 3485–3502.

Miller, C. B., B. W. Frost, B. Booth, P. A. Wheeler, M. R. Landry, and N. Welschmeyer (1991), Ecological processes in the subarctic Pacific: iron limitation cannot be the whole story, *Oceanography*, *4*(2), 71–78.

Miller, R. N., R. P. Matano, and E. D. Palma (2011), Shelfbreak upwelling induced by alongshore currents: analytical and numerical results, *Journal of Fluid Mechanics*, *686*, 239–249, doi:10.1017/jfm.2011.326.

Mitchell, B., and O. Holm-Hansen (1991), Observations of modeling of the Antartic phytoplankton crop in relation to mixing depth, *Deep Sea Research*, *38*(8/9), 981–1007.

Mitchell, B. G., and M. Kahru (2009), Bio-Optical Algorithms for ADEOS-2 GLI, *Journal of The Remote Sensing Society of Japan*, *29*(1), 80–85.

Mitchell, B. G., and D. A. Kiefer (1988), Chlorophyll a specific absorption and fluorescence excitation spectra for fight-limited phytoplankton, pp. 1–25.

Mizobata, K., S. Saitoh, A. Shiomoto, T. Miyamura, N. Shiga, K. Imai, M. Toratani, Y. Kajiwara, and K. Sasaoka (2002), Bering Sea cyclonic and anticyclonic eddies observed during summer 2000 and 2001, *Progress In Oceanography*, *55*, 65–75.

Moore, J., and M. Abbott (2000), Phytoplankton chlorophyll distributions and primary production in the Southern Ocean, *Journal of Geophysical Research*, *105*(C12), 28,709–28,722.

Moore, J. K. (2004), Upper ocean ecosystem dynamics and iron cycling in a global three-dimensional model, *Global Biogeochemical Cycles*, *18*, GB4028, doi:10.1029/2004GB002220.

Morel, A., and J.-F. Berthon (1989), Surface pigments, algal biomass profiles, and potential production of the euphotic layer: Relationships reinvestigated in view of remote-sensing applications, *Limnol. Oceanogr*, *34*(8), 1545–1562.

Morel, A., and L. Prieur (1977), Analysis of variations in ocean color, *Limnology and Oceanography*, *22*, 709–722.

Morrison, A. K., T. L. Frölicher, and J. L. Sarmiento (2015), Upwelling in the Southern Ocean, *Physics Today*, *68*(1), 27–32.

Muller-Karger, F. E. (2005), The importance of continental margins in the global carbon cycle, *Geophysical Research Letters*, *32*, L01602, doi:10.1029/2004GL021346.

Musgrave, D., J. Chou, and W. Jenkins (1988), Application of a model of upper-ocean physics for studying seasonal cycles of oxygen, *Journal of Geophysical Research*, *93*(C12), 15,679–15,700.

Nagai, T., A. Tandon, and D. L. Rudnick (2006), Two-dimensional ageostrophic secondary circulation at ocean fronts due to vertical mixing and large-scale deformation, *Journal of Geophysical Research*, *111*, C09038, doi:10.1029/2005JC002964.

Nakamura, H., T. Izumi, and T. Sampe (2002), Interannual and decadal modulations recently observed in the Pacific storm track activity and East Asian winter monsoon, *Journal of Climate*, *15*, 1855–1874.

Neori, A., and O. Holm-Hansen (1982), Effect of temperature on rate of photosynthesis in Antarctic phytoplankton, *Polar Biology*, *1*, 33–38.

O'Malley, R. T., M. J. Behrenfeld, D. A. Siegel, and S. Maritorena (2010), Global ocean phytoplankton. In D.S. Arndt, M.O. Baringer and M.R. Johnson (Eds.), State of the Climate in 2009, *Bulletin of the American Meteorological Society*, *91*(7), S75–S78.

O'Neill, L., and D. Chelton (2003), Observations of SST-induced perturbations of the wind stress field over the Southern Ocean on seasonal timescales, *Journal of Climate*, *16*, 2340–2354.

O'Neill, L., and D. Chelton (2010), The effects of SST-induced surface wind speed and direction gradients on midlatitude surface vorticity and divergence, *Journal of Climate*, *23*, 255–281.

O'Reilly, J., S. Maritorena, B. Mitchell, D. Siegel, K. Carder, S. Garver, M. Kahru, and C. McClain (1998), Ocean color chlorophyll algorithms for SeaWiFS, *Journal of Geophysical Research*, *103*(C11), 24,937–24,953.

Orsi, A., T. Whitworth, and W. Nowlin (1995), On the meridional extent and fronts of the Antarctic Circumpolar Current, *Deep Sea Research Part I*, *42*(5), 641–673.

Osborn, T. (1980), Estimates of the Local Rate of Vertical Diffusion from Dissipation Measurements, *Journal of Physical Oceanography*, *10*, 83–89.

Painter, S. C., A. J. Poulton, J. T. Allen, R. Pidcock, and W. M. Balch (2010), The COPAS'08 expedition to the Patagonian Shelf: Physical and environmental conditions during the 2008 coccolithophore bloom, *Continental Shelf Research*, *30*(18), 1907–1923.

Palma, E. D., R. P. Matano, and A. R. Piola (2004), A numerical study of the Southwestern Atlantic Shelf circulation: Barotropic response to tidal and wind forcing, *Journal of Geophysical Research*, *109*, C08014, doi:10.1029/2004JC002315.

Palma, E. D., R. P. Matano, and A. R. Piola (2008), A numerical study of the Southwestern Atlantic Shelf circulation: Stratified ocean response to local and offshore forcing, *Journal of Geophysical Research*, *113*, C11010, doi:10.1029/2007JC004720.

Perez-Cenci, M., G. F. Caló, R. I. Silva, R. M. Negri, and G. L. Salerno (2014), The First Molecular Characterization of Picocyanobacteria from the Argentine Sea, *Journal of Marine Biology*, *2014*(1), 1–8.

Perry, M. J., B. S. Sackmann, C. C. Eriksen, and C. M. Lee (2008), Seaglider observations of blooms and subsurface chlorophyll maxima off the Washington coast, pp. 1–11.

Piola, A. R., and V. Falabella (2009), *El Mar Patagónico*, 55–75 pp., Atlas del Mar Patagnico, especies y espacios, V. Falabella, C. Campagna y J. Croxall (Eds.), Wildlife Conservation Society y BirdLife International, Buenos Aires.

Piola, A. R., E. J. D. Campos, O. O. Moller, M. Charo, and C. Martinez (2000), Subtropical Shelf Front off eastern South America, *Journal of Geophysical Research: Oceans*, *105*(C), 6565–6578.

Piola, A. R., S. I. Romero, and U. Zajaczkovski (2008), Space–time variability of the Plata plume inferred from ocean color, *Continental Shelf Research*, *28*(13), 1556–1567.

Piola, A. R., N. Martínez Avellaneda, R. A. Guerrero, F. P. Jardón, E. D. Palma, and S. I. Romero (2010), Malvinas-slope water intrusions on the northern Patagonia continental shelf, *Ocean Science*, *6*(1), 345–359.

Piola, A. R., B. C. Franco, E. D. Palma, and M. Saraceno (2013), Multiple jets in the Malvinas Current, *Journal of Geophysical Research: Oceans*, *118*(4), 2107–2117.

Podestá, G. P. (1990), Migratory pattern of Argentine hake Merluccius hubbsi and oceanic processes in the Southwestern Atlantic Ocean, *Fishery Bulletin*, *88*(1), 167–177.

Pollard, R., M. Lucas, and J. Read (2002), Physical controls on biogeochemical zonation in the Southern Ocean, *Deep Sea Research Part II*, *49*, 3289–3305.

Post, A. F., Z. Dubinsky, K. Wyman, and P. G. Falkowski (1984), Kinetics of light-intensity adaptation in a marine planktonic diatom *, *Marine Biology*, *83*, 231–238.

Poulton, A. J., S. C. Painter, J. R. Young, N. R. Bates, B. Bowler, D. Drapeau, E. Lyczsckowski, and W. M. Balch (2013), The 2008 Emiliania huxleyi bloom along the Patagonian Shelf: Ecology, biogeochemistry, and cellular calcification, *Global Biogeochemical Cycles*, *27*(4), 1023–1033.

Powell, J. R., and M. D. Ohman (2015), Deep-Sea Research II, *Deep Sea Research Part II ...*, *112*(c), 79–90.

Press, W. H., S. A. Teukolsky, W. T. Vetterling, and B. P. Flannery (2007), *Numerical Recipes The Art of Scientific Computing*, 3 ed., 773 pp., Cambridge University Press, Cambridge, U.K.

Price, J. (1981), Upper ocean response to a hurricane, *J. Phys. Oceanogr*, *11*(2), 153–175.

Proctor, C. W., and C. S. Roesler (2010), New insights on obtaining phytoplankton concentration and composition from in situ multispectral Chlorophyll fluorescence, *Limnology and Oceanography: Methods*, *8*, 695–708.

Racault, M.-F., C. Le Quéré, E. Buitenhuis, S. Sathyendranath, and T. Platt (2012), Phytoplankton phenology in the global ocean, *Ecological Indicators*, *14*, 152–163.

Reay, D., J. Priddle, D. Nedwell, M. Whitehouse, J. Ellis-Evans, C. Deubert, and D. Connelly (2001), Regulation by low temperature of phytoplankton growth and nutrient uptake in the Southern Ocean, *Marine Ecology Progress Series*, *219*, 51–64.

Ricker, W. E. (1973), Linear regressions in Fishery Research, *Fisheries Research Board of Canada*, *30*, 409–434.

Risien, C., and D. Chelton (2008), A global climatology of surface wind and wind stress fields from eight years of quikscat scatterometer data, *Journal of Physical Oceanography*, *38*(11), 2379–2413.

Rivas, A. L. (2006), Quantitative estimation of the influence of surface thermal fronts over chlorophyll concentration at the Patagonian shelf, *Journal of Marine Systems*, *63*(3-4), 183–190, doi:10.1016/j.jmarsys.2006.07.002.

Romero, S. I., A. R. Piola, M. Charo, and C. A. E. Garcia (2006), Chlorophyll-avariability off Patagonia based on SeaWiFS data, *Journal of Geophysical Research*, *111*(C5), doi:10.1029/2005JC003244.

Roquet, F., J.-B. Charrassin, S. Marchand, L. Boehme, M. Fedak, G. Reverdin, and C. Guinet (2011), Delayed-Mode Calibration of Hydrographic Data Obtained from Animal-Borne Satellite Relay Data Loggers, *Journal of Atmospheric and Oceanic Technology*, *28*(6), 787–801.

Roquet, F., C. Wunsch, G. Forget, P. Heimbach, C. Guinet, G. Reverdin, J.-B. Charrassin, F. Bailleul, D. P. Costa, L. A. Huckstadt, K. T. Goetz, K. M. Kovacs, C. Lydersen, M. Biuw, O. A. Nøst, H. Bornemann, J. Ploetz, M. N. Bester, T. McIntyre, M. C. Muelbert, M. A. Hindell, C. R. McMahon, G. Williams, R. Harcourt, I. C. Field, L. Chafik, K. W. Nicholls, L. Boehme, and M. A. Fedak (2013), Estimates of the Southern Ocean general circulation improved by animal-borne instruments, *Geophysical Research Letters*, *40*(23), 6176–6180.

Russell, J., K. Dixon, A. Gnanadesikan, R. Stouffer, and J. Toggweiler (2006), The Southern Hemisphere westerlies in a warming world: Propping open the door to the deep ocean, *Journal of Climate*, *19*(24), 6382–6390.

Russell, J., J. Sarmiento, H. Cullen, R. Hotinski, K. Johnson, S. Riser, and L. Talley (2014), The Southern Ocean Carbon and ClimateObservations and Modeling Program (SOCCOM), pp. 1–28.

Ryther, J. H., and E. M. Hulburt (1960), On winter mixing and the vertical distribution of phytoplankton, *Limnology and Oceanography*, *5*, 337–338.

Sackmann, B. S., M. J. Perry, and C. C. Eriksen (2008), Seaglider observations of variability in daytime fluorescence quenching of chlorophyll-a in Northeastern Pacific coastal waters., *Biogeosciences Discussions*, *5*(4).

Saha, S., S. Moorthi, H.-L. Pan, X. Wu, J. Wang, S. Nadiga, P. Tripp, R. Kistler, J. Woollen, D. Behringer, H. Liu, D. Stokes, R. Grumbine, G. Gayno, J. Wang, Y.-T. Hou, H.-Y. Chuang, H.-M. H. Juang, J. Sela, M. Iredell, R. Treadon, D. Kleist, P. Van Delst, D. Keyser, J. Derber, M. Ek, J. Meng, H. Wei, R. Yang, S. Lord, H. Van Den Dool, A. Kumar, W. Wang, C. Long, M. Chelliah, Y. Xue, B. Huang, J.-K. Schemm, W. Ebisuzaki, R. Lin, P. Xie, M. Chen, S. Zhou, W. Higgins, C.-Z. Zou, Q. Liu, Y. Chen, Y. Han, L. Cucurull, R. W. Reynolds, G. Rutledge, and M. Goldberg (2010a), NCEP Climate Forecast System Reanalysis (CFSR) 6-hourly Products, January 1979 to December 2010, http://dx.doi.org/10.5065/D69K487J, Research Data Archive at the National Center for Atmospheric Research, Computational and Information Systems Laboratory, Boulder, Colo. Accessed 30 Oct 2013.

Saha, S., S. Moorthi, H.-L. Pan, X. Wu, J. Wang, S. Nadiga, P. Tripp, R. Kistler, J. Woollen, D. Behringer, H. Liu, D. Stokes, R. Grumbine, G. Gayno, J. Wang, Y.-T. Hou, H.-Y. Chuang, H.-M. H. Juang, J. Sela, M. Iredell, R. Treadon, D. Kleist, P. Van Delst, D. Keyser, J. Derber, M. Ek, J. Meng, H. Wei, R. Yang, S. Lord, H. Van Den Dool, A. Kumar, W. Wang, C. Long, M. Chelliah, Y. Xue, B. Huang, J.-K. Schemm, W. Ebisuzaki, R. Lin, P. Xie, M. Chen, S. Zhou, W. Higgins, C.-Z. Zou, Q. Liu, Y. Chen, Y. Han, L. Cucurull, R. W. Reynolds, G. Rutledge, and M. Goldberg (2010b), The NCEP Climate Forecast System Reanalysis, *Bulletin of the American Meteorological Society*, *91*(8), 1015–1057.

Sallée, J.-B., N. Wienders, K. Speer, and R. Morrow (2006), Formation of subantarctic mode water in the southeastern Indian Ocean, *Ocean Dynamics*, *56*(5-6), 525–542.

Sallée, J. B., K. G. Speer, and S. R. Rintoul (2010), Zonally asymmetric response of the Southern Ocean mixed-layer depth to the Southern Annular Mode, *Nature Geoscience*, *3*, 273–279.

Sanford, T. B., J. H. Dunlap, J. A. Carlson, D. C. Webb, and J. B. Girton (2005), Autonomous velocity and density profiler: EM-APEX, *Current Measurement Technology, 2005. Proceedings of the IEEE/OES Eighth Working Conference on*, pp. 152–156.

Saraceno, M., C. Provost, and A. R. Piola (2005), On the relationship between satellite-retrieved surface temperature fronts and chlorophyll ain the western South Atlantic, *Journal of Geophysical Research*, *110*(C11), doi:10.1029/2004JC002736.

Schloss, I. R., G. A. Ferreyra, M. E. Ferrario, G. O. Almandoz, R. Codina, A. A. Bianchi, C. F. Balestrini, H. A. Ochoa, D. Ruiz Pino, and A. Poisson (2007), Role of plankton communities in sea-air variations in pCO_2 in the SW Atlantic Ocean, *Marine Ecology Progress Series*, *332*, 93–106.

Sedwick, P. N., and G. R. Ditullio (1997), Regulation of algal blooms in Antarctic Shelf Waters by the release of iron from melting sea ice, *Geophysical Research Letters*, *24*(20), 2515–2518.

Sedwick, P. N., C. M. Marsay, B. M. Sohst, A. M. Aguilar-Islas, M. C. Lohan, M. C. Long, K. R. Arrigo, R. B. Dunbar, M. A. Saito, W. O. Smith, and G. R. DiTullio (2011), Early season depletion of dissolved iron in the Ross Sea polynya: Implications for iron dynamics on the Antarctic continental shelf, *Journal of Geophysical Research*, *116*(C12019), doi:10.1029/2010JC006553.

Segura, V., V. A. Lutz, A. Dogliotti, R. I. Silva, R. M. Negri, R. Akselman, and H. Benavides (2013), Phytoplankton types and primary production in the Argentine Sea, *Marine Ecology Progress Series*, *491*, 15–31.

Siedlecki, S. A., D. E. Archer, and A. Mahadevan (2011), Nutrient exchange and ventilation of benthic gases across the continental shelf break, *Journal of Geophysical Research*, *116*, C06023, doi:10.1029/2010JC006365.

Siedlecki, S. A., A. Mahadevan, and D. E. Archer (2012), Mechanism for export of sediment-derived iron in an upwelling regime, *Geophysical Research Letters*, *39*, L03601, doi:10.1029/2011GL050366.

Siegel, D. A. (2002), Global distribution and dynamics of colored dissolved and detrital organic materials, *Journal of Geophysical Research*, *107*(C12), 3228, doi:10.1029/2001JC000965.

Siegel, D. A., M. Behrenfeld, S. Maritorena, C. R. McClain, D. Antoine, S. W. Bailey, P. S. Bontempi, E. S. Boss, H. M. Dierssen, S. C. Doney, R. E. Eplee, Jr, R. H. Evans, G. C. Feldman, E. Fields, B. A. Franz, N. A. Kuring, C. Mengelt, N. B. Nelson, F. S. Patt, W. D. Robinson, J. L. Sarmiento, C. M. Swan, P. J. Werdell, T. K. Westberry, J. G. Wilding, and J. A. Yoder (2013), Remote Sensing of Environment, *Remote Sensing of Environment*, *135*(C), 77–91, doi:10.1016/j.rse.2013.03.025.

Signorini, S. R., V. M. T. Garcia, A. R. Piola, C. A. E. Garcia, M. M. Mata, and C. R. Mcclain (2006), Seasonal and interannual variability of calcite in the vicinity of the Patagonian shelf break (38 °S–52 °S), *Geophysical Research Letters*, *33*, L16610, doi:10.1029/2006GL026592.

Signorini, S. R., V. M. Garcia, A. R. Piola, H. Evangelista, C. R. Mcclain, C. A. Garcia, and M. M. Mata (2009), Further Studies on the Physical and Biogeochemical Causes for Large Interannual Changes in the Patagonian Shelf Spring-Summer Phytoplankton Bloom Biomass, *NASA Technical Memorandum*.

Simmonds, I., and K. Keay (2000), Mean Southern Hemisphere Extratropical Cyclone Behavior in the 40-Year NCEP-NCAR Reanalysis., *Journal of Climate*, *13*(5), 873–885.

Simmonds, I., K. Keay, and E.-P. Lim (2003), Synoptic Activity in the Seas around Antarctica, *Monthly Weather Review*, *131*, 272–.

Smith, J. (1998), Evolution of Langmuir circulation during a storm, *Journal of Geophysical Research*, *103*(C6), 12,649–12,668.

Sokolov, S., and S. R. Rintoul (2007), On the relationship between fronts of the Antarctic Circumpolar Current and surface chlorophyll concentrations in the Southern Ocean, *Journal of Geophysical Research*, *112*, C07030, doi:10.1029/2006JC004072.

Song, H., J. Marshall, M. J. Follows, S. Dutkiewicz, and G. Forget (2016), Source waters for the highly productive Patagonian shelf in the southwestern Atlantic, *Journal of Marine Systems*, *158*, 120–128, doi:10.1016/j.jmarsys.2016.02.009.

Stammer, D. (1998), On Eddy Characteristics, Eddy Transports, and Mean Flow Properties, *Journal of Physical Oceanography*, *28*(4), 727–739.

Stephenson, G. R., Jr., S. T. Gille, and J. Sprintall (2012), Seasonal variability of upper ocean heat content in Drake Passage, *Journal of Geophysical Research*, *117*, C04,019, doi:10.1029/2011JC007772.

Strass, V., A. Naveira Garabato, R. Pollard, H. Fischer, I. Hense, J. Allen, J. Read, H. Leach, and V. Smetacek (2002), Mesoscale frontal dynamics: shaping the environment of primary production in the Antarctic Circumpolar Current, *Deep Sea Research Part II*, *49*, 3735–3769.

Sunda, W., and S. Huntsman (1995), Iron uptake and growth limitation in oceanic and coastal phytoplankton, *Marine Chemistry*, *50*, 189–206.

Sverdrup, H. U. (1953), On conditions for the vernal blooming of phytoplankton, *JJournal du Conseil International pour l'Exploration de la Mer*, *18*, 287–295.

Swart, S., S. J. Thomalla, and P. M. S. Monteiro (2014), Journal of Marine Systems, *Journal of Marine Systems*, pp. 1–13.

Tagliabue, A., J.-B. Sallée, A. R. Bowie, M. Lévy, S. Swart, and P. W. Boyd (2014), Surface-water iron supplies in the Southern Ocean sustained by deep winter mixing, *Nature Geoscience*, *7*(4), 314–320.

Talley, L. D., G. L. Pickard, W. J. Emery, and J. H. Swift (2011), Chapter 4 - typical distributions of water characteristics, in *Descriptive Physical Oceanography (Sixth Edition)*, edited by L. D. Talley, G. L. Pickard, W. J. Emery, and J. H. Swift, sixth edition ed., pp. 67 – 110, Academic Press, Boston, doi:http://dx.doi.org/10.1016/B978-0-7506-4552-2.10004-6.

Taylor, A. G., R. Goericke, M. R. Landry, K. Selph, D. A. Wick, and M. J. Roadman (2012), Sharp gradients in phytoplankton community structure across a frontal zone in the California Current Ecosystem, *Journal of Plankton Research*, *34*(9), 778–789.

Taylor, J. R., and R. Ferrari (2011a), Shutdown of turbulent convection as a new criterion for the onset of spring phytoplankton blooms, *Limnology and Oceanography*, *56*, 2293–2307.

Taylor, J. R., and R. Ferrari (2011b), Ocean fronts trigger high latitude phytoplankton blooms, *Geophysical Research Letters*, *38*, L23601, doi:10.1029/2011GL049312.

Therriault, J.-C., D. A. Booth, L. Legendre, and S. Demers (1990), Phytoplankton photoadaptation to vertical excursion as estimated by an in vivo fluorescence ratio, *Marine Ecology Progress Series*, *60*, 97–111.

Thomalla, S. J., N. Fauchereau, S. Swart, and P. M. S. Monteiro (2011), Regional scale characteristics of the seasonal cycle of chlorophyll in the Southern Ocean, *Biogeosciences*, *8*, 2849–2866.

Thomas, L., and R. Ferrari (2008), Friction, Frontogenesis, and the Stratification of the Surface Mixed Layer, *Journal of Physical Oceanography*, *38*(11), 2501–2518.

Thomas, L. N., and C. M. Lee (2005), Intensification of ocean fronts by down-front winds, *Journal of Physical Oceanography*, *35*(6), 1086–1102.

Thompson, D. W. J., S. Solomon, P. J. Kushner, M. H. England, K. M. Grise, and D. J. Karoly (2011), Signatures of the Antarctic ozone hole in SouthernHemisphere surface climate change, *Nature Geoscience*, *4*, 741–749.

Thompson, L. (2000), Ekman layers and two-dimensional frontogenesis in the upper ocean, *Journal of Geophysical Research: Oceans*, *105*(C3), 6437–6451, doi:10.1029/1999JC900336.

Thomson, R. E., and I. V. Fine (2003), Estimating mixed layer depth from oceanic profile data, *Journal of Atmospheric and Oceanic Technology*, *20*(2), 319–329.

Thorpe, S. A. (1977), Turbulence and Mixing in a Scottish Loch, *Philosophical Transactions for the Royal Society of London. Series A*, *286*(1), 125–181.

Tréguer, and P. Pondaven (2001), Preface: climatic changes and the carbon cycles in the Southern Ocean: a step forward, *Deep Sea Research Part II*, *49*, 15971600.

Tzella, A., and P. H. Haynes (2007), Small-scale spatial structure in plankton distributions, *Biogeosciences*, *4*(2), 173–179.

Ulbrich, U., G. C. Leckebusch, and J. G. Pinto (2009), Extra-tropical cyclones in the present and future climate: a review, *Theoretical and Applied Climatology*, *96*(1-2), 117–131.

Valla, D., and A. R. Piola (2015), Evidence of upwelling events at the northern Patagonian shelf break, *Journal of Geophysical Research: Oceans*, *120*(11), 7635–7656.

Venables, H., and C. M. Moore (2010), Phytoplankton and light limitation in the Southern Ocean: Learning from high-nutrient, high-chlorophyll areas, *Journal of Geophysical Research*, *115*, C02015, doi:10.1029/2009JC005361.

Vera, C. (2003), Interannual and interdecadal variability of atmospheric synoptic-scale activity in the Southern Hemisphere, *Journal of Geophysical Research*, *108*(C4).

Verlinden, K. L., D. W. J. Thompson, and G. L. Stephens (2011), The Three-Dimensional Distribution of Clouds over the Southern Hemisphere High Latitudes, *Journal of Climate*, *24*, 5799–5811.

Vernet, M., D. Martinson, R. Iannuzzi, S. Stammerjohn, W. Kozlowski, K. Sines, R. Smith, and I. Garibotti (2008), Primary production within the sea-ice zone west of the Antarctic Peninsula: I–Sea ice, summer mixed layer, and irradiance, *Deep Sea Research Part II*, *55*, 2068–2085.

Vivier, F., and C. Provost (1999), Direct velocity measurements in the Malvinas Current, *Journal of Geophysical Research: Oceans*, *104*(C9), 21,083–21,103.

Vivier, F., C. Provost, and M. P. Meredith (2001), Remote and Local Forcing in the Brazil–Malvinas Region, *JPO*, pp. 1–22.

Wagener, T., C. Guieu, R. Losno, S. Bonnet, and N. Mahowald (2008), Revisiting atmospheric dust export to the Southern Hemisphere ocean: Biogeochemical implications, *Global Biogeochemical Cycles*, GB2006, doi:10.1029/2007GB002984.

Waite, A. M., S. Pesant, D. A. Griffin, P. A. Thompson, and C. M. Holl (2007), Oceanography, primary production and dissolved inorganic nitrogen uptake in two Leeuwin Current eddies, *Deep Sea Research Part II*, *54*, 981–1002.

Wallace, J. M., T. P. Mitchell, and C. Deser (1989), The Influence of Sea Surface Temperature variability on Surface Wind in the Eastern equatorial Pacific: Seasonal and Interannual Variability, *Journal of Climate*, *2*, 1492–1499.

Wang, X. L., Y. Feng, G. P. Compo, V. R. Swail, F. W. Zwiers, R. J. Allan, and P. D. Sardeshmukh (2012), Trends and low frequency variability of extra-tropical cyclone activity in the ensemble of twentieth century reanalysis, *Climate Dynamics*, *40*(11-12), 2775–2800.

Winn, C. D., L. Campbell, J. R. Christian, R. M. Letelier, D. V. Hebel, J. E. Dore, L. Fujieki, and D. M. Karl (1995), Seasonal variability in the phytoplankton community of the North Pacific Subtropical Gyre, *Global Biogeochemical Cycles*, *9*(4), 605–620.

Xie, S.-P. (2004), Satellite Observations of Cool Ocean–Atmosphere Interaction*, *Bulletin of the American Meteorological Society*, *85*, 195–208.

Xing, X., H. Claustre, S. Blain, F. D'ortenzio, D. Antoine, J. Ras, and C. Guinet (2012), Quenching correction for in vivo chlorophyll fluorescence acquired by autonomous platforms: A case study with instrumented elephant seals in the Kerguelen region (Southern Ocean), *Limnol. Oceanogr.: Methods*, *10*, 483–495, doi: 10.4319/lom.2012.10.483.

Xue, Y., B. Huang, Z.-Z. Hu, A. Kumar, C. Wen, D. Behringer, and S. Nadiga (2011), An assessment of oceanic variability in the NCEP climate forecast system reanalysis, *Climate Dynamics*, *37*, 2511–2539.

Yuan, X. (2004), High-wind-speed evaluation in the Southern Ocean, *Journal of Geophysical Research*, *109*, D13101, doi:10.1029/2003JD004179.

Zhang, W. G., D. J. McGillicuddy, Jr., and G. G. Gawarkiewicz (2013), Is biological productivity enhanced at the New England shelfbreak front?, *Journal of Geophysical Research: Oceans*, *118*(1), 517–535.